PLASMONIC NANOPARTICLES AS SENSORS:

A NOVEL APPROACH TO QUANTIFY ADSORPTION AND DIFFUSION KINETICS

Dissertation

zur Erlangung des akademischen Grades

Doktor der Naturwissenschaften

– Dr. rer. nat. –

am Fachbereich Chemie, Pharmazie und Geowissenschaften

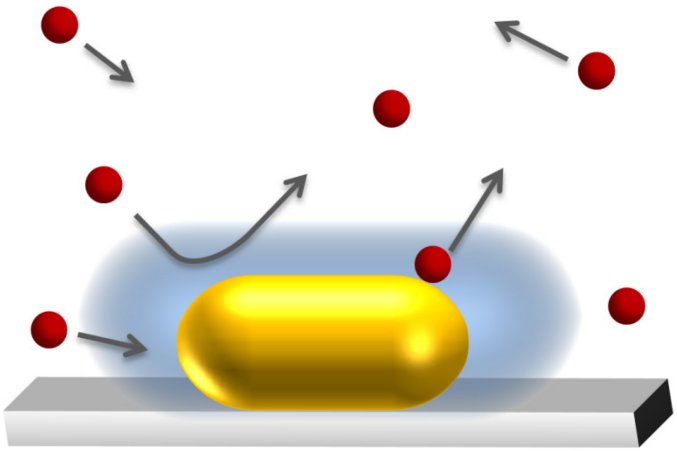

Verena Kleiner

geboren in Bamberg

Mainz 2014

Kennzeichen D77

Dekan:	[personal data removed]
Erster Gutachter:	[personal data removed]
Zweiter Gutachter:	[personal data removed]
Vorsitzender der Prüfungskommission:	[personal data removed]
Beisitzer der Prüfungskommission:	[personal data removed]

Tag der mündlichen Prüfung: 11. September 2014

No science has ever made more rapid progress in a shorter time than chemistry.

-- Martin Heinrich Klaproth, 1791

Diese Arbeit entstand im Zeitraum Juni 2011 bis Mai 2014 im Arbeitskreis am Institut für Physikalische Chemie, Johannes Gutenberg Universität Mainz.

I acknowledge the Carl Zeiss Foundation for providing me a PhD scholarship.

Carl Zeiss Stiftung

ABSTRACT

Biosensors find wide application in clinical diagnostics, bioprocess control and environmental monitoring. They should not only show high specificity and reproducibility but also a high sensitivity and stability of the signal. Therefore, I introduce a novel sensor technology based on plasmonic nanoparticles which overcomes both of these limitations. Plasmonic nanoparticles exhibit strong absorption and scattering in the visible and near-infrared spectral range. The plasmon resonance, the collective coherent oscillation mode of the conduction band electrons against the positively charged ionic lattice, is sensitive to the local environment of the particle. I monitor these changes in the resonance wavelength by a new dark-field spectroscopy technique. Due to a strong light source and a highly sensitive detector a temporal resolution in the microsecond regime is possible in combination with a high spectral stability. This opens a window to investigate dynamics on the molecular level and to gain knowledge about fundamental biological processes.

First, I investigate adsorption at the non-equilibrium as well as at the equilibrium state. I show the temporal evolution of single adsorption events of fibrinogen on the surface of the sensor on a millisecond timescale. Fibrinogen is a blood plasma protein with a unique shape that plays a central role in blood coagulation and is always involved in cell-biomaterial interactions. Further, I monitor equilibrium coverage fluctuations of sodium dodecyl sulfate and demonstrate a new approach to quantify the characteristic rate constants which is independent of mass transfer interference and long term drifts of the measured signal. This method has been investigated theoretically by Monte-Carlo simulations but so far there has been no sensor technology with a sufficient signal-to-noise ratio.

Second, I apply plasmonic nanoparticles as sensors for the determination of diffusion coefficients. Thereby, the sensing volume of a single, immobilized nanorod is used as detection volume. When a diffusing particle enters the detection volume a shift in the resonance wavelength is introduced. As no labeling of the diffusers is necessary the hydrodynamic radius and thus the diffusion properties are not altered and can be studied in their natural form. In comparison to the conventional Fluorescence Correlation Spectroscopy technique a volume reduction by a factor of 5000-10000 is reached.

CONTENTS

LIST OF ABBREVIATIONS

abs	**ABS**orption
AFM	**A**tomic **F**orce **M**icroscopy
AR	**A**spect **R**atio
ASF	**A**vailable **S**urface **F**unction
ATR-FTIR	**A**ttenuated **T**otal **R**eflectance **F**ourier **T**ransform **I**nfra**R**ed
CMC	**C**ritical **M**icelle **C**oncentration
CTAB	**C**etyl **T**rimethyl**A**mmonium **B**romide
DNA	**D**eoxyribo**N**ucleic **A**cid
ELL	**ELL**ipsometry
EMCCD	**E**lectron **M**ultiplying **C**harge **C**oupled **D**evice
FCS	**F**luorescence **C**orrelation **S**pectroscopy
FFT	**F**ast **F**ourier **T**ransform
FWHM	**F**ull **W**idth **A**t **H**alf **M**aximum
MWCO	**M**olecular **W**eight **C**ut-**O**ff
NP	**N**ano**P**article
NR	**N**eutron **R**eflection
PBS	**P**hosphate **B**uffered **S**aline
PEG	**P**oly**E**thylene **G**lycol
PSD	**P**ower **S**pectral **D**ensity
QCM	**Q**uartz **C**rystal **M**icrobalance
QSA	**Q**uasi-**S**tatic **A**pproximation
rpm	**R**adiation **P**er **M**inute
SAM	**S**elf-**A**ssembled **M**onolayer
sca	**SCA**ttering
SDS	**S**odium **D**odecyl **S**ulfate
SEM	**S**canning **E**lectron **M**icroscopy
SN	**S**ignal-to-**N**oise ratio
SPR	**S**urface **P**lasmon **R**esonance
TIR	**T**otal **I**nternal **R**eflection
UV/Vis	**U**ltra**V**iolet/**VIS**ible

LIST OF FIGURES

The schematic representation of a gold nanoparticle immobilized on a glass surface as presented on the cover and within a few other figures originates from literature [1] and was applied with slight modifications.

LIST OF TABLES

Chapter 1

Almost all the chemical processes which occur in nature, whether in animal or vegetable organisms, or in the non-living surface of the earth – take place between substances in solution.

-- Wilhelm Ostwald

1 Introduction

In clinical diagnostics[2, 3] as well as in bioprocess control[4, 5] and environmental monitoring[6, 7] there is a strong need for biosensors. A powerful biosensor is characterized by its high specificity,[8] sensitivity,[9] stability[10] and reproducibility[11] of the signal so that a target can be easily and reliably identified and quantified even at low concentrations. The design of a whole biosensor system (see *Figure 1*) is quite complex and requires interdisciplinary knowledge. In principle, there are three different components. First, the biological recognition occurs where the target attaches to a receptor. Second, the attachment is converted into a signal that can be measured and quantified. Third, an electronic device displays the measured value.[12]

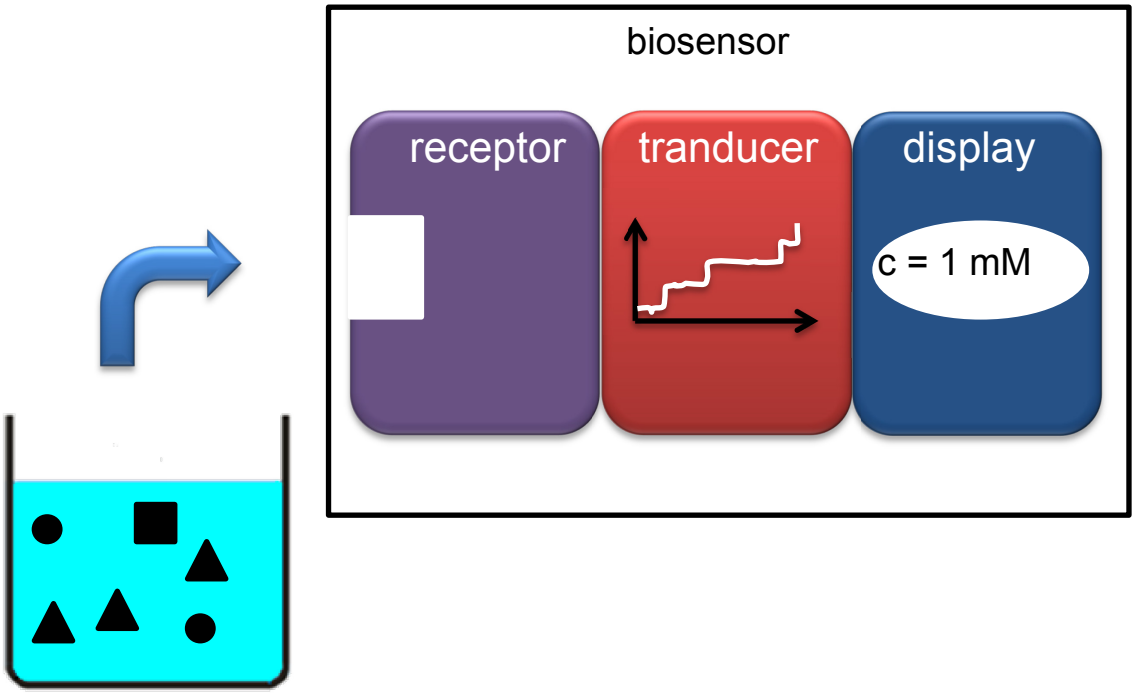

Figure 1. Schematic representation of a biosensor. A receptor is necessary for biological recognition. This is then converted into a measured signal which is displayed by an electronic device. This figure was prepared in dependence on literature [13].

Many physical parameters can be utilized for transduction. Just to name some examples: With a Quartz Crystal Microbalance (QCM) the mass per unit area is quantified by measuring changes in the resonance frequency of a piezoelectric crystal.[14] Electrochemical biosensors have recently been established where nanomaterials such as carbon nanotubes or graphene are applied for electrochemical communication between an electrode and redox proteins.[15] Another wide field is the usage of optical biosensors. Optical biosensors show the advantages that they are not affected by electromagnetic interference and can offer multiplexed detection within a single apparatus.[16] Surface Plasmon Resonance (SPR) is quite sensitive to changes in the refractive index due to material attachment on the surface of the sensor.[17, 18] SPR belongs to the class of optical biosensors where no labeling of the analyte (e.g. with fluorescent dyes) is necessary. Consequently, the targets can be investigated in their natural forms and their functions are not affected.[16] However, this technique does not reach the detection limit of a single molecule. The reason for this lies in the large surface area of the sensor. Thus, many molecules can adsorb at the same time and single

adsorption events are not detectable as fluctuations cancel each other out. Therefore, the sensor surface should be dramatically reduced to ideally the size of the target. Then, only few molecules can adsorb and fluctuations in signal are measurable (see *Figure 2*).

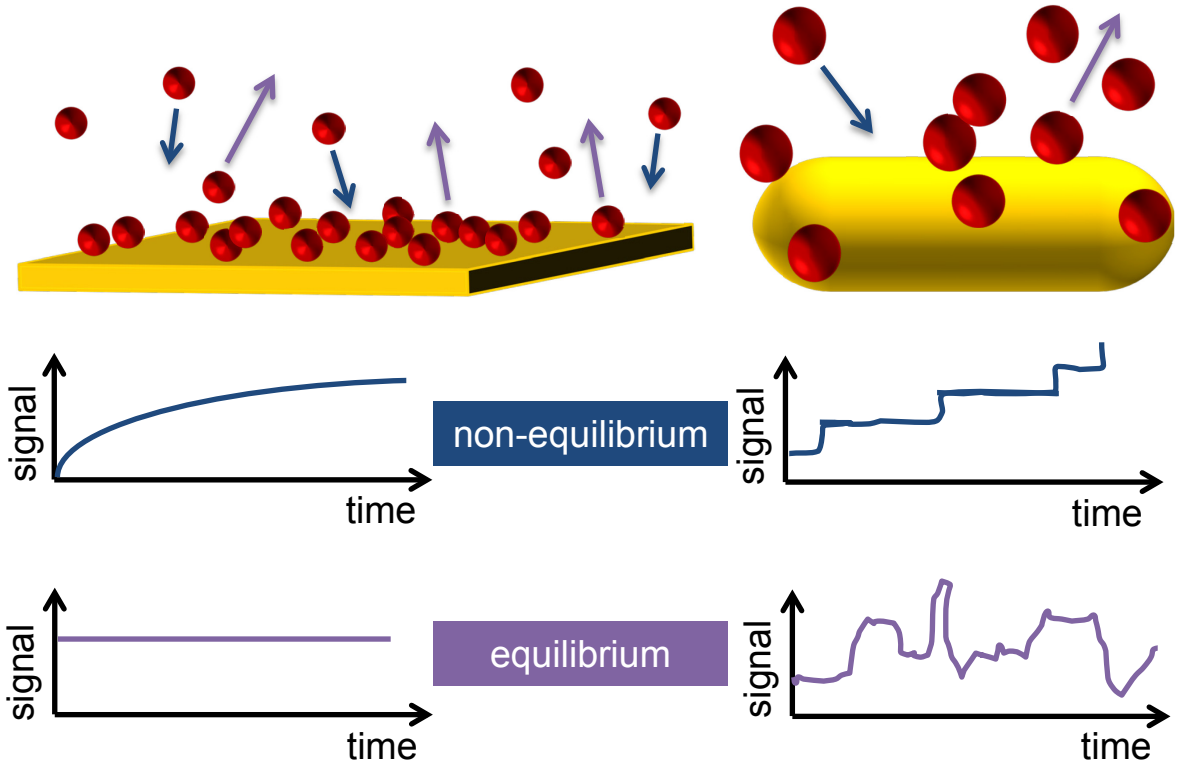

Figure 2. Comparison of a big sensor with a small sensor. An example for a big sensor is a gold chip in an SPR experiment (left). A gold nanorod can be applied as small sensor (right). On a big sensor many molecules can adsorb, single adsorption events are not detectable and fluctuations cancel each other out whereas single molecule attachment is measureable with smaller sensors. This counts for processes in equilibrium as well as at the non-equilibrium state. The figure originates from literature [19] with slight variations.

Hence, the consequence is to go to particles in the nanometer regime. Plasmonic nanoparticles exhibit strong absorption and scattering in the visible and near-infrared spectral range. The plasmon resonance of single nanoparticles, the collective coherent oscillation mode of the conduction band electrons against the positively charged ionic lattice, can be monitored by dark-field spectroscopy.[20] So far, this technique is quite established to measure the coverage of the entire sensor.[21] But recently, a novel setup was developed which overcomes the limitations of a low time resolution and a little spectral sensitivity. Thereby, a strong white light laser is coupled onto the sample via total internal reflection. Consequently, only light scattered by plasmonic particles is collected by

the objective of the microscope while the rest of the sample appears as dark background. The spectra are acquired by a sensitive detector which enables a temporal resolution in the microsecond regime.[22] This opens a window to investigate phenomena on the single molecule level and to gain knowledge about fundamental biological processes such as adsorption, diffusion and conformational changes.

Within this thesis I first give an introduction to plasmon theory. Plasmonic sensors are not only sensitive to changes in the refractive index but also to plasmon coupling and charging. These properties have also been applied within the presented projects and are consequently explained in *Chapter* 2 as well. *Chapter* 3 reveals technical and performance details about the Plasmon Fluctuation Setup. The setup was applied to observe single adsorption events of the blood plasma protein fibrinogen (see *Chapter* 4). Further, I monitored equilibrium coverage fluctuations of sodium dodecyl sulfate (SDS) and demonstrate a new approach to quantify the characteristic rate constants (see *Chapter* 5). Last but not least, I reveal a new method to quantify diffusion constants of particles (see *Chapter* 6).

Chapter 2

Erwin (Schrödinger) with his Psi can do calculations quite a few. But one thing has not been seen just what does Psi really mean.

-- Walter Hückel

2 Plasmonic Nanoparticles as Sensors

2.1 Plasmon Spectra

Noble metal nanoparticles exhibit strong absorption and scattering in the visible and near-infrared spectral range. In order to get a quantitative access to this phenomenon the well-known Drude-Sommerfeld model[23] can be taken into account. In this model electrons are described as free electron gas where the electrons do not interact with each other. When an external force like an electromagnetic oscillating wave is introduced to the system a collective coherent oscillation of the conduction band electrons against the positively charged ionic lattice occurs. This leads to the following dielectric function:

$$\epsilon(\omega) = 1 - \frac{\omega_p^2}{\omega(\omega + i\gamma_0)} \tag{2.1}$$

with the plasma frequency ω_p: $\omega_p = \sqrt{\frac{ne^2}{\epsilon_0 m^*}}$ (2.2)

Thereby n and m^* represent the density and the effective mass of the electrons.

Johnson and Christy[24] extended this model for real metals as the s-electrons have an influence on the plasma frequency, too. Through measurements of the dielectric functions of various metals *formula 2.1* can be extended to:

$$\epsilon(\omega) = \epsilon_{\infty} - \frac{\omega_p^2}{(\omega^2 + i\gamma\omega)} \tag{2.3}$$

with $1 \leq \epsilon_{\infty} \leq 10$.

To enlarge this model to noble metal nanoparticles the assumption that the diameter of the particle is to a great extent smaller than the wavelength of electromagnetic field has to be considered (see *Figure 3*).

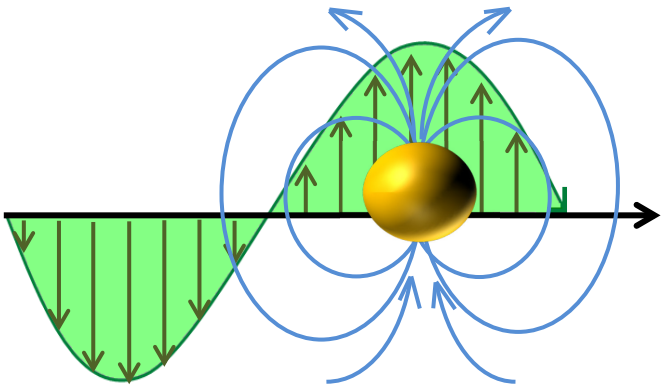

Figure 3. Particle Plasmons**.** An electromagnetic field leads to collective oscillations of the conduction electrons of a nanoparticle.

As a consequence, at each point of the nanoparticle the phase of the light can be regarded as the same. Now, only the time dependency of the field has to be taken into account and a so called Quasi-Static Approximation (QSA) can be conducted. The scattering (sca) and absorption (abs) cross sections can be described through:[25]

$$C_{sca} = \frac{k^4}{6\pi}|\alpha|^2 \tag{2.4}$$

$$C_{abs} = k \cdot Im(\alpha) \tag{2.5}$$

with the wave vector k: $k = 2\pi\frac{\sqrt{\varepsilon_m}}{\lambda}$ (2.6)

The extinction cross-section is the sum of the absorption and scattering cross sections.[26] Thereby, α is the polarizability of the particle with the volume V and λ the wavelength of the electromagnetic field. α can be expressed through the Clausius Mossotti relation:

$$\alpha = 3V\frac{\varepsilon_{NP} - \varepsilon_m}{\varepsilon_{NP} + 2\varepsilon_m} \tag{2.7}$$

with ε_{NP} as dielectric function of the nanoparticle and ε_m as dielectric constant of the medium. The intensity of the light after interaction with the particles is decreased:

$$I_{abs/sca} = \frac{I_0(\omega)}{A}C_{abs/sca}(\omega) \tag{2.8}$$

Within the projects in the framework of this thesis gold nanorods where applied as sensors.[27] For particles with ellipsoidal shape, the polarizability has to be modified to:[28]

$$\alpha_i = 4\pi abc\frac{\varepsilon_{NP} - \varepsilon_m}{3\varepsilon_m + 3L_i(\varepsilon_{NP} - \varepsilon_m)} \tag{2.9}$$

with the axes a,b,c ($a \geq b = c$) and the geometry factors L_i:

$$L_a = \frac{1-e^2}{e^2}\left(-1 + \frac{1}{2e}\ln\left(\frac{1+e}{1-e}\right)\right) \tag{2.10}$$

and

$$L_{b,c} = \frac{1-L_a}{2} \tag{2.11}$$

with the eccentricity $e^2 = 1 - (\frac{b}{a})^2$ (2.12)

In order to get a more precise description of the scattering spectra, also end-shape geometries and surface properties have to be considered.[29, 30] In many applications, it is necessary

to regard the nanoparticle as an inner core surrounded by an outer shell with a different refractive index, i.e. when the nanoparticle is functionalized with a layer consisting of another metal[31] or coated with a membrane.[21] The polarizability is then modified to:[32]

$$\alpha_i = V_{total} \frac{\{(\epsilon_s - \epsilon_m)[\varepsilon_s + (\varepsilon_{NP} - \varepsilon_s)(L_i^{(NP)} - fL_i^{(s)})] + f\varepsilon_s(\varepsilon_{NP} - \varepsilon_s\}}{[\varepsilon_s + (\varepsilon_{NP} - \varepsilon_s)(L_i^{(NP)} - fL_i^{(s)})][\varepsilon_m + (\varepsilon_s - \varepsilon_m)L_i^{(s)}] + fL_i^{(s)}\varepsilon_s(\varepsilon_{NP} - \varepsilon_s)} \tag{2.13}$$

with the dielectric constant of the shell medium ε_s, the total volume of the coated nanoparticle V_{total}, the geometrical factors $L_i^{(NP)}$ and $L_i^{(s)}$ as well as the fraction f:

$$f = \frac{a_{NP}b_{NP}c_{NP}}{a_s b_s c_s} \tag{2.14}$$

Particle plasmons can be studied in particle suspensions as well as on the single particle level. The transmitted light through a particle suspension can simply be analyzed by an UV/Vis-spectrometer (ensemble spectrum). The resulting spectrum (see *Figure 4*) provides a lot of information about the particles.

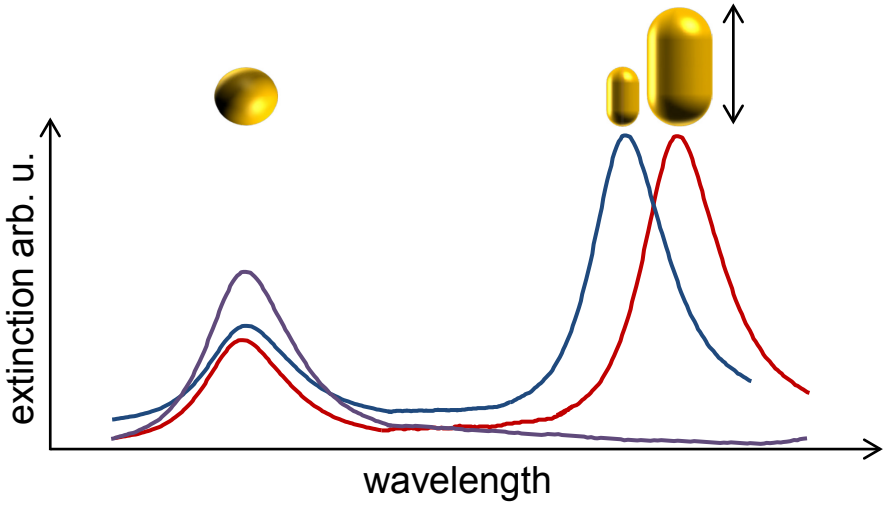

Figure 4. Schematic representation of extinction spectra of nanoparticles. Spectra of nanospheres (purple) and nanorods with two different aspect ratios (red and blue) are shown. Nanospheres only show one resonance peak. Rods show two resonance peaks corresponding to the short and the long axis of the rod. The position of the second peak is dependent on the mean aspect ratio of the rods in solution.

Due to its anisotropic shape nanorods show not only one but two maxima (transversal resonance of short axis at around 520 nm and longitudinal resonance along long axis typically around 600-700 nm). Thus, these values contain information about the dimensions of the particles. The full width at half maximum (FWHM) provides information about the polydispersity of the sample. The sharper the spectra the more homogenous are the particles. Applying Lambert-Beer's law

$$E = \varepsilon \cdot c \cdot d \tag{2.15}$$

the measured extinction E can be used to calculate the concentration c of nanoparticles in suspension knowing the extinction coefficient ε and the thickness of the cuvette d. The scattering spectrum of a single particle can be acquired via dark-field microscopy.[20] Therefore, nanoparticles fixed onto a glass surface are illuminated via a dark-field condenser. Thus, only light scattered by the particles is collected by the objective of the microscope and the rest of the sample appears as black background. More detailed information on the setup used for the here presented projects can be found in *Chapter* 3.

2.2 Plasmonic Sensors

In the following I will present the principles due to which physical effects plasmonic nanoparticles can be applied as sensors: they are sensitive to changes in the refractive index, the plasmon resonance shifts through interaction with other plasmonic particles (plasmon coupling) and third, the resonance position shifts if charge is introduced (see *Figure 5*). For sensing applications some general things have to be considered including the choice of the right material as well as the optimal shape and size of the sensor. Silver particles for example show higher sensitivities than gold particles. However, even in aqueous medium they are less inert.[33] The sensitivity can also be improved by special shapes of the sensors.[34, 35] Within this thesis only gold nanorods were established which show in comparison to nanospheres higher sensitivities and the aspect ratios where optimized in dependence of the analyte.[36] Further, for biological applications the toxicity of the nanoparticles has generally to be considered.[37]

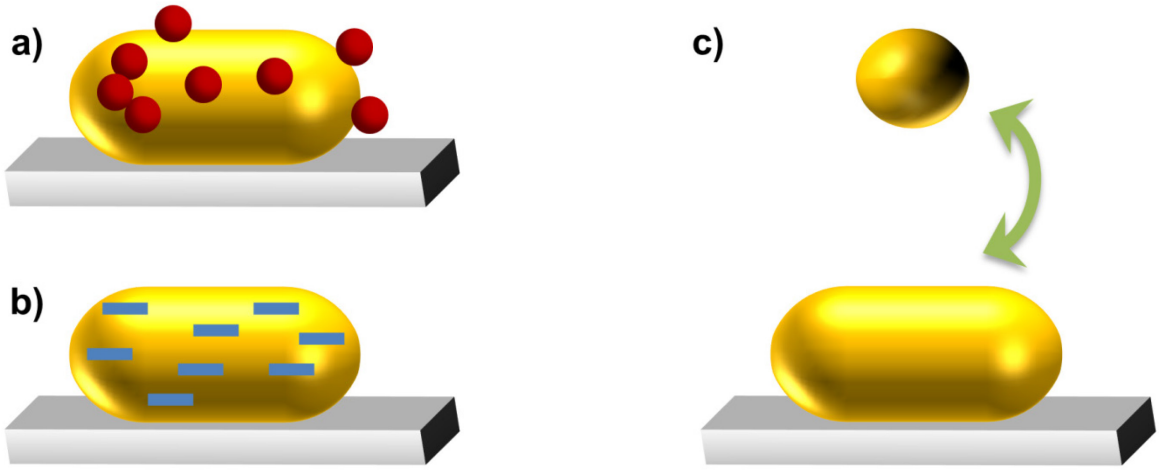

Figure 5. The resonance wavelength of a gold nanoparticle can be shifted by 3 different effects. **a)** changes in the refractive index, **b)** charging and **c)** and plasmon coupling.

2.2.1 Sensing due to Changes in the Refractive Index

The resonance wavelength of a plasmonic nanoparticle is dependent of the dielectric constant of the surrounding medium, ε_m, or in other words of the refractive index, n, of the local environment:[38]

$$\Delta\lambda_{res} = S_\lambda \Delta n (1 - \exp\left(-\frac{2d}{I_d}\right)) \tag{2.16}$$

with the sensitivity S_λ: $S_\lambda = \frac{\Delta\lambda}{\Delta n}$ (2.17)

Thereby, Δn is defined as change in the refractive index, d represents the thickness of the adsorbed layer and I_d the sensing distance of the sensor. This results from the fact that the electromagnetic field lines also enter the surrounding medium. Because of their small size plasmonic nanoparticles can not only be applied as sensors when the whole surrounding medium is exchanged (i.e. change from water to glycerin) but also when small particles attach to the surface of the sensor (see *Figure 6*). Consequently, they are widely applied as sensors or markers in biological systems.[39] In the workgroup of this principle has already been applied to develop a sensor for the specific recognition of proteins[40] as well as for the detection of single binding events.[22]

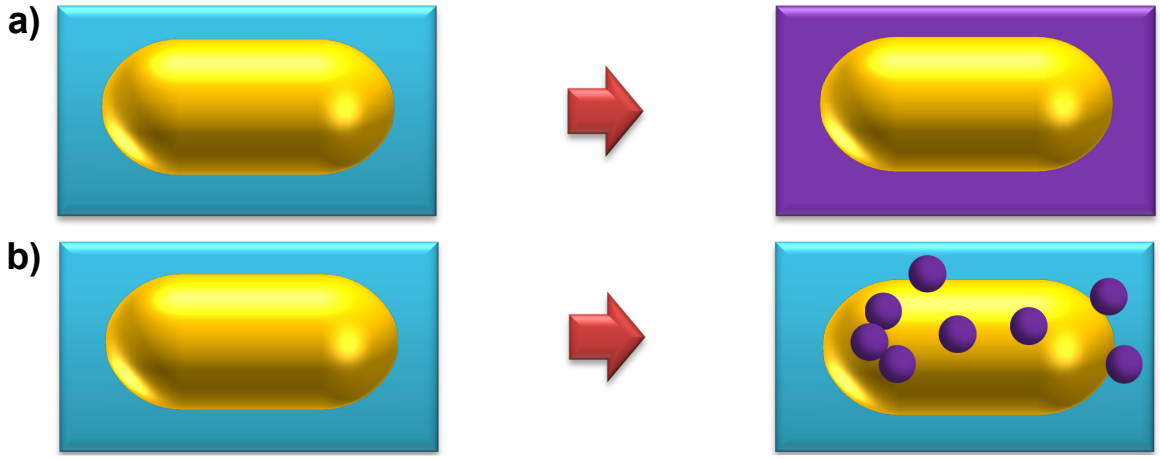

Figure 6. Sensing due to refractive index changes. Refractive index changes can be caused by altering the refractive index of the whole surrounding medium (**a**) or by attachment of small particles with another refractive index (**b**).

2.2.2 Sensing due to Plasmon Coupling

When two or more plasmonic nanoparticles are arranged closely to each other their electromagnetic field lines overlap which results in a change of the resonance positions. This effect is called plasmon coupling.[41] Up to now a lot of effort has been done to gain knowledge about this phenomenon itself[42] because of many interesting effects like the appearance of novel plasmonic modes[43] or hot spots.[44] However, there is also a great potential for various applications. One famous application is the concept of the plasmon ruler, where two particles are bound to each other through a spacer and it is taken use of the fact that the resonance wavelength is distance dependent of the two particles.[45-47]

The simplest case to study plasmon coupling is the so called homodimer where the interactions of identical particles, i.e. spheres of the same size and material are studied. There are already some publications which also have studied heterodimers.[48-50] In this thesis, the plasmon coupling of gold nanospheres with a gold nanorod is applied (see *Chapter* 6). As these interactions have already been studied and published by Shao *et al.*[51] a brief overview is in the following given on their results.

Shao *et al.*[51] investigated the plasmon coupling between a gold nanorod (average aspect ratio of around 2.2 with an average length of 85 nm) and a gold nanosphere (average

diameter: 24 nm). Therefore, they built heterodimers with a distance of 1 nm between the monomers and characterized them via Scanning Electron Microscopy (SEM), dark-field microscopy and simulations. The spectra changed systematically with the position of the sphere relative to the rod. While the scattering spectrum of a nanorod only shows one scattering peak the heterodimer shows two peaks whereas the one which is located more to the red scatters stronger. When the nanosphere "moves" from the end to the side of the nanorod the higher-energy peak gets stronger and red-shifts whereas the lower-energy peak blue-shifts so that the two peaks approach each other. When the nanosphere is situated exactly at the side of the rod, only one peak is visible. Further, the lower-energy peak is enhanced by the gap area between the two particles in comparison to the spectrum of only a single nanorod which indicates the presence of a hot spot. Finite-difference time-domain calculations show that mainly the scattering for the excitation polarized parallel to the substrate along the length axis of the nanorod (longitudinal polarization) causes the two scattering peaks. *Figure 7a* shows the plasmon hybridization diagram of a nanorod-nanosphere heterodimer. At the lower-energy peak the bounding dipole-dipole hybridized mode dominates. At the dip in between the two particles the dipole-quadruple mode prevails while at the higher-energy peak a mixture of the two of them is existent.

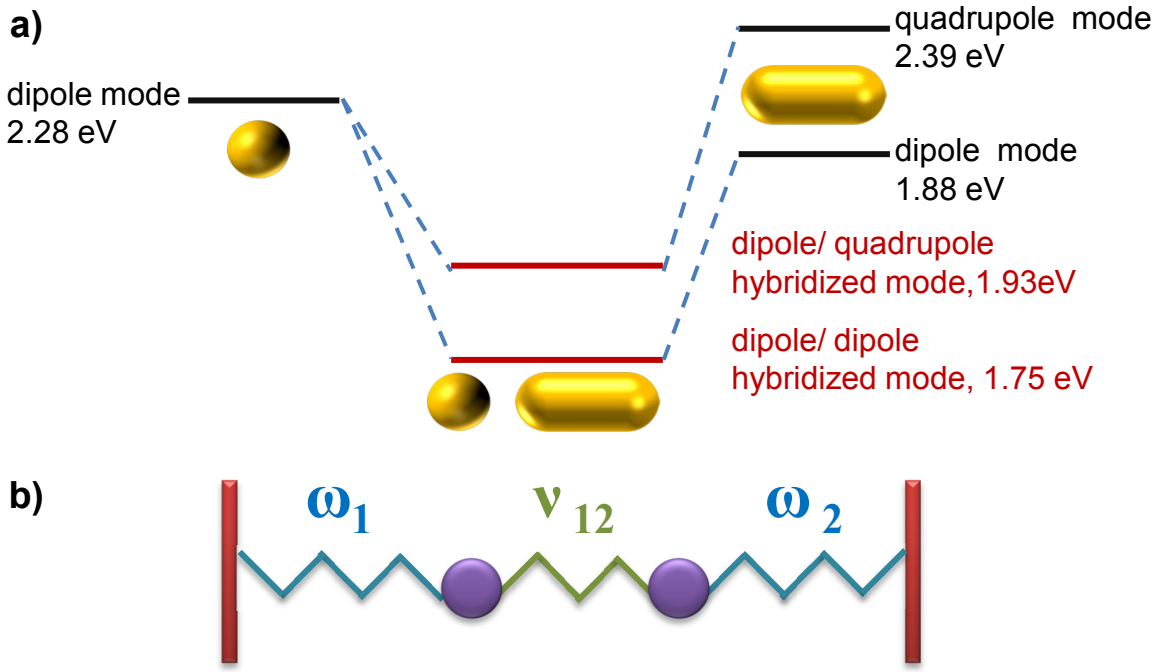

Figure 7. Plasmon coupling of the system "nanorod-nanosphere". **a)** Plasmon hybridization diagram and **b)** classical two-oscillator model. The figure was prepared in dependence on Shao *et al.*.[51]

A classical two-oscillator model can be used to describe the plasmon modes (see *Figure 7b*). The dipole-dipole and the dipole-quadrupole hybridized modes can be regarded as two mechanical oscillators with the energies ω_1 and ω_2 and the interacting strength v_{12}:

$$\ddot{x}_1 + \gamma_1\dot{x}_1 + \omega_1^2 x_1 - v_{12}x_2 = F_0\exp(-i\omega_{1/2}t) \tag{2.18}$$

$$\ddot{x}_2 + \gamma_2\dot{x}_2 + \omega_2^2 x_2 - v_{12}x_2 = 0 \tag{2.19}$$

with the friction coefficients γ_i and the displacement from the equilibrium position

$$x_i = c_i\exp(-i\omega t) \tag{2.20}$$

and the scattering power

$$P(\omega) = \left|\ddot{x}_1 + \ddot{x}_2\right|^2 \tag{2.21}$$

The further the nanosphere is away from the end of the rod ω_1 increases whereas ω_2 and v_{12} decrease. Further, the distance of the gap as well as the variation of the nanocrystals'

dimensions have been investigated within this publication. In summary, due to plasmon coupling larger shifts can be expected when a gold nanosphere enters the sensing volume of a nanorod in comparison an analyte of the same shape and size but of a dielectric material.

2.2.3 Sensing due to Charging

The resonance wavelength cannot only be shifted by changes in the refractive index or by plasmon coupling as described above but also by electron injection.[52] There are several ways to inject electrons which have been reported in literature like the utilization of electrodes[53] or the usage of conducting surfaces.[54] Mulvaney *et al.*[55] showed impressively that electron charging effects can simply be studied by electron loading. In the following I will briefly introduce their results.

Mulvaney *et al.*[55] studied shifts in the resonance position of gold nanorod suspensions by introducing $NaBH_4$. They determined severe shifts to the blue due to an increase in the electron density of the rods up to 50 nm depending on the dimensions of the rods. The shifts occurred after a few seconds, stayed stable for several hours and then red-shifted back in some cases although no full recovery of the resonance position was observed. The red shift is explained by the assumption that the electrons are transferred to water or to oxygen. Applying *formula (2.3)* and *formula (2.2)* to the following term which his valid for the description of absorption modes of plasmonic nanorods (L stands for the depolarization factor)

$$(1-L)\varepsilon_m + L\varepsilon'(\omega) = 0 \tag{2.22}$$

the shift in the absorbance spectra, $\Delta\lambda$, can be quantified to:

$$\Delta\lambda = -\frac{\Delta N}{2N}\lambda_p\sqrt{\varepsilon_\infty + (\frac{1}{L}-1)\varepsilon_m} \tag{2.23}$$

with the bulk gold plasma wavelength λ_p = 130 nm.

There is a simple relationship between $\Delta\lambda$, the resonance position λ_0 and the conduction electron concentration N:

$$\frac{\Delta N}{2N} = -\frac{\Delta\lambda}{\lambda_0} \tag{2.24}$$

This formula gives quick information about the amount of charge transfer just by determining the shift of an absorbance spectrum. These equations are only valid when particles are located in a medium with a high dielectric constant where high electron densities are present. This information provides a useful tool to estimate charge transfer and can help to trigger plasmon energies.

Chapter 3

Everything in the future is a wave, everything in the past is a particle.

-- Lawrence Bragg

3 The Plasmon Fluctuation Setup

In general, sensor miniaturization is also related with a poor detection limit. It has to be differentiated between short-term noise in timescales up to 1 s and long term instabilities.[56] In principle, all optical sensor devices operate by monitoring intensity values by a photodetector array. As the photon flux is usually converted into a current, the signal-to noise ratio can generally be expressed by

$$\frac{signal}{noise} = \frac{I(\alpha - 1)}{\sqrt{I + var(I_{noise})}} \tag{3.1}$$

Thereby, I is the current related to the measuring signal, I_{noise} represents the intrinsic noise of the setup and α is associated with a change in the value of I. As I is the only parameter which is dependent of the sensor size the impact of this parameter becomes clear.[56] In the following I will present the Plasmon Fluctuation Setup with overcomes the limitations through a low spectral stability.

The setup was developed by

. Consequently, at this point only information relevant to the following projects is presented. More details can be found in her thesis[57] and publication.[22]

3.1 Experimental Setup

Within the scope of this PhD thesis a sensor technology to quantify kinetic processes on the molecular scale was needed. Therefore, in comparison to conventional dark-field microscopes the Plasmon Fluctuation Setup shows significant improvements in terms of temporal resolution as well as signal-to-noise ratio (SN). This can be achieved by the construction presented in *Figure 8*.

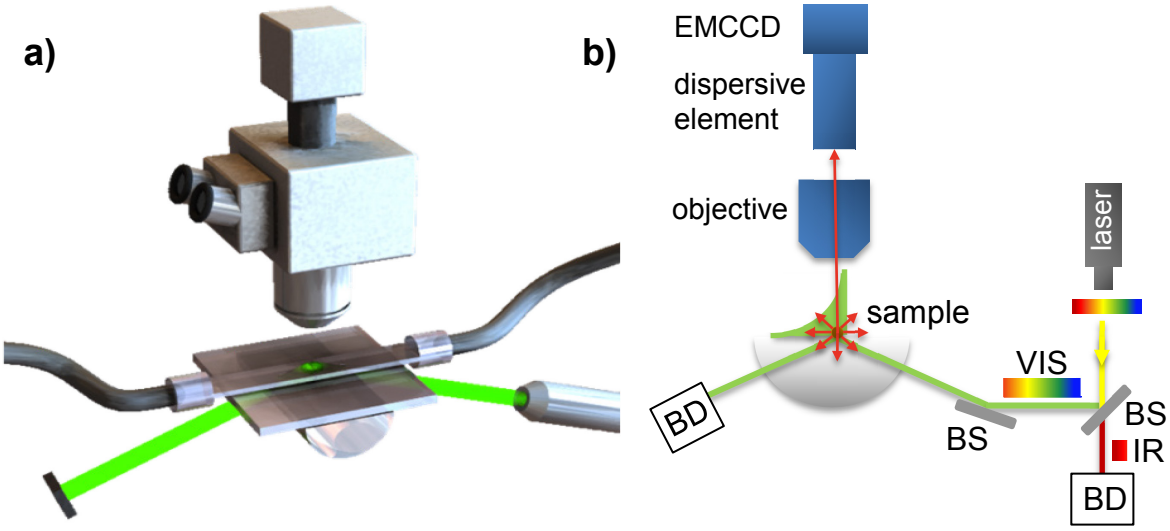

Figure 8. The Plasmon Fluctuation Setup. **a**) A 3D visualization is shown. The figure was kindly provided by S. Hein, University of Stuttgart and originates from Ament *et al.*.[22] **b)** Schematic representation with focus on the beam path. Before the laser beam is coupled onto the sample, a beam splitter (BS) only couples out the visible spectral region (VIS) up to 750 nm while the infrared region (IR) is collected by a beam dump. The figure originates from literature [1] with slight variations.

An upright transmission microscope (*Zeiss Axioskop*) is equipped with a total internal reflection (TIR) device for illumination. Therefore, a supercontiuum white light source (*Koheras SuperK-Power*) is injected via a glass half cylinder. The white light laser shows a wavelength range from 460 nm to 2400 nm. However, to avoid instability of the signal due to heating effects two optical filters were integrated into the beam bath so that the wavelength range is cut at 750 nm. This leads to a total output power of approximately 80 µW/mm²·nm. Gold nanoparticles which act as sensors are introduced into a 'home-built' flow cell and are electrostatically bound onto the glass surface by flushing with a 1 M solution of sodium chloride. The evanescent field illuminates the particles and their scattered light is collected by a 40x air objective (*Zeiss CP-Achromat, NA 0.65*). After

passing a dispersive element (*Spectim ImSpector V8*) the light is detected by an EMCCD camera (*Andor iXon DV885*). Additionally, a second slit which is situated at a 90 degree angle to the entrance slit of the dispersive element effectively shields light from areas of the chip which are not needed for data acquisition. The calibration of the pixel-to-wavelength relation of the camera was conducted through two different lasers (532 nm, 655 nm). For determination of the corresponding pixels the maxima were approximated with a Gaussian fit respectively. As a result, due to the stronger illumination source more photons reach the sample and are in turn scattered by the gold nanoparticles. The spectra are analyzed by a 'home-built' software called *Nanocenter* based on *MATLAB*. The resonance wavelength is calculated through fitting with a Lorentz function and its changes over time (timetrace) are investigated (see *Figure 9a*).

3.2 Setup Performance

The applied EMCCD camera is equipped with a so called *crop mode* which allows a minimal exposure time of 30 µs. Without this special mode, spectra can be acquired with a maximal time resolution of 2.45 ms. In comparison to common dark-field microscopes equipped with a halogen lamp and a dark-field condenser, the temporal resolution is improved by 4-6 orders of magnitude.[57]

The spectral stability is dependent of the dimensions of the sensor as well as of the chosen time resolution (see *Figure 9b*). In general, bigger rods show a more stable signal. Furthermore, the fluctuation amplitude increases with increasing time resolution. For measurements in the *standard mode*, which includes a time resolution of 5-10 ms and medium rods, a signal with a standard deviation of up to 0.02 nm can be obtained over several minutes.

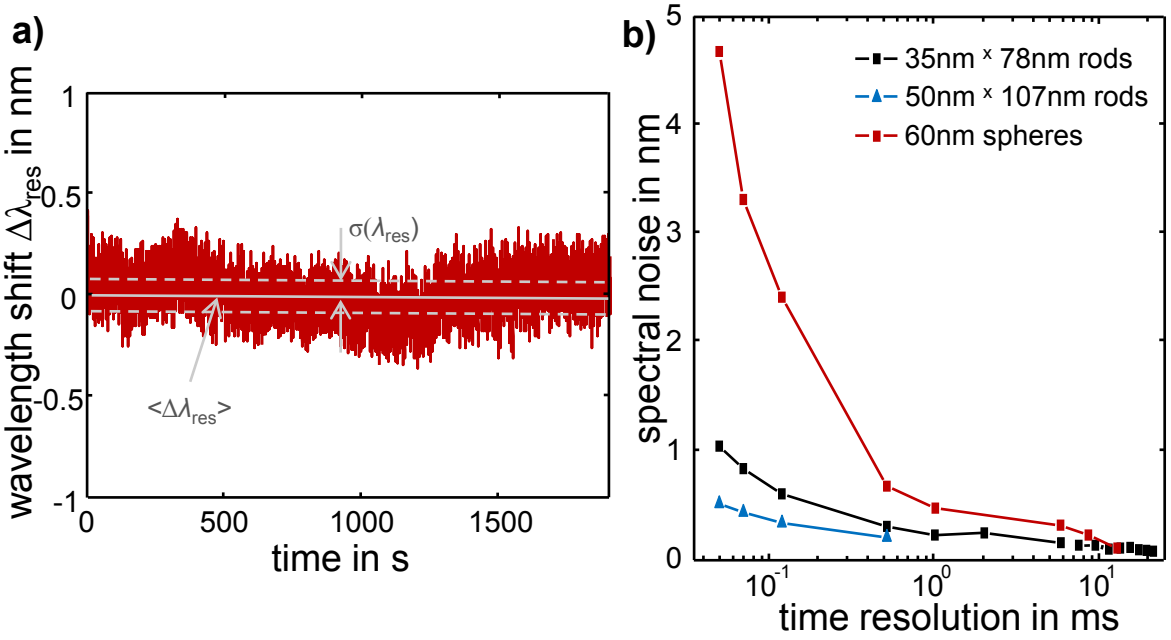

Figure 9. Data acquisition with the Plasmon Fluctuation Setup. **a)** Shift in the resonance wavelength over time (timetrace) of a single gold nanorod in aqueous medium. $\langle \Delta\lambda_{res} \rangle$ describes the mean value of the wavelength shift, $\sigma(\lambda_{res})$ corresponds to the spectral noise. **b)** The spectral noise is dependent on the dimensions of the particles and decreases with exposure time. This figure originates from literature [57].

For the following scientific projects it was of prior importance to improve the signal-to-noise ratio and consequently to obtain knowledge about the different noise sources and how they influence the signal under investigation. One major noise source is of course the white light laser. estimated a noise level of 1.5% for the millisecond regime and of around 3% for the microsecond regime.[57] Another noise source is the camera where three different kinds of noise can be classified. There is the shot noise which is dependent on the photon flux whereas the read noise is dependent on the gain. The third kind of noise, the dark noise, can be neglected for cooled EMCCD cameras.[58]

In general, a measured signal S_{meas} consists of two kinds of signal: signal S and noise N. They can be considered as superposition where N should be independent from S:

$$S_{meas} = S + N \tag{3.2}$$

The challenge within the following described research projects lay in a reliable separation of the measured signal into *S* and *N*. Different kinds of noise show different behavior in the frequency domain. White noise usually arises from extremely fast thermal fluctuations of elementary particles. Consequently, as the measurement time is always slower than the fluctuation time white noise can be regarded as independent of the frequency regime and thus appears as a horizontal line in the power spectrum.[59] Another kind of noise is the so called pink noise which shows a $1/\nu$ behavior for low frequencies. The origin often lies in correlated movements of charge carriers in electronic devices.[60] This is also the reason why data acquisition at higher frequencies is preferred. Noise with a $1/\nu^2$ behavior is called Brownian noise or red noise which originates -as the name implies- from Brownian motion. There are also a lot of other noise sources. If the signal in the timetrace contains any periodicity, the power spectrum shows the characteristic frequency by a sharp peak.[61] Other causes like temperature, air pressure or the presence of electromagnetic fields can also contribute to instrumental noise.

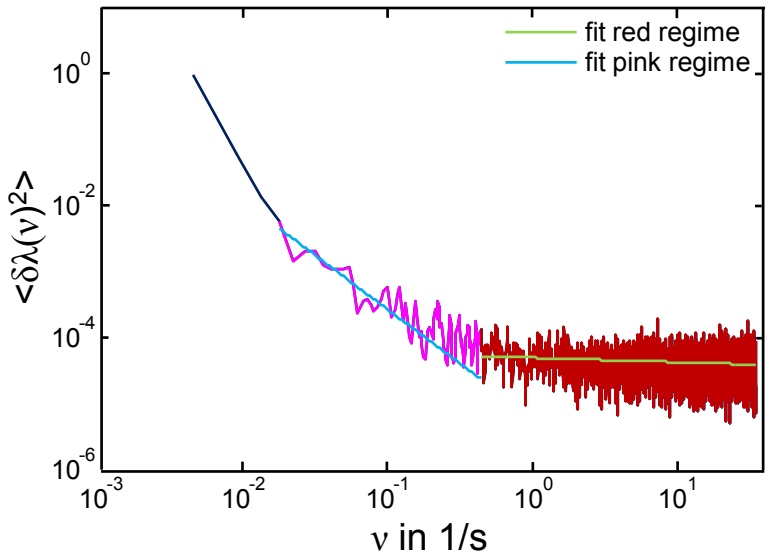

Figure 10. Power spectrum of a measured timetrace. The resonance spectra of one single gold nanoparticle in an aqueous medium were acquired for 10 min with an exposure time of 10 ms. The spectrum was calculated applying the Welch algorithm (further details see *Chapter 5.3*, section *Data Evaluation*). The pink regime and the red regime are approximated according to *formula 3.3* respectively.

Figure 10 displays the power spectrum of a measured timetrace of a single gold nanoparticle in an aqueous medium. At higher frequencies (*red*) an almost horizontal behavior is found. The regime can be approximated with the following formula:

$$y = a \cdot x^b \tag{3.3}$$

The parameter *b* can be determined to -0.06. Consequently, white, uncorrelated noise is present. The lower frequency regime (pink) can be described with a $1/x^{1.6}$ behavior (*light blue*). Consequently, to successfully distinguish the actual signal from instrumental noise the following things should be considered:

1.) It should be measured at high frequencies.
2.) The characteristic time constant of the kinetic system under investigation should ideally be above 0.1 Hz.

Independent from this, a stable baseline signal with a minimal variance should be achieved. This can be realized by following several precautions:

1.) The resonance wavelength can shift due to temperature variation.[62] To avoid effects like heating or convection due to the strong light source optical filters were integrated into the beam path (see *Chapter 3.1*). As a consequence, only wavelengths up to 750 nm reach the sample whereas the energetic light in the infrared regime is cut out. Further, the Plasmon Fluctuation Setup itself should be stationed in a temperature controlled environment.
2.) Interreflection of the white light laser on scattering surfaces, particularly on metals, should be suppressed. Consequently, the light path was enclosed and all surfaces were covered with blackout materials.
3.) Another crucial point is the mechanical stability of the setup. A stabilizing "cage system" was built in other to prevent movement of the single devices relative to each other.

4.) Further, mechanical stress on the flow cell should be diminished. The tubing should be fixed with several pieces of tape. The change of the flowing fluid should be conducted carefully and it should be measured with a constant flow rate.[57]
5.) The resonance wavelength is highly dependent on the position of the sensing particle under investigation relative to the objective.[63] Therefore, drifts of the sample stage have to be suppressed.
6.) To minimize noise which originates from electronic devices (see remarks above) the whole Plasmon Fluctuation Setup should be switched on as soon as possible so that there is a maximal delay until the actual measurement takes place. This includes temperature cooling of the EMCCD camera. According to experience, a stable signal of the resonance wavelength over time is the sooner reached the longer the setup has been switched on.
7.) Beyond, the new software, *Nanocenter*, allows now a live monitoring of the measurement (see *Chapter 3.1*). When instability in the signal is observed it can be intervened at once and the measurement can be saved.

As a rule of dump, the signal gets stable after half an hour when all of these precautions are followed.

Further developments on the Plasmon Fluctuation Setup should focus on a further decrease of the setup noise. As identified the laser as strongest noise source[22, 57] an automated parallel white light alignment seems reasonable. Within this project an efficient strategy to couple out a small percentage of the laser beam for parallel measurement has to be found. Some possibilities like the usage of filters or a needle to introduce scattering have already been tested. However, the filters introduced interferences and the applied materials were not stable under the influence of high temperatures. A higher sensitivity can be achieved by the usage of nanoparticles with a high aspect ratio. However, the resonance wavelength shifts to the near infrared and other strategies to diminish heating effects have to be developed. Beyond, as kinetic processes are also temperature dependent the development of a temperature controllable flow cell construction appears path breaking.

Chapter 4

Sciene at its best provides us with better questions, not absolute answers.

-- Norman Cousins

4 Adsorption Behavior of Fibrinogen on the Single Molecule Level

4.1 Introduction

Whenever implants are inserted into our body complex tissue-biomaterial interactions occur.[64] As proteins adsorb on the surface within seconds the cells do not interact with the biomaterial itself but with the adsorbed protein layer. Consequently, unforeseen reactions might take place due to conformational changes of the adsorbed proteins and changes in the orientation of their functional sites.[65] The blood plasma protein fibrinogen (molecular weight: 340 kD) plays a central role in blood coagulation[66] and platelet adhesion[67] which leads to thrombogenesis. It is present in the circulatory system at a concentration of 2.6 mg/ml[68] and thus plays a central role in tissue-biomaterial interactions. The investigation of conformational changes of fibrinogen after adsorption is sophisticated since the protein shows a unique shape (see *Figure 11a*). It was firstly characterized by Hall and Slayter[69] and can be described as a covalent dimer of 2 fibrin molecules with a total length of 48 nm. The D domains with a mean diameter of 6.5 nm are connected with each other through a central E domain which is 5 nm in size (see *Figure 11b*).[70] This so called trinodular structure has been visualized with high resolution by Atomic Force Microscopy.[71] Beyond, fibrinogen molecules show a high flexibility.[72]

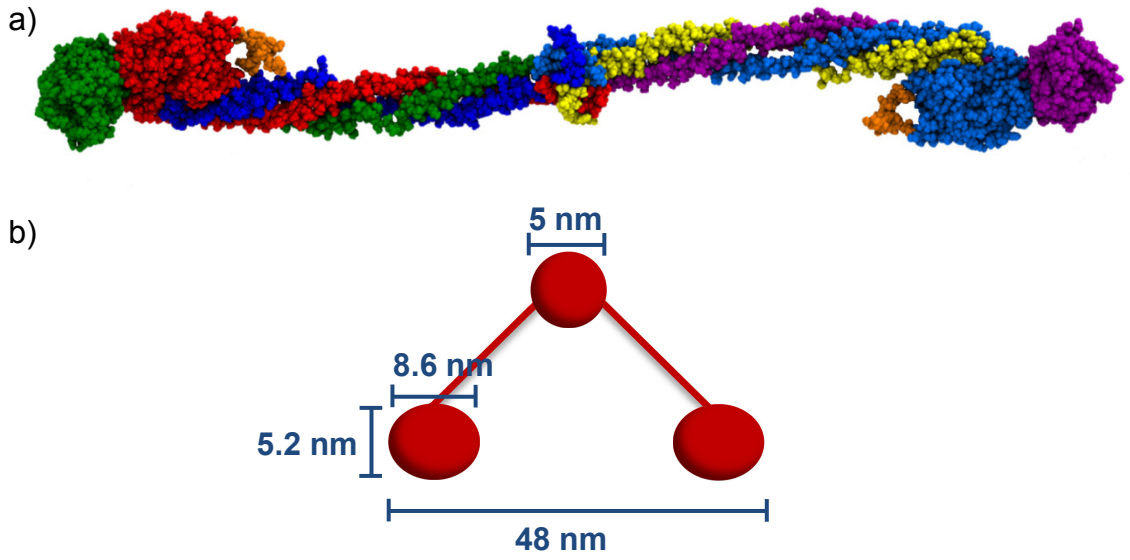

Figure 11. Fibrinogen molecule. **a)** A 3D visualization is shown. The figure was kindly provided by Stephan Köhler, workgroup of Prof. Schmid/ University of Mainz.[73] **b)** Schematic representation including the sizes of the domains. Dimensions are taken from Agnihotri *et al.*.[70]

Because of its biological relevance it is of most importance to develop methods to study adsorption behavior of fibrinogen on materials for biomedical applications. Many methods cannot characterize adsorbed protein layers in their natural form due to necessary sample preparations.[65] Atomic Force Microscopy (AFM) on the contrary allows to study proteins under physiological conditions at the molecular level.[74] However, it does not resolve the adsorption process itself. Recently, Ament *et al.*[22] could follow adsorption of single fibronectin molecules on the gold surface of the plasmonic nanorod in real time (see *Figure 12a*). Beside of the fact that single molecule detection is the ultimate goal in the field of sensor development[56] this resolution finds application to investigate conformational changes of biomacromolecules[75] and to study different kinds of binding events.[76] Time-resolving the adsorption process itself a plasmonic redshift was observed within 1-2 seconds which led to the conclusion that denaturation[77-79] was monitored (see *Figure 12b*).

I applied this technique to follow the adsorption of fibrinogen on the gold surface of the sensor on a single molecule level and present the results within this chapter. The results are interpreted in context of the existing knowledge about the stages of fibrinogen adsorption

which is presented in *Chapter 4.2* and should act as a further hint to complete this model. The procedure for the data analysis was conducted according to Ament *et al.*.[22]

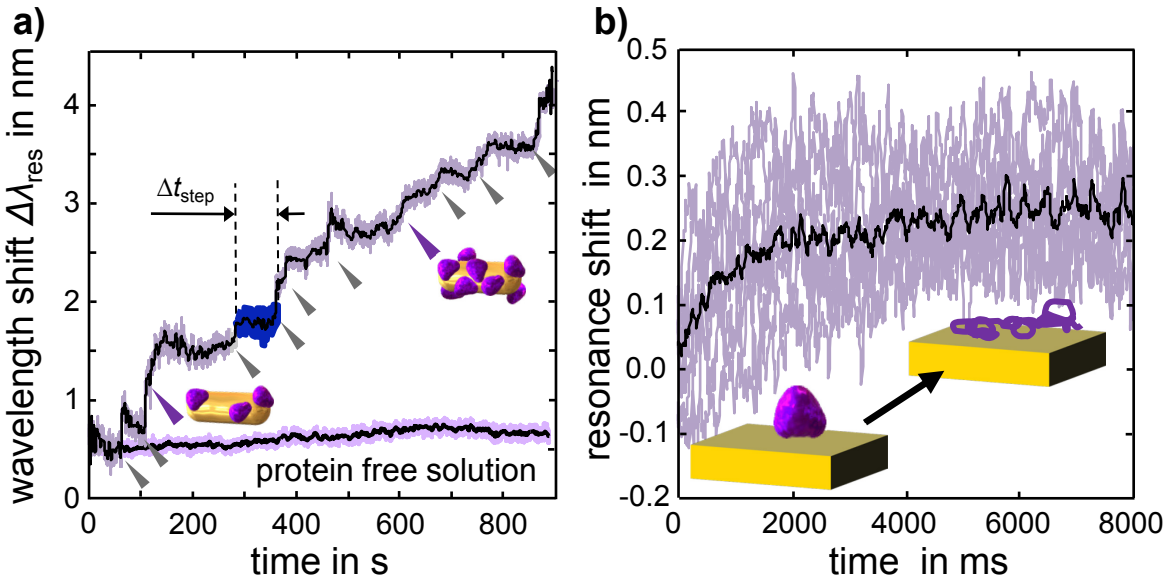

Figure 12. Fibronectin adsorption. **a)** Timetrace of the resonance wavelength of a single gold nanorod when a protein solution containing 1.25 µg/ml of fibronectin is introduced. The black curve corresponds to the FFT denoised signal. One sketch indicates the adsorption of one single fibronectin molecule. In comparison, in a protein free solution no increase in the resonance wavelength is monitored. **b)** 8 individual adsorption events from one timetrace (purple) are averaged (black). An exponential increase of the resonance wavelength is observed. Both figures originate from literature [57].

4.2 Theory

4.2.1 Protein Adsorption

Protein adsorption can be regarded as a complex process. Therefore, the properties of all components of the system under investigation have to be considered: the protein, the surface and the surrounding medium.[68] Proteins are hydrophilic as they are defined by its charged amino acid subunits which arrange at the outside of the protein.[80] Consequently, protein-material interactions occur via the end groups or rather via the collectivity of protein end groups and accumulated molecules of the medium. Due to Gibbs law

$$\Delta_{ads}G = \Delta_{ads}H - T\Delta_{ads}S \tag{4.1}$$

the free energy G is negative when the product of the temperature T and the entropy S is bigger than the enthalpy. When this is realized spontaneous adsorption occurs.[81] The size of the protein also plays an important role. As bigger proteins show more binding amino acids on the outside they are obviously capable to interact better with the surface. However, in a competitive situation between proteins of different sizes smaller ones adsorb first which are only replaced by bigger competitors afterwards. This effect is called Vorman effect.[82]

As proteins can be regarded as hydrophilic there is a higher affinity for hydrophobic surfaces. It can be distinguished between soft proteins which can adsorb to both hydrophobic and hydrophilic surfaces and hard proteins which show a high preference for hydrophobic surfaces.[83] The surface can mainly be characterized by the kind of material, its roughness and texture. For example, metals which are often integrated in implants show a negatively charged free electron cloud.[23] In general, this leads to a low affinity for proteins. However, in our bodies metals tend to corrode[84] and the resulting oxidation can increase the affinity. In general, a higher roughness leads to more binding sites and thus to a higher adsorption rate.[85]

On the surface, strong conformational changes of the proteins occur. This phenomenon is discussed using the example of fibrinogen in the following chapter.

4.2.2 State of the Art: Adsorption Behavior of Fibrinogen

This chapter gives a short summary about what is already known about the adsorption behavior of fibrinogen on the single molecule level with a focus on the timescales at which the different stages of the adsorption process (see *Figure 13*) occur. It is well known that interactions between proteins and surfaces and the resulting conformational changes[86] are strongly influenced by surface conditions.[87-89] Consequently, the adsorption behavior of fibrinogen has been studied on different kinds of surfaces. Often, it was distinguished between hydrophobic and hydrophilic surfaces.[68, 90, 91] Fibrinogen adsorption occurs on both kinds of surfaces but there is a slightly higher affinity for hydrophobic surfaces where the degree of denaturation is higher.[68] On hydrophobic surfaces, fibrinogen unfolds and increases the favorable interactions with the substrate whereas in case of a hydrophilic

surface, angle narrowing between the two D domains occurs.[90, 91] As a side remark: The surface of clean gold is regarded as hydrophilic,[92] whereas colloidal gold can be classified as hydrophobic.[93, 94] In general, at low concentrations the time between single adsorption events is higher and thus, the proteins have more time to unfold and occupy a larger area on the surface before another molecule adsorbs nearby.[91] Hemmerle *et al.*[95] stated that the adsorption occurs through the D or E domains. With the help of the force spectroscopy mode of Atomic Force Microscopy (AFM) they found out that the minimal interaction time for a fibrinogen molecule is about 50-200 ms. Ongoing simulations suggest a high flexibility between the two D domains in the nanosecond regime.[73] Furthermore, the complete denaturation process is known to take minutes up to hours. Agnihotri *et al.*[70] observed structural changes of fibrinogen during adsorption by measuring the height of the three domains via AFM. Over time, these heights decreased due to spreading of the protein and its trinodular structure was lost within 130 min. Beyond, experimental[96] and theoretical studies[97] come to the conclusion that monolayer instead of multilayer adsorption occurs.

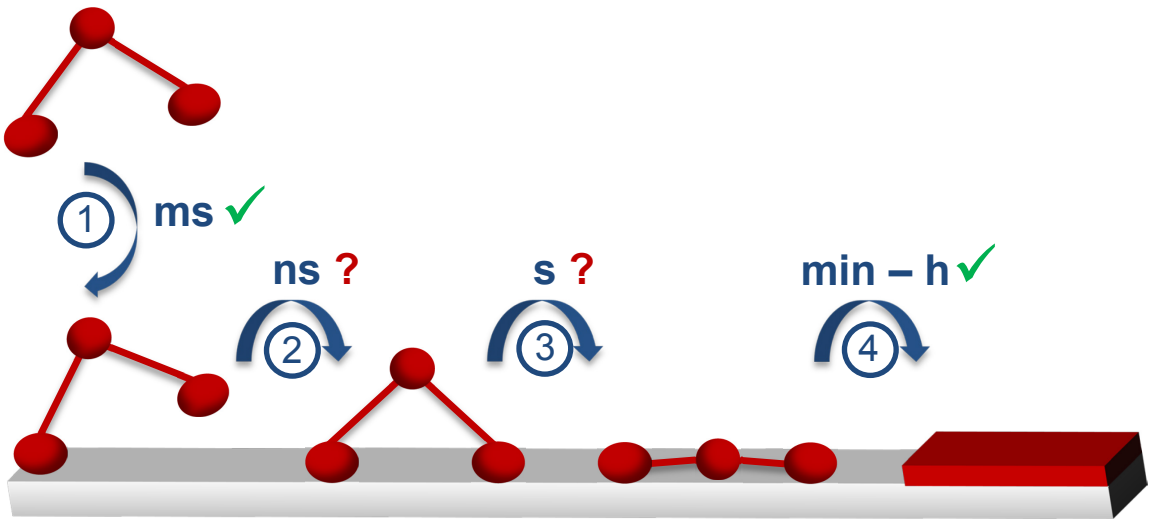

Figure 13. Schematic representation of different stages of fibrinogen adsorption on a solid surface. Stage 1: Protein attaches on the surface. Stage 2: Two domains are attached. Stage 3: Middle domain attaches to the surface. Stage 4: Protein is completely denaturized.

Bringing all this information together, this leads to a classification of the fibrinogen adsorption process into four different stages (see *Figure 13*). First, adsorption occurs via the D or E domain of the protein. This is known to happen within milliseconds[95] and appears

as one step in my presented experiments. As the two D domains are quite flexible in solution[73] the second D domain probably adsorbs at the nanosecond timescale (stage 2) and is (currently) not resolvable with the Plasmon Fluctuation Setup. At the moment, there is no information available at which timescale the bending of the middle domain towards the surface and thus the collapse of the trinodular structure occurs (stage 3). On the contrary, the whole denaturation process is known to take place within hours (stage 4).[70]

4.3 Experimental Details

Materials Phosphate buffered saline (PBS), sodium chloride and sodium thiosulfate were bought from *Sigma* and dissolved in de-ionized water. Right before application, the buffer was filtered (0.02 µm pore size). Fibrinogen (341576-100 MG) was purchased from *Merck* and dissolved in PBS. Therefore, a solution with a concentration of 1 mg/ml was dialyzed for 12 hours. The filter size was 3.5 MWCO (molecular weight cut-off). For measurements, dilutions of 5-10 µg/ml were used. As sensors, gold nanorods with a mean resonance wavelength λ_{res} of 635 nm and mean dimensions of 35 nm x 78 nm (for further details see *appendix C1*) were used. The synthesis was conducted according to Nikoobakht *et al.*[98] (for further details see *appendix A1*).

Sample Preparation The flow cells were self-made and consisted of a glass capillary with dimensions of 100 mm x 2 mm x 0.1 mm affixed to flexible tubes. The flow cells were built into the microscope with immersion oil deposited between flow cell and prism. For immobilization of the gold nanorods on the glass surface a 1M solution of sodium chloride was used. To remove the surrounding cetyl trimethylammonium bromide (CTAB) and silver bromide, the particles were incubated with a solution of sodium thiosulfate (50 µg/ml) for 45 min and after that rinsed with water and PBS. After stability of the resonance wavelength was reached, the fibrinogen solution was introduced. The measurements were conducted under continuous flow generated through gravitational force.

Setup For measurements the microscope as described in *Chapter* 3 was applied. The exposure time was amounted to 5-15 ms and the readout time to 3.78 ms. The resonance wavelength of one single gold nanorod was monitored over time (timetrace).

Data Evaluation The data analysis was conducted according to Ament *et al.*.[22] Single adsorption events appeared as discrete steps in the timetrace which were recognized via histograms and approximated through multi-Gaussian fits. Thereby, the size of one step, $\Delta\lambda_{step}$, corresponds to the difference between the maxima of two neighboring peaks. The time between two steps, Δt_{step}, equals the area. To determine the time of two following steps the parameters *a*, *b* and *c* of the Gaussian fit were extracted:

$$f(x) = a \cdot \exp(-\frac{x-b^2}{c}) \tag{4.2}$$

As the full width at half maximum, *FWHM*, is related to the standard deviation of a Gaussian distribution as follows:

$$FWHM = 2 \cdot \sqrt{2ln2} \cdot \sigma \tag{4.3}$$

the *FWHM* can be determined:

$$FWHM = 2 \cdot \sqrt{ln2} \cdot c \tag{4.4}$$

Then, the number of counts, N_{counts}, can be calculated:

$$N_{counts} = a \cdot \frac{FWHM \cdot B}{\Delta\lambda} \tag{4.5}$$

$$\text{with } \Delta\lambda = \lambda_{max} - \lambda_{min} \tag{4.6}$$

Thereby, *B* represents the binning used for calculation of the histograms whereas λ_{min} and λ_{max} represent the minimal and maximal resonance wavelength within the applied timetrace sequence respectively. Finally, the time between two steps corresponds to:

$$t = N_{counts} \cdot t_{wait} \tag{4.7}$$

t_{wait} is the sum of exposure time and acquisition time.

4.4 Results and Discussion

For the investigation of single protein adsorption events, the gold nanorods were immobilized on the surface of the glass capillary. Spectra of one single particle were acquired and the changes in the resonance wavelength over time were monitored (timetrace). As proteins show a refractive index of about 1.5[99] the adsorption led to a red shift in the resonance position and adsorption isotherms could be followed. By applying protein solutions in quite low concentrations the critical point can be reached were discrete steps within one timetrace appear.[22, 57] *Figure 14* shows a timetrace following the protein adsorption while rinsing with a buffer solution containing 5 µg/ml of fibrinogen. For better visualization, a display window is shown where discrete steps are illustrated by sketches. Further adsorption isotherms can be found in *appendix E*. Discrete steps were identified through histograms. Thereby, the peaks were approximated with a multi-Gaussian fit. The difference in the maxima of two neighboring peaks corresponds to the step size, $\Delta\lambda_{step}$, and the area equals the time between two steps, Δt_{step}. This strategy was developed by Ament *et al.*.[22, 57] Alternatively, a step-finding algorithm could be utilized. For example, Zijlstra *et al.*[100] who also developed a method with the sensitivity for single protein detection based on photothermal imaging used a step-finding algorithm developed by Kerssemakers *et al.*.[101] However, when applied this algorithm on the data of only a less accurate determination of the discrete steps could be achieved.

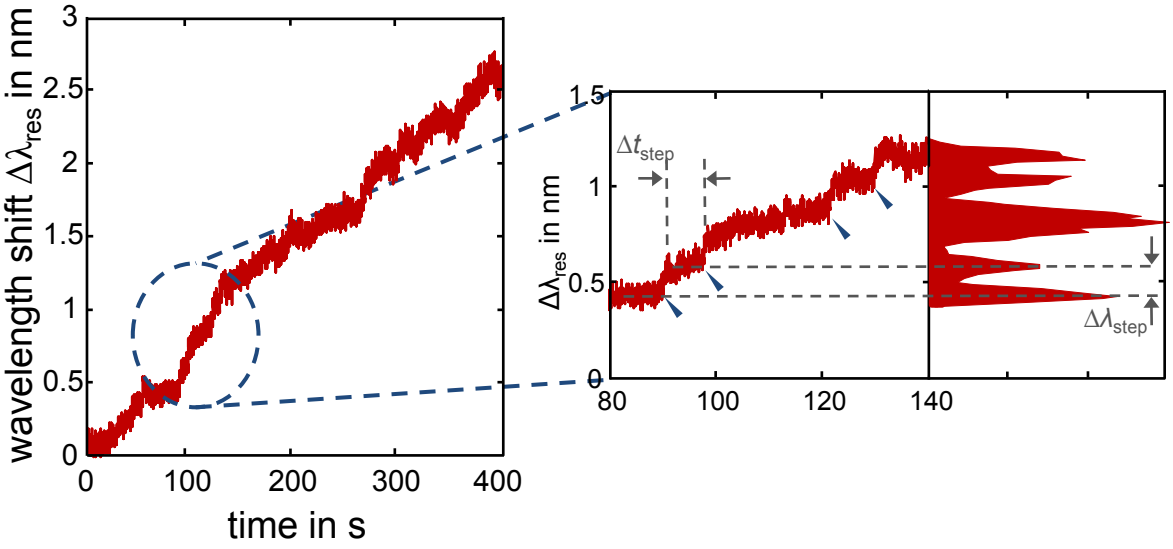

Figure 14. Adsorption isotherm during incubation with fibrinogen. A timetrace of the resonance wavelength of a single gold nanorod during attachment of single fibrinogen molecules (left) is shown. A concentration of 5 µg/ml was applied. For better visualization, a display window is shown (right). The sketches mark the position of discrete steps in the resonance wavelength which were identified through the corresponding histogram. The time between steps, Δt_{step}, and the step size, $\Delta\lambda_{step}$, were determined and evaluated.

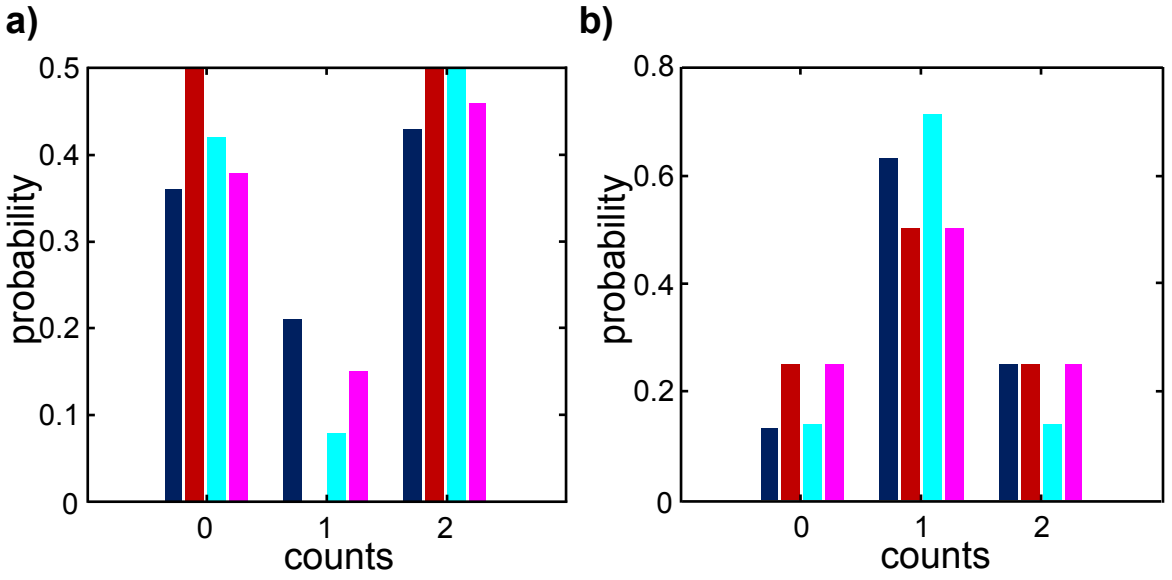

Figure 15. Evaluation of the time between steps. **a)** Probability of the number of steps within the mean time between two steps for 4 different timetraces. **b)** Probability of fibrinogen attachment events under the assumption that 2 steps directly behind each other are regarded as one adsorption event.

In order to investigate the time between events the mean time between steps within one timetrace was calculated. Thereafter, the trace was divided into equidistant sections and number of steps was counted (see *Figure 15a*). An irregularity in the time between steps was

found as it becomes apparent, that with most probability either 0 or 2 events occur within one section. Or in other words: a first short time sequence is followed by a second, longer time interval. If steps appearing within one equidistant section are grouped, are thus regarded as one unit and the described procedure is applied once more (see *Figure 15b*), a Gaussian distribution is found (see *appendix E*, *Figure 46*). These results allow a classification into two different kinds of time intervals. The first time interval corresponds to the time between two following steps within one time section. The second one equals the time between two neighboring units. *Table 1* gives an overview about the values of these intervals for different concentrations.

Table 1. Classification of the time between steps into two different time intervals. The first one corresponds to the time between two following steps within one time section. The second one equals the time difference between two neighboring units. The values are shown for different concentrations. For better comparison, only the respective first five time intervals are considered in the second case.

concentration in µg/ml	5	7.5	10
time interval 1	6.9	7.9	7.3
time interval 2	43.4	33.7	22.3

The first time interval is independent from concentration while the second one decreases when higher concentrations are applied. To further investigate the concentration dependency of this second time interval the correspondent attachment frequencies were calculated and compared with theoretical expectations. The attachment frequency is dependent on the utilized concentration of the protein and can be calculated according to *formula 4.8*.[102]

$$N = c \cdot A_{rod} \cdot \sqrt{D \cdot t} \tag{4.8}$$

Thereby, N is the number of adsorbed proteins after time t. D describes the diffusion constant. For calculations, a literature value of $1.8 \cdot 10^{-7}$ cm^2/s[103] was applied. A_{rod} represents the surface area of the rod. In principle, the diffusion constant D can also be calculated according to the Einstein-Stokes law:

$$D = \frac{k_B \cdot T}{6 \cdot \pi \cdot \eta \cdot r} \tag{4.9}$$

Thereby, k_B represents the Boltzman constant, T the temperature, η the viscosity and r the protein radius. As fibrinogen does not have a spherical but a trinodular structure a mean radius is difficult to determine and thus the literature value was applied. *Figure 16* shows the theoretical values for the attachment frequency in dependence of the concentration (blue). The time between events according to experiment were extracted from measured timetraces with concentrations ranging from 5-10 µg/ml (red). Within this concentration regime, adsorption occurred in a way so that a certain number of steps became visible within a reasonable measurement time on the one hand. On the other hand, the probability that more than one protein adsorbs at the same time was low. In all cases, only the first five events were considered.[104] An event is defined as unit of the steps which occur within one section as described above. With increasing concentration the attachment frequency increases, too. Derivations between experimental and theoretical values could arise from the fact that no probability of adsorption was considered.[57]

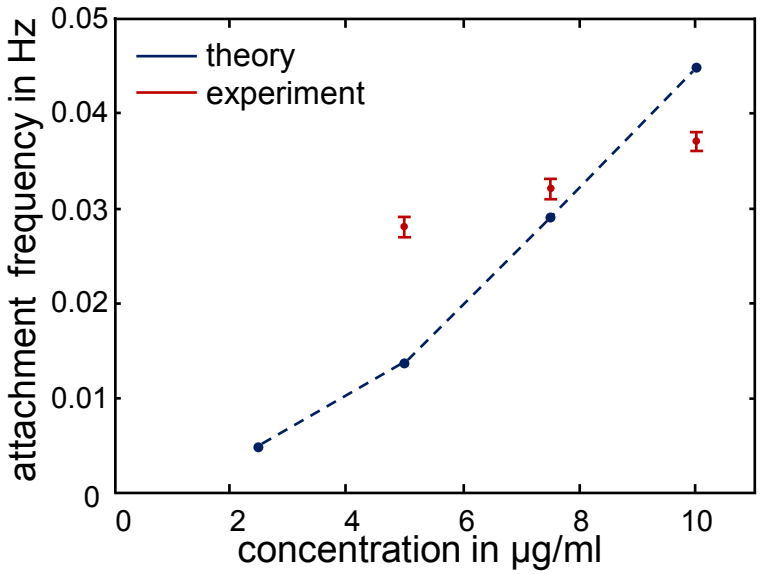

Figure 16. Dependency of the attachment frequency on the utilized concentration. The figure shows measured data (red) as well as theoretical data (blue). The error bars correspond to the accuracy of the determined values for the time values. The theoretical data points were calculated with a MATLAB script, see literature [1].

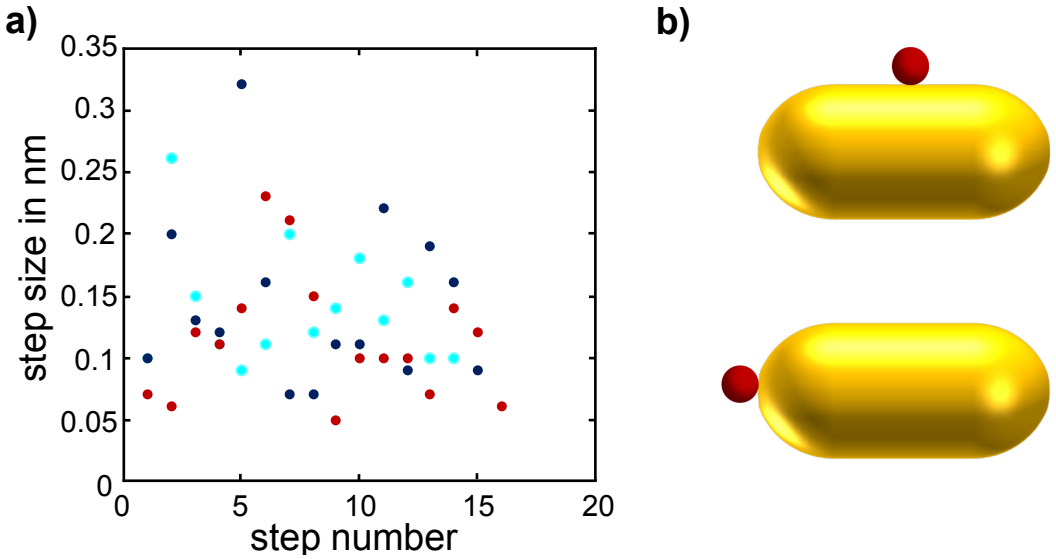

Figure 17. Evaluation of the step size. **a)** Step sizes extracted from three different timetraces. **b)** The shift of the resonance wavelength of a gold nanorod is dependent on which position protein adsorption occurs. The tip is in general more sensitive than the side of the rod.

All in all, the two different time intervals can be characterized as shown in *Table 2*. The first time interval is invariable in time and independent of the concentration. Slight variations in the value probably originate from differences in the utilized sensor size. The second time interval is variable in time and dependent on the concentration as well.

Table 2. Characterization of the two time intervals in means of time and concentration.

time interval	1	2
time	invariable	variable
concentration	independent	dependent

This in turn leads to the assumption that 2 steps directly behind each other belong to the adsorption of one single fibrinogen molecule or in other words the adsorption event of one single fibrinogen molecule is resolved as a 2-step process.

The size of one step is dependent on the size of the adsorbed particle. As the D domains of fibrinogen have slightly other dimensions than the E domain (compare with *Figure 11b*) the shift height can in principle provide information about which domain adsorbs first or in

which order. However, the height of the shift is also dependent on the attachment position (see *Figure 17b*). As fibrinogen is nearly as long as the sensor itself its domains certainly adsorb on entirely different positions of the rod. This makes the examination if there is any history dependency in the step size difficult (see *Figure 17a*).

4.5 Conclusions and Outlook

In summary, the adsorption of single fibrinogen molecules was followed by monitoring the resonance wavelength of single, plasmonic nanorods over time. Discrete steps in the timetrace were identified by histograms and the times between steps as well as the step sizes were calculated. Statistics on the time between steps led to the assumption that the adsorption process is resolved as a two-step process. Putting this result into context with the existing knowledge about the adsorption behavior of fibrinogen (see C*hapter 4.2*) this leads to the assumption that the observed two-step process in my experiments arises from stage 1, the adsorption of the protein itself, and from stage 3, the bending of the E domain towards the surface which would then occur within milliseconds. However, up to now there is no publication about the timescale of this third stage. Thus so far, this is only a hypothesis which will be approved or disapproved by ongoing simulations.

All in all, I have shown that the Plasmon Fluctuation Technique does not only reach the limit of single-molecule detection[22] but can also be applied to study conformational protein dynamics. In comparison to other techniques, this method shows a high signal-to-noise ratio without the necessity of labeling the target with a fluorescent dye. This opens a window to study these conformational changes under different conditions such as different surface modifications or environments and get a deeper understanding about biological processes.

Chapter 5

There is an infinite number of wrong ways to get the right answer.

-- A .D. McLean

5 Equilibrium Coverage Fluctuations as New Method to Quantify Adsorption Kinetics

5.1 Introduction

Surfactants play an important role in our daily life. There are a lot of useful applications like cosmetics, pharmaceuticals, detergency, wetting films or stabilization of dispersions.[105, 106] Consequently, it is necessary to characterize and quantify surfactant kinetics. Surfactant behavior in solution has already been intensely investigated.[107] The calculation of the on- and off-rates which describe the exchange of surfactant monomers between micelles and solution can be extracted by temperature-jump and pressure-jump experiments[108] in combination with theoretical models.[109] On the contrary, quite little is known about surfactant behavior at interfaces.[107] Ward *et al.*[110] set basis to study surfactant behavior at liquid-liquid as well as at air-liquid interfaces by measuring the time dependency of boundary tensions of solutions. Information about surfactant adsorption and desorption at the solid-liquid interface has so far been collected through a various number of techniques. Turner *et al.*[106] used Neutron Reflection (NR) and Attenuated Total Reflection Infrared Spectroscopy (IR-ATR) to quantify the adsorbed amount and position relative to an interface of adsorbed molecules. To identify different types of structures surfactants can

form on a solid surface Atomic Force Microscopy (AFM) has been applied.[107, 111-113] While NR and IR-ATR do not provide any information about surfactant kinetics AFM allows some indirect quantification of the longetivity of surface micelles.[112, 114, 115]

To quantify the rate constants which fully describe the adsorption kinetics adsorption and desorption are usually followed over time (adsorption isotherms). The change in the surface coverage can be monitored by several techniques. Appling quartz crystal microbalance (QCM) frequency changes are monitored over time.[116] Optical techniques like ellipsometry (ELL)[117] or surface plasmon resonance (SPR)[118-120] quantify surface coverage via changes in the optical thickness. Cantilever Arrays have also been used recently.[121] The resulting adsorption isotherms are then fitted with the corresponding rate equation. However, this method has to deal with several disadvantages. As mentioned above, the experiments have to be conducted with a high flow rate to avoid mass transfer interference. Second, long term drifts in the measuring signal falsify the results. Third, the available surface function (ASF) which is crucial to mathematically describe the adsorption isotherms cannot be expressed analytically. Forth, at higher coverages when the so called *jamming limit* is overcome adsorption is expressed in a 2-step process. However, it is not realistic to measure this second step as this effect occurs at a timescale of around 10^6 s.[122] Levchenko *et al.*[105] measured the adsorption on and desorption from self-assembled monolayers on gold of sodium dodecyl sulfate vi a SPR. Thereby, a lot of effort was put on avoiding mass transfer interference through the utilization of high flow rates and the kinetics could only be described via half-times and initial rates as the Langmuir equation could not describe the experimental data. Further, Clark *et al.*[107] used attenuated Total Reflectance Fourier Transform Infrared Spectroscopy (ATR- FTIR) to quantify adsorption kinetics of tetradecyltrimethylammonium bromide (CTABr). They analyzed surfactant exchange processes between C_{14}TABr and perdeuterated C_{14}TABr-d_{38}. Unfortunately, these experiments also suffer from mass transfer complications. All in all, a huge variety of calculated rate constants to describe surfactant adsorption on solid interfaces exists. While some researchers believe that equilibrium of surfactant adsorption is reached within hours[123, 124] others are convinced that the process is much faster and equilibrium is reached within seconds.[125] At least, there is an agreement that the rate constants are slower than the

corresponding rates in bulk which can result from the fact, that the exchange process in itself is slow or that the desorption is hindered through surface aggregates.[107]

Consequently, there is a need for a new technique to quantify the rate constants which overcomes the described limitations. One novel approach could be to observe coverage fluctuations in equilibrium. This strategy has already been investigated theoretically with the help of Monte-Carlo simulations in 2005 by Prof. Janshoff.[126, 127] Nevertheless, no sensor technology has so far shown a sufficient signal-to-noise ratio to demonstrate this principle experimentally.

In the following chapters I will first give an introduction to equilibrium coverage fluctuations (see *Chapter 5.2.1*) and I will give an overview about what is already known about the adsorption behavior of surfactants (see *Chapter 5.2.2*). In the experimental section, I will first evaluate the new method itself (see *Chapter 5.4.1*). Therefore, I will demonstrate the principle how the characteristic time constant τ can be determined through one single measurement. Second, I will discuss different ways for the calculation of the rate constants k_{on} and k_{off}. Further, possibilities to optimize the signal-to-noise ratio will be discussed. Then, in *Chapter 5.4.2* the adsorption behavior of the utilized surfactant sodium dodecyl sulfate will be investigated. Beyond, possible explanations why SDS causes a blue shift in the resonance wavelength of the sensor will be discussed in *Chapter 5.4.3*.

For data evaluation, the power spectra were calculated with the Welch algorithm. The script was developed by . At this point I also want to thank for helpful discussion.

5.2 Theory

5.2.1 Equilibrium Coverage Fluctuations

This chapter deals with a basic understanding of adsorption and desorption kinetics of particles on solid surfaces in solution. Further, it is shown how to quantify the characteristic rate constants via observation of equilibrium coverage fluctuations. This approach has been

developed and published by Eike Lüthgens and Andreas Janshoff. Consequently, the flowing description is based on their publication in *ChemPhysChem*[126] and on the dissertation of Eike Lüthgens.[127]

Already in 1918 a simple mathematical model to describe adsorption kinetics of small molecules was developed by Langmuir:[128]

$$\frac{\partial \Theta}{\partial t} = k_{on}\pi a^2 \rho_{bulk}(\Theta_{max} - \Theta) - k_{off}\Theta \tag{5.1}$$

with the analytical solution:

$$\Theta = \Theta_{eq}\left[1 - \exp(-\left(k_{on}\pi a^2 \rho_{bulk} + k_{off}\right)t)\right] \tag{5.2}$$

and

$$\Theta_{eq} = \Theta_{max}(1 + \frac{k_{off}}{k_{on}\pi a^2 \rho_{bulk}})^{-1} \tag{5.3}$$

Thereby, the time dependent surface coverage Θ is described by the rate constants k_{on} (adsorption) and k_{off} (desorption) as well as by the radius a and the density of molecules in solution ρ_{bulk}. Θ_{max} refers to the maximal coverage $\Theta_{max}=1$ and Θ_{eq} is the coverage at equilibrium. This formula is only valid, if only the formation of a monolayer is taken into account and if the particles do not interact with each other. For larger molecules like proteins these equations are not valid any more, as a particle can occupy several lattice sites. Consequently, a so called *available surface function* (ASF), $\Phi(\Theta)$, has to be considered:[129]

$$\frac{\partial \Theta}{\partial t} = k_{on}\pi a^2 \rho_{bulk}\Phi(\Theta) - k_{off}\Theta \tag{5.4}$$

The ASF can be regarded as a probability for a successful adsorption event.[127] This formula has to be solved numerically as no analytical solution is possible.[130] Schaaf and Talbot published the following solution for the ASF (here until third order):[129]

$$\Phi(\Theta) = 1 - 4\Theta + \frac{6\sqrt{3}}{\pi}\Theta^2 + 2.4243\Theta^3 \tag{5.5}$$

Up to a mean coverage of 10% the series expansion up to the first order is sufficient to describe adsorption kinetics. Until a mean coverage of 25% the series expansion up to the second order can be utilized. Taking the third order into account, mean coverage up to 35% can be described.[126, 127] For further details on derivations have a look at Ruckenstein[131] and Adamczyk *et al.*.[132]

Adsorption kinetics are drastically influenced by mass transport effects. This means that a depletion of adsorbents in the directly surrounding solution occurs. The adsorption kinetics are consequently limited through convection and diffusion and the calculated k_{on}- and k_{off}-values are falsified. The transport of the adsorbents to the surface is described through the rate constant k_{tr}. The transport is mathematically described by Adamczyk *et al.*[133, 134] through:

$$\frac{\partial \rho_{bulk}}{\partial t} + \vec{\nabla}\,\vec{\mathrm{j}} = 0 \tag{5.6}$$

with

$$\vec{\mathrm{j}} = -\vec{\mathrm{D}}\left[\nabla\rho_{bulk} + \frac{\nabla\Phi}{\mathrm{k_B T}}\rho_{bulk}\right] + \vec{\mathrm{j}}_{konv} \tag{5.7}$$

Thereby, $\vec{\mathrm{j}}$ describes the flux density vector, $\vec{\mathrm{D}}$ the tensor of diffusion, Φ the interaction potential of wall and particle whereas $\vec{\mathrm{j}}_{konv}$ refers to particle flux vector. Taking initial and boundary conditions into account the adsorption kinetics can be describes through:

$$\frac{d\Theta}{dt} = \frac{k_{on}\pi a^2 \Phi(\Theta)\rho_{bulk} - k_{off}\Theta}{1 + \frac{k_{on}}{k_{tr}}\Phi(\Theta)} \tag{5.8}$$

The characteristic rate constant k_{tr} can be calculated through:

$$k_{tr} = 0.78\left(\frac{\alpha_0 v D_\infty^2}{R^2}\right)^{1/3} \tag{5.9}$$

R refers to the radius of the flow cell and h is the distance of the delivery port to the place where adsorption takes place. The prefactor α_0 depends on the Reynolds number. For further details on the derivation of this formula have a look at the corresponding publications[133, 134] or at the PhD thesis of Eike Lüthgens.[127] In summary, several processes between absorbents and the surface are possible in the solution face as shown in *Figure 18*.

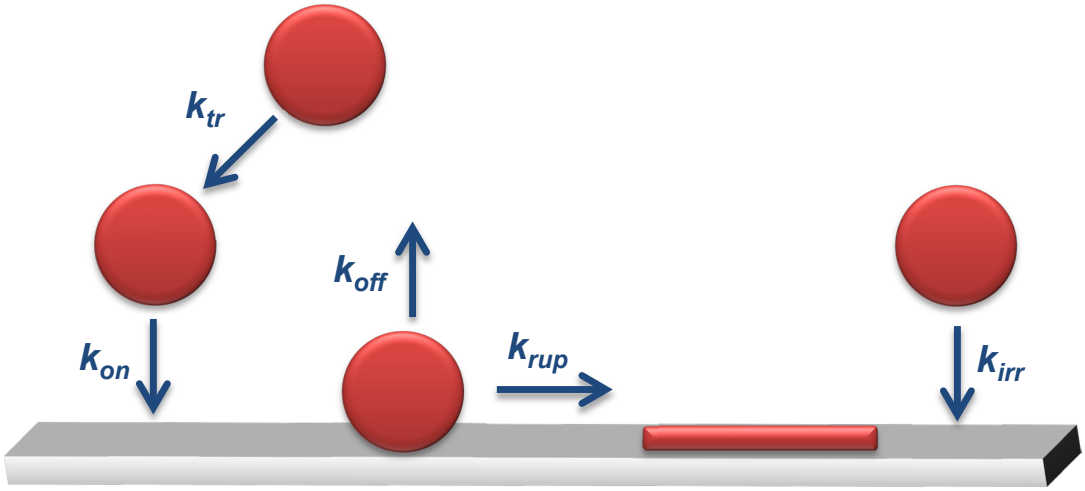

Figure 18. Schematic representation of the possible processes at the solid-liquid interface which are classified by different kinetic constants. The transport of a particle to the surface is described by k_{tr}. k_{on} describes adsorption on and k_{off} desorption off the surface. Irreversible binding is characterized by k_{irr} and structural changes of the adsorbed particle (e.g. denaturation) by k_{rup}. The figure is prepared in dependence on the dissertation of Eike Lüthgens.[127]

E. Lüthgens and A. Janshoff[126] proposed a new method to extract the rate constants within one single experiment: to measure adsorption and desorption processes in equilibrium. A reversible adsorption and desorption can be expressed through:

$$N_A \underset{k_{21}}{\overset{k_{12}}{\rightleftharpoons}} N_B \tag{5.10}$$

with

$$N_B = N - N_A \tag{5.11}$$

Thereby, N_A describes the number of molecules in the bound state and N_B the number of molecules in solution with the rate constants k_{12} and k_{21}. In the beginning, the sensor surface is empty:

$$N_A(t=0)=0 \tag{5.12}$$

N_A can be written as:

$$N_A(t)=N\frac{k_{21}}{k_{12}+k_{21}}\left(1-\exp\left[-(k_{12}+k_{21})\right]\right) \tag{5.13}$$

with the autocorrelation

$$\left\langle \delta N_A(t)\delta N_A(t+t^a)\right\rangle \propto \exp\left[-(k_{12}+k_{21})t^a\right] \tag{5.14}$$

and the power spectral density (PSD)

$$\left\langle \delta N_A(v)^2\right\rangle =\frac{c\cdot\tau}{1+(2\pi v\tau)^2} \tag{5.15}$$

with the amplitude c

$$c=4\cdot\left\langle N_A\right\rangle\cdot\left(1-\frac{N_A}{N}\right) \tag{5.16}$$

and the kinetic time constant τ:

$$\tau=(\hat{k}_{on}+k_{off})^{-1} \tag{5.17}$$

$$\text{with } \hat{k}_{on}=k_{on}\cdot c \tag{5.18}$$

Then the mean surface coverage can be expressed via:

$$\left\langle \Theta\right\rangle =\frac{\hat{k}_{on}}{\hat{k}_{on}+k_{off}} \tag{5.19}$$

Taking the ASF into account, the *formula 5.15* can be modified to:

$$\langle \delta N_A(\nu)^2 \rangle = \frac{4\tau \langle \Theta \rangle \pi a^2 (1 - 4\langle \Theta \rangle)}{A\left[1 + (2\pi\nu\tau)^2\right]} \tag{5.20}$$

with the radius of the adsorbates a and the surface area of the sensor A. τ is connected to the rate constants and the mean coverage $\langle \Theta \rangle$ via

$$\tau = (4\hat{k}_{on} + k_{off})^{-1} \tag{5.21}$$

and

$$\langle \Theta \rangle = \frac{\hat{k}_{on}}{4\hat{k}_{on} + k_{off}} \tag{5.22}$$

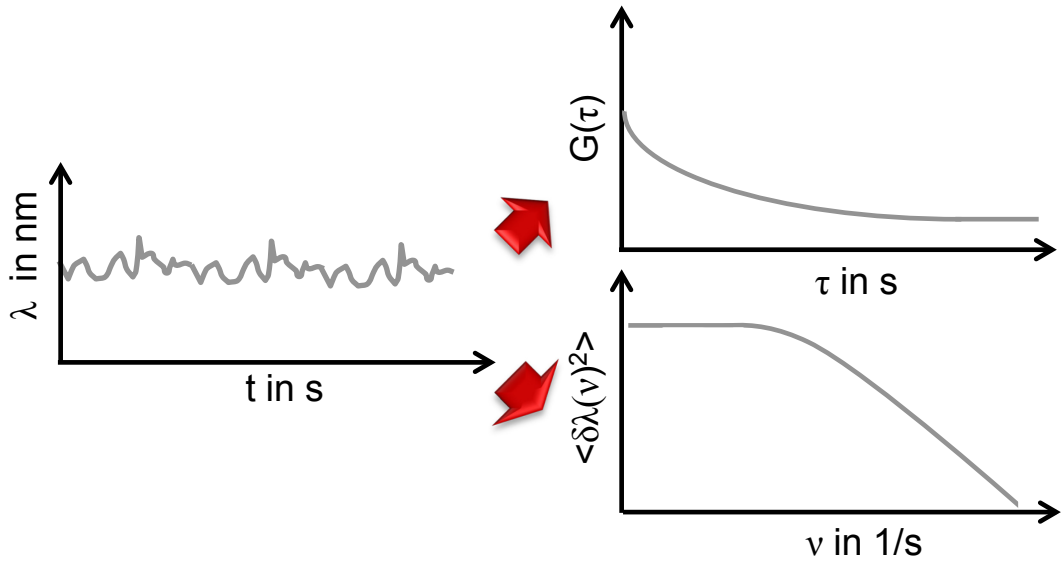

Figure 19. Schematic demonstration of how the rate constants can be determined through observation of equilibrium coverage fluctuations. From the temporal fluctuations (left) the autocorrelation and power spectrum can be calculated. The time constant τ can be calculated by either fitting the autocorrelation exponentially or by describing the power spectrum with a single Lorentzian. This figure was prepared in dependence on the dissertation of Eike Lüthgens.[127]

Mass transport does not have to be integrated into this formula as the flow rate only influences the thickness of the boundary layer but not the number of adsorbates that are

exchanged between sensor surface and solution at a certain unit of time. For further details on the derivation of these formula have a look at the PhD thesis of E. Lüthgens.[127] To determine the rate constants the measured signal following equilibrium coverage fluctuations can either be transformed into the frequency domain and the resulting power spectrum can be approximated with a single Lorentzian. Alternatively, the corresponding autocorrelation can principally be approximated with an exponential fit (see *Figure 19*).

In meantime Jokic *et al.*[135, 136] demonstrated in 2012 the influence of mass transport on theoretical basis and extended the Janshoff-model. Consequently, this argument has to be surveyed when evaluating this method experimentally.

Until today, no sensor technology has shown a sufficient signal-to-noise ratio to be able to resolve coverage fluctuations in equilibrium since the variance of fluctuations is indirect proportional to the sensor surface.[126] In ideal case, the size of the sensor should be close to the size of the particles/molecules under investigation (see *Figure 2*, *Chapter* 1).

5.2.2 Adsorption Behavior of Surfactants

In the following I present a summary of what has so far been found out on surfactant adsorption at the solid-liquid-interface (also compare with *Figure 20*). By enchanting the surfactant concentration the adsorption and desorption rates also increase.[105] Above the critical micelle concentration (CMC) the adsorbed amount as well as the rate constants remain constant.[105, 106] The adsorption is considered to be a 2-step process. First, diffusion from bulk solution to the subsurface occurs. Second, transport from the subsurface to the surface and subsequent adsorption takes place.[137] Following the adsorption over time, a biphasic behavior at low concentrations was observed. An initial fast rate is followed by a second, slower rate. Therefore, the Langmuir kinetic model does not give a good empirical approximation.[105, 106, 137] When the equilibrium state is reached the responding signal becomes independent of the flow rate.[105] High flow rates are necessary in experiments to determine the rate constants of the system under investigation, i.e. via SPR, so that mass transfer limitations are negligible. Therefore, many control experiments have to be conducted under variation of the flow rate.[105, 137] Surfactants can form micelles on solid

surfaces. The critical concentration of surfactants at which surface aggregates at solid-solution interfaces are formed (CSAC) is close to or at the CMC.[105, 137] Many details about micelle formation on surfaces are unclear.[106] There exist different types of surface micelles on solid surfaces like hemicylinders, cylinders, hemispheres or spheres. Charged surfactants preferably form hemimicelles on hydrophobic surfaces whereas on hydrophilic surfaces micelles form full micellar structures. The kinetics of adsorption and surface micelle formation for hemicylinders are believed to be a slower process than for adsorption and formation of hemispheres.[105] The presence of ions in solution decreases the critical micelle concentration. Besides, it has a big effect on adsorption behavior. Paria *et al.*[137] showed that the kinetics of sodium dedecylbenzenesulfonate differ when using the same surfactant concentration but a different concentration of potassium chloride. The rates were higher with increasing salt concentrations. Furthermore, they investigated the effect of valency of counterions and of coions.

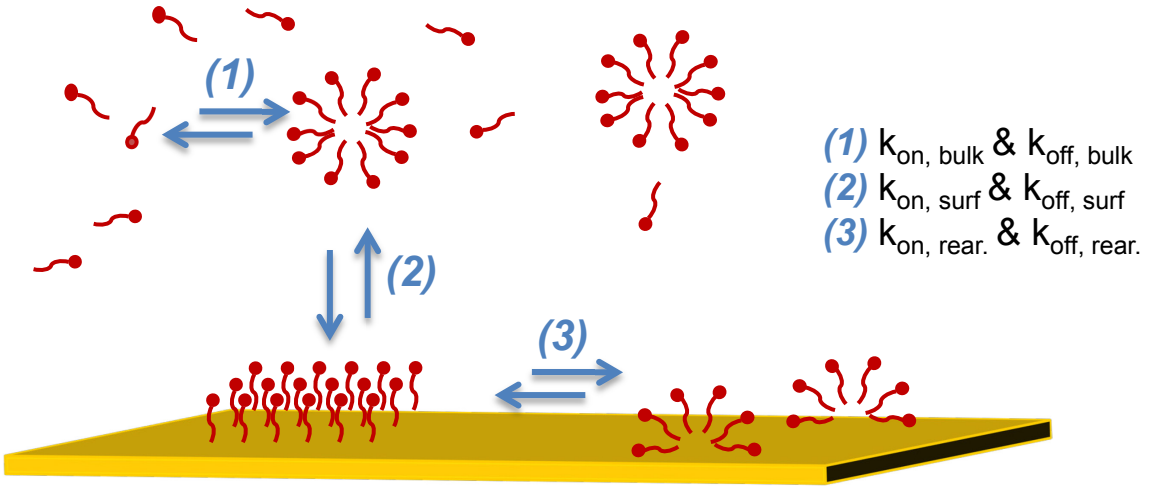

Figure 20. Schematic representation of the different processes of surfactants that occur in solution and at the solid-liquid interface. In solution exchange of molecules between bulk micelles and solution takes place *(1)*. At the solid-liquid interface adsorption and desorption occurs *(2)* as well as the formation of different kinds of surface micelles *(3)*. This figure was prepared in dependence of Levchenko *et al.*[105] and the dissertation of Eike Lüthgens.[127]

5.3 Experimental Details

Materials Phosphate buffered saline (PBS), sodium dodecyl sulfate (SDS), sodium chloride, sodium thiosulfate, cysteamine hydrochloride and 1-dodecanethiol were purchased from *Sigma.* Ethanol (absolute) was bought from *VWR*. PBS was dissolved in de-ionized water according to instruction. SDS was dissolved in PBS with an ultrasonic bath and filtered (0.02 µm pore size) right before usage. On the basis of a 34 mM stock solution, the dilutions applied in the experiments were produced. Gold nanorods of medium size were utilized as sensors. For further details on sensor dimensions and synthesis see *appendix A1* and *C1*.

Sample Preparation The flow cells consisted of a glass capillary (dimensions 100 mm x 2 mm 0.1 x mm) and flexible tubes. To match the reflective index, immersion oil was deposited between flow cell and half cylinder. The gold nanorods where first immobilized on the glass surface with a 1M solution of sodium chloride, incubated with a 50 µM solution of sodium thiosulfate for 45 min and then rinsed extensively with water. Sodium thiosulfate removes the surrounding cetyl trimethylammonium bromide (CTAB) and silver bromide of the nanorods. As model for hydrophobic and hydrophilic surfaces self-assembled monolayers of 1-dodecanethiol and cysteamine hydrochloride were applied respectively. Therefore, the thiols where dissolved in ethanol (concentration: 5 mM) and rinsed into the flow cell. The incubation took place over night (approximately 16 hours). To avoid evaporation of the solvent, the tubing was sealed with parafilm. Afterwards, the flow cell was rinsed with 10 ml of ethanol, 5 ml of water and then with PBS until the stability of the resonance wavelength was reached. From *Chapter 5.4.1.2* onwards all experiments were generally conducted with 1-dodecanethiol functionalized sensors. Exceptions are the experiments presented in *Figure 29* and *Figure 34*. The SDS solutions were introduced via gravitational flow and all measurements were conducted under continuous flow (flow rate: $3 \cdot 10^{-4}$ m/s), too.

Setup The microscope as described in *Chapter* 3 was used. The exposure times ranged from 3 ms to 10 ms with a readout time of 3.78 ms.

Data Evaluation For the determination of the fluctuation amplitude σ only short timetrace sequences of 60 s were considered. The timetraces were divided into 5 equidistant pieces and the mean values as well as the standard deviations were calculated respectively. For the calculation of the power spectrum the mean value of the resonance wavelength was determined and the value was subtracted. Then, the Welch algorithm was applied. Therefore, a timetrace is cut into several equidistant pieces with some overlap and the spectra are averaged. Usually, a segment length of 2^{14} data points and an overlap of 99% were chosen. The value of the time constant τ was extracted by fitting the power spectrum with a single Lorentzian. As the Lorentzian behavior of the measured signal slightly overlapped with the $1/x^{1.6}$ trend of the instrumental noise (see *Chapter 3.2*) the fit of one power spectrum was conducted several times under variation of the fitting boundaries and the averaged value and standard deviation are given respectively.

5.4 Results and Discussion

5.4.1 Equilibrium Coverage Fluctuations as New Method to Quantify Adsorption Kinetics

5.4.1.1 Principle

To demonstrate the principle of the determination of the rate constants through observation of equilibrium coverage fluctuations the gold nanorods were first immobilized on the surface of the glass capillary and then incubated with sodium thiosulfate to completely remove the CTAB layer which was indicated by a blue shift of 1.6 nm (the timetrace is displayed in *appendix F*, *Figure 48*). The surface of the sensor became hydrophobic.[93, 94] After monitoring the resonance wavelength of a single gold nanorod over time in PBS buffer as reference a solution containing 1.7 mM sodium dodecyl sulfate was introduced (see *Figure 21a*). On the one hand, PBS was utilized to increase the rate constants and thus to reduce the measurement time. On the other hand, a pH stable medium was necessary due to the surface modification of the sensor. The CMC of SDS in pure water is 8 mM[106] whereas in a 0.2 M solution of sodium chloride the CMC is reduced down to 0.9 mM (see *appendix F*).

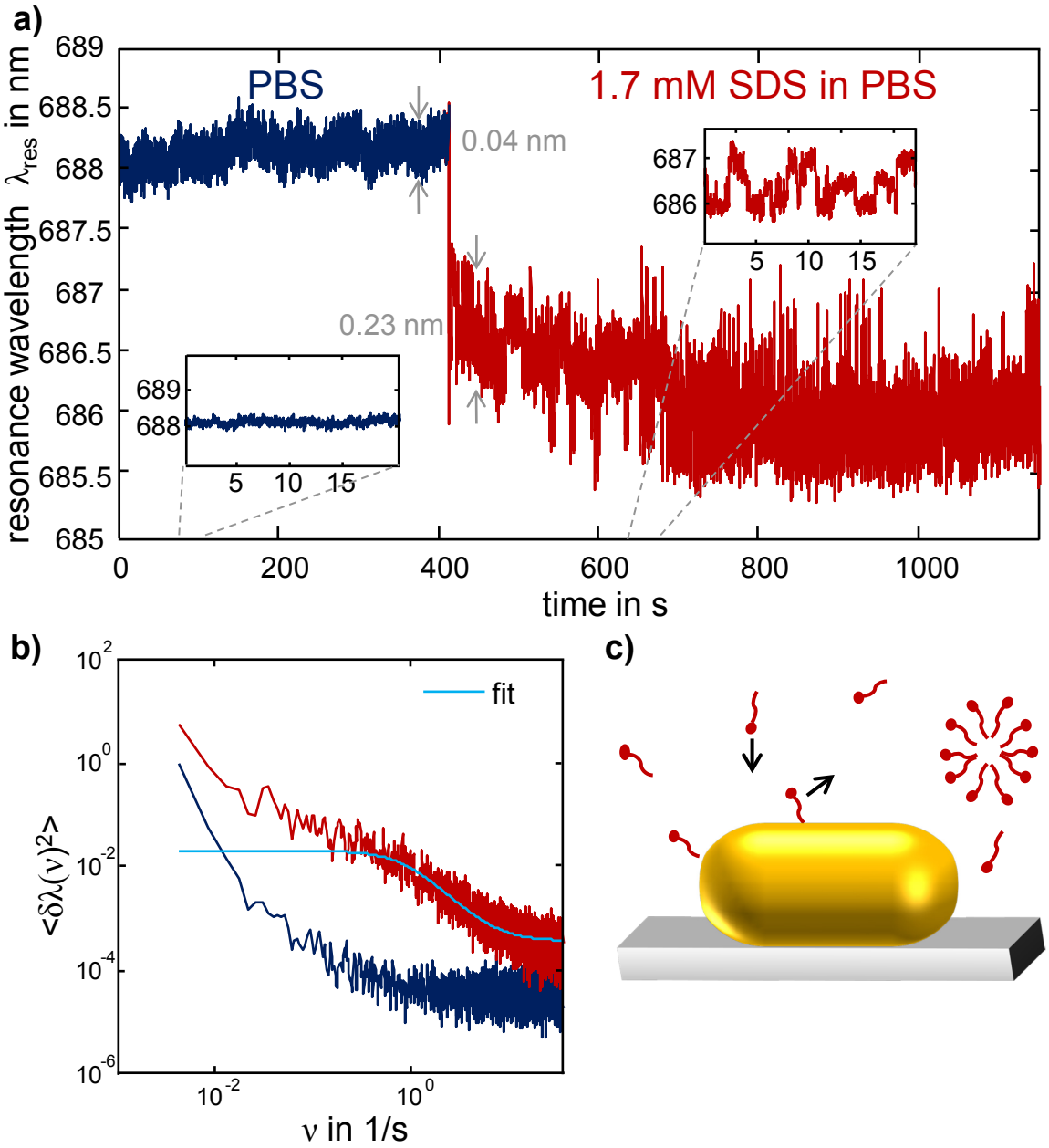

Figure 21. Adsorption of sodium dodecyl sulfate on the surface of a blank gold nanorod. **a)** Timetrace of the resonance wavelength of a single gold nanorod. It was first rinsed with PBS buffer (baseline, dark blue) and then a buffer solution containing 1.7 mM SDS was introduced. A blue shift and an increase in the fluctuation amplitude can be observed (red). The insets display magnifications of the baseline and of the equilibrium coverage fluctuations. **b)** The power spectrum of the equilibrium coverage fluctuations of SDS (red) can be described by a single Lorentzian (light blue). For comparison the power spectrum of the baseline in PBS buffer is shown (dark blue). **c)** Schematic representation of adsorption of SDS on the surface of the sensor. As colloidal gold is hydrophobic adsorption of SDS occurs via the alkyl tail.[105]

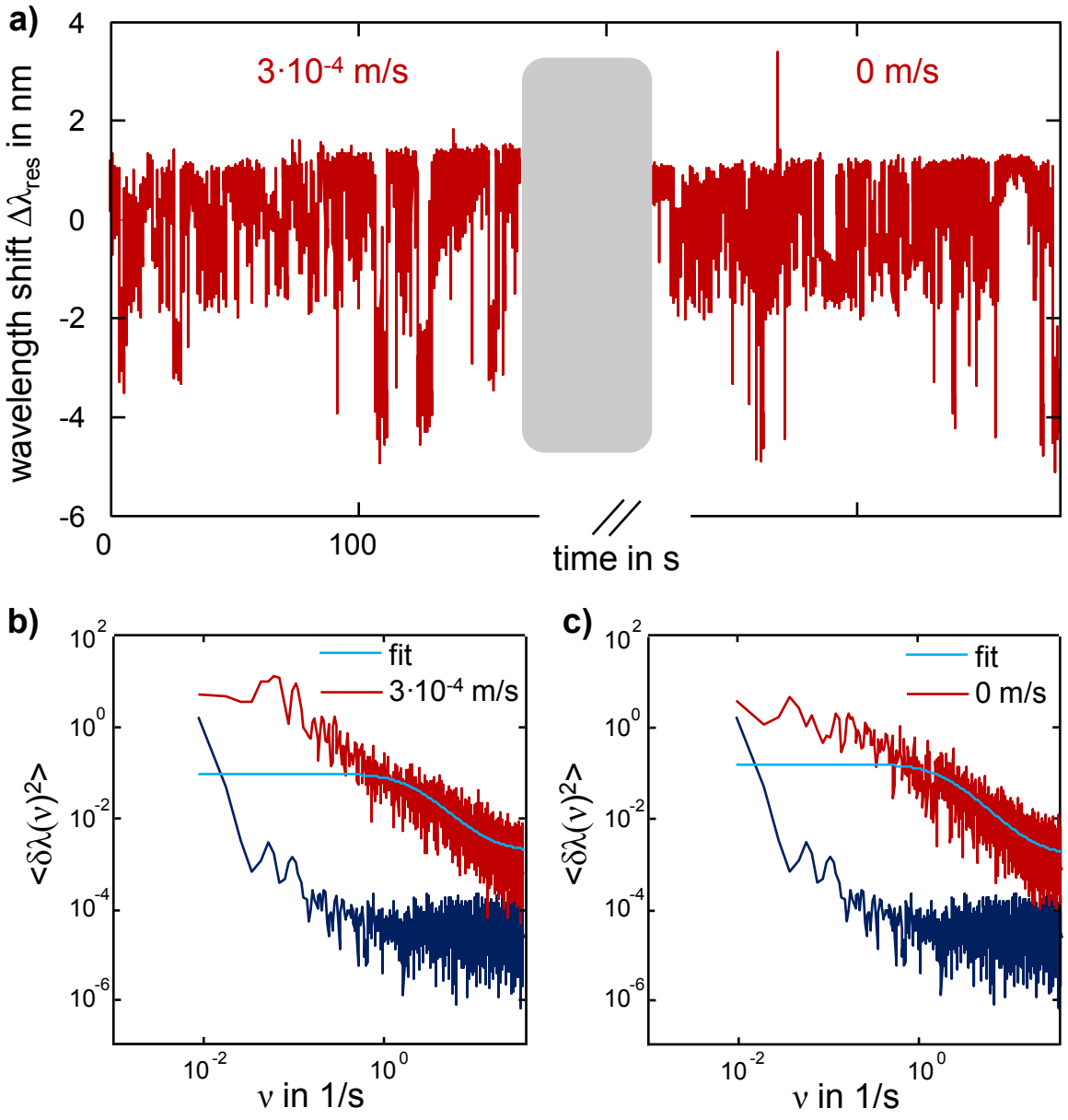

d)

flow rate in 10^{-4} m/s	noise in nm	τ in s
3	0.89 ± 0.34	0.09 ± 0.01
0	0.82 ± 0.23	0.09 ± 0.01

Figure 22. Adsorption of SDS in dependency of the mass transport. **a)** Timetrace of the resonance wavelength of a single, blank gold nanorod surrounded by a buffer solution containing 1.7 mM SDS. It was first measured under continuous flow with a flow rate of $3 \cdot 10^{-4}$ m/s (left). Then the flow was stopped (right). **b)-c)** The corresponding power spectra of the timetrace sequences (red) can be described by a single Lorentzian (light blue). For comparison, the power spectra of a baseline in PBS buffer are shown (dark blue). **d)** Overview of the calculated noise values and kinetic time constants.

A blue shift of 2.2 nm can be observed which indicates the adsorption of SDS molecules on the sensor surface. Furthermore, the fluctuation amplitude increases from 0.04 nm to 0.23 nm. The insets of *Figure 21a* display magnifications of the baseline and of the regime where SDS was introduced respectively. Fluctuations in the measured signal become visible. This effect arises from equilibrium coverage fluctuations[126] and the noise yields information about the time constant τ which can be extracted via Fourier transform. This is demonstrated in *Figure 21b*. The power spectrum can be described with a single Lorentzian[126, 127] (see *formula 5.15*) and the value of τ can be determined to 0.18 ± 0.01 s. According to model conceptions, adsorption occurs via the alkyl tail while micelles do not adsorb as a whole on hydrophobic surfaces (further discussion see *Chapter 5.4.2*).[105] This is schematically displayed in *Figure 21c*.

When Lüthgens *et al.*[126, 127] first described this detection scheme on theoretical basis the independence of mass transport phenomena was pointed out: In equilibrium, a certain number of adsorbates of the boundary layer adsorb and desorb on the sensor surface per time unit. Consequently, the flow rate only has influence on the thickness of the boundary layer but not on the number of adsorbing molecules. To survey this theory, the above described experiment was repeated under variation of the flow rate (see *Figure 22a*). First, equilibrium coverage fluctuations were monitored while an 1.7 mM solution of SDS was rinsed through the flow cell with a flow rate of $3 \cdot 10^{-4}$ m/s generated through gravitational flow. Then the flow was completely stopped by lifting the tubing and a timetrace was measured again. Based on these measurements the time constants τ were extracted by fitting the power spectra with a single Lorentzian (see *Figure 22b-c*). *Figure 22d* summarizes the respective values for the time constant and fluctuation amplitude. In both cases the value of τ was 0.09 s. So, the independence of the equilibrium coverage fluctuations of SDS from mass transport could be demonstrated.

As a remark: The following experiments were all conducted with a flow rate of $3 \cdot 10^{-4}$ m/s. To get a more defined (hydrophobic) surface, the rods were functionalized with 1-dodecanethiol (see *Chapter 5.3*).

5.4.1.2 Sensor Optimization

The first measurement parameters which have to be considered are the acquisition time and the total length of the measurement. The choice of these parameters is represented as follows within a power spectrum: the highest frequency corresponds to the acquisition time whereas the lowest frequency depends on the length of the timetrace. The power spectra were calculated with the Welch algorithm (see *Chapter 5.3*). Typically, a segment length of 2^{14} and an overlap of 99% were chosen. When the signal-to-noise ratio was amounted to be > 2, a timetrace of 10 min is sufficient to extract the rate constants. In cases of lower signal-to-noise ratios a timetrace of at least 20 min should be acquired. For the measurements of sodium dodecyl sulfate in PBS buffer the kinetic time constant τ was in the range of ~ 0.1 s. As a rule of thumb it should be measured by a factor of 10 lower than the characteristic time constant of the system under investigation. Especially within this project the usage of a much lower exposure time was necessary, so that the Lorentzian trend of the power spectra could be fitted accurately. Thus, an exposure time of 10 ms proved to be a suitable value.

For the purpose to determine the rate constants within one single experiment the right choice of the parameters which optimize the signal-to-noise ratio is worthwhile. In the following I demonstrate that the two prior parameters for this intension are the sensor size and the utilized concentration. Furthermore, the dependency of the time constant τ on the sensor size has to be investigated.

The signal-to-noise ratio strongly depends on the size of the sensor. The fluctuation amplitude is indirectly proportional to the surface area A:[126, 127]

$$\langle \delta\Theta^2 \rangle \sim A^{-1} \tag{5.23}$$

To demonstrate this, the respective signal-to-noise ratio of the equilibrium coverage fluctuations of SDS at a concentration of 1.7 mM was determined in 6 independent measurements (see *Figure 23, red*). The signal-to-noise ratio is hereby defined as quotient of the fluctuation amplitude of the measured signal, σ_s, and the fluctuation amplitude if the baseline, σ_b, measured in buffer conditions:

$$\frac{S}{N} = \frac{\sigma_s}{\sigma_b} \tag{5.24}$$

The baseline noise can almost exclusively be characterized as setup noise. It is largely independent of the surface area (see *Figure 23, blue*). A small influence of physical processes like density fluctuations of water molecules is nevertheless possible. The correspondent surface areas were calculated according to Henkel *et al.*.[138] The estimation of the dimensions of a single gold nanorod is possible on basis of the resonance wavelength and *FWHM* of its scattering spectrum. Henkel *et al.* used the boundary element method for the simulation of the scattering cross sections σ_{sca} to extract the resonance energy E_{res} and *FWHM* through fitting with a single Lorentzian. Furthermore, the bulk sensitivity was estimated by simulating an increase in the refractive index of the surrounding medium. Then, the value for the diameter and aspect ratio of one rod could be interpolated with a 5th order polynomial surface fit. In *Figure 23* it becomes apparent that despite of only minor differences in the surface area the signal-to-noise ratios range from 9.94 to 0.96 and can be approximated according to *formula 3.3*. All utilized sensors derived from the same batch. This is an impressive example how sensor minimization can drastically improve the resolution. As incubation with SDS drastically reduces the intensity of the plasmon spectra (for further discussion see *Chapter 5.4.3*) and consequently requires a conduction of the experiment under much higher exposure times experiments under utilization of even smaller sensors were not conducted. Further, it has to be kept in mind that further sensor minimization also increases the noise level of the baseline (also compare with *Figure 9*) which in turn again diminishes the signal-to-noise ratio.

For the calculation of the actual rate constants k_{on} and k_{off} (see next *Chapter 5.4.1.3*) the dependency of the constant τ on the size of the sensor has to be taken into account. *Figure 24* shows a significant increase in the value of τ for sensors with a surface area above $7 \cdot 10^3$ nm^2. Lüthgens *et al.*[126, 127] already considered this parameter for the Lorentzian function which describes the power spectrum calculated from observation of equilibrium coverage fluctuations of hard particles (i.e. proteins) (see *Chapter 5.2*). For such systems the available surface area is a function of the coverage and the available surface function (ASF) had to be considered. On the contrary, for the description of the adsorption kinetics of SDS

the ASF can be neglected at first sight under inclusion of the model conceptions that adsorption of SDS occurs via the alkyl tail and micelles do not adsorb as a whole (also compare with *Chapter 5.4.2*). However, the concept that one molecule only interacts with one single lattice site without further reciprocity with other molecules remains an ideal case. Because of the formation of surface micelles (see *Chapter 5.2.2*) molecules interact with each other and free lattice sites can potentially be blocked out. Furthermore, the surface of the sensor does not represent an ideal lattice but shows defects. Thus, also in case of SDS a coverage-dependent adsorption behavior is probably also existent and the model has to be extended under consideration of the ASF.

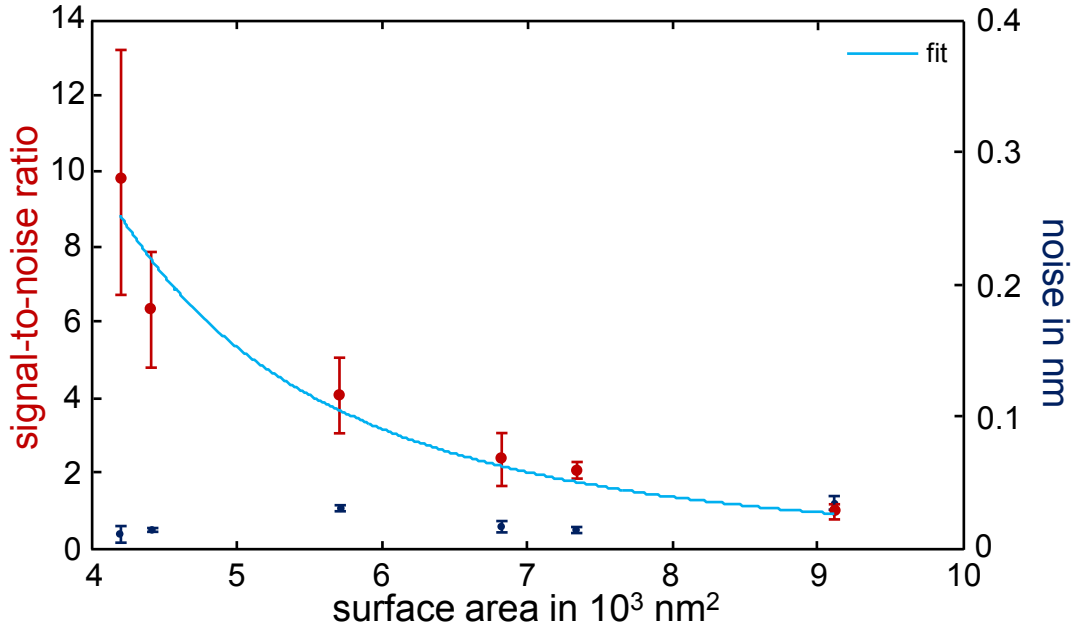

Figure 23. Dependency of the signal-to-noise ratio on the sensor size. The signal-to-noise ratio of the equilibrium coverage fluctuations of SDS depends on the surface area of the sensor (red). The trend can be approximated according to *formula 3.3* (light blue). For comparison, the noise levels of the corresponding baselines are shown respectively (dark blue). The utilized concentration of SDS was 1.7 mM in PBS solution for each case. All sensors were functionalized with 1-dodecanethiol.

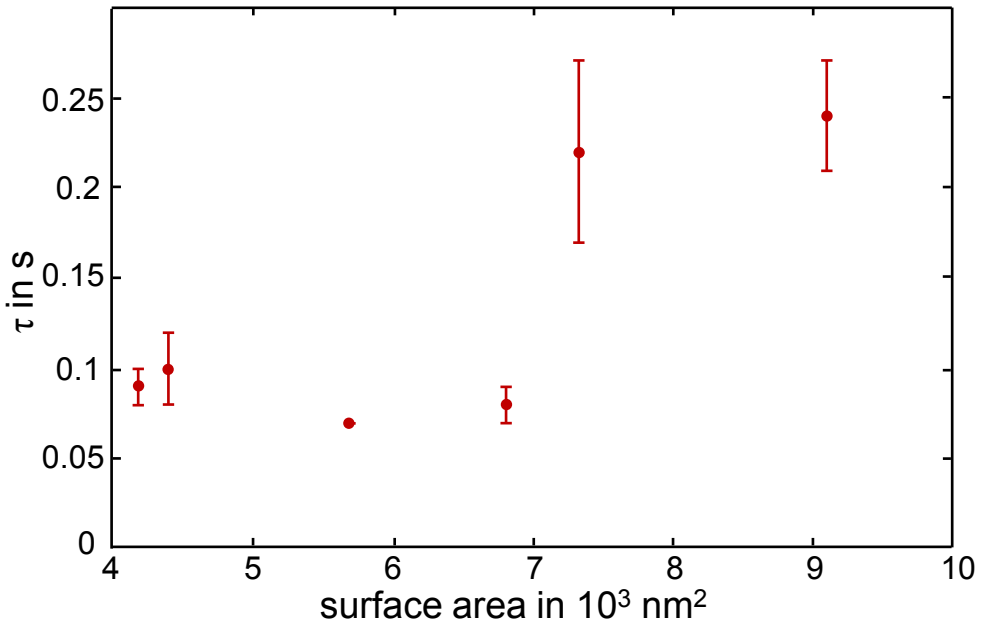

Figure 24. Dependency of the kinetic time constant τ on the sensor size. The values for τ were determined through approximation of the power spectrum with a single Lorentzian. The utilized concentration of SDS was 1.7 mM dissolved in PBS for all cases.

The signal-to-noise ratio can not only be optimized by the right choice of the sensor size but it also strongly depends on the utilized concentration. The fluctuation amplitude varies systematically with concentration. For the purpose to determine the rate constants within one single experiment the right choice of the utilized concentration is therefore worthwhile. In general, a higher concentration leads to a higher mean surface coverage of the sensor and thus to a higher exchange rate between bound and unbound molecules. To investigate the correlation between concentration and fluctuation amplitude for SDS in PBS the resonance wavelength of a single gold nanorod was measured while gradually increasing the concentration from 0 mM to 0.6 mM. After equilibrium was reached respectively the measurement was continued for 30 min before the next concentration was injected. *Figure 25a* shows correspondent timetrace sequences. *Figure 25b* shows that the averaged noise value of the baseline, 0.06 nm, does not increase significantly until a concentration of 0.3 mM is reached. Slight variation of the values below this "threshold" of 0.3 mM arises empirically from long term drifts due to setup instabilities (see *Chapter 3.2*).

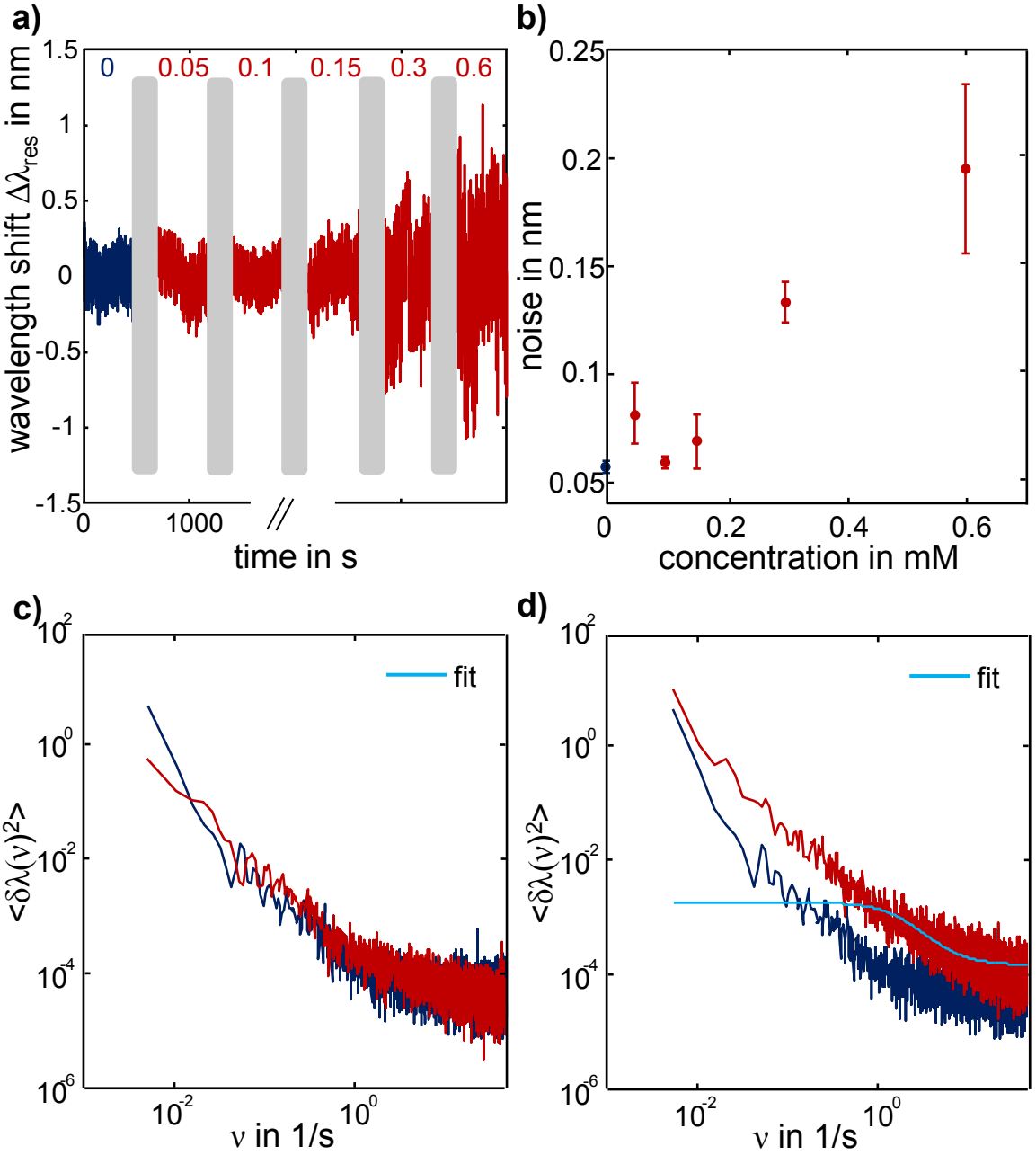

Figure 25. Concentration dependency of equilibrium coverage fluctuations of SDS. **a)** Timetrace sequences of the shift in the resonance wavelength of a single gold nanorod under variation of the SDS concentration. A gold nanord functionalized with 1-dodecanethiol was utilized as sensor. **b)** An increase in the concentration of SDS leads to an increase in the fluctuation amplitude. Only after a certain signal-to-noise ratio is overcome the corresponding power spectrum of the timetraces allows extracting the time constants. **c)** The shape of the power spectrum of the timetrace corresponding to 0.15 mM SDS solution does not differ from the baseline (dark blue). **d)** Increasing the concentration of SDS up to 0.3 mM increases the signal-to-noise ratio up to 1.2 and the power spectrum can be approximated with a Lorentzian function (light blue).

The power spectra which correspond to the concentrations ranging from 0.05 mM to 0.15 mM do not allow to extract the time constant τ as they do not differ from the baseline. This is exemplarily illustrated in *Figure 25c*. At a concentration of 0.3 mM the fluctuation amplitude increases up to 0.13 nm and the corresponding power spectrum can be described with a single Lorentzian (see *Figure 25d*). Consequently, a minimal signal-to-noise-ratio of 2.4 is necessary determine τ. Lüthgens *et al.*[126, 127] stated that for hard particle systems there is an optimum for the signal-to-noise ratio at intermediate coverage due to the dependency of the available surface area on coverage. Consequently, with increasing surface coverage the probability of a successful adsorption event and consequently the exchange rate decreases. To further discuss if and where there is an optimum in the fluctuation amplitude in case of SDS further understanding of the relationship between concentration, surface coverage (see *Chapter 5.4.1.3*), CMC (see *Chapter 5.4.2*) and the shift in the resonance wavelength of the sensor (see *Chapter 5.4.3*) is necessary before the optimal choice of the concentration can be determined.

5.4.1.3 Determination of the Rate Constants

In principle, one single measurement is sufficient to fully describe the kinetics of the system under investigation. In the previous chapter it was described how the kinetic time constant τ can be extracted by fitting the power spectrum with a single Lorentzian. The rate constants k_{on} and k_{off} can then be determined with the *formula 5.17-5.19*. There are generally two different strategies. First, the surface coverage can be calculated from the amplitude of the power spectrum (see *formula 5.16*) as $\langle \Theta \rangle$ corresponds to the ratio of bound molecules to the total number of molecules within the boundary layer $\langle N_A \rangle / N$. However, with so many unknown parameters the fit becomes unstable and shows high confidence intervals for both, $\langle N_A \rangle / N$ and τ and this method is not applicable. A more convenient approach is to use the information of the shift in the resonance wavelength of the sensor as benchmark for the coverage $\langle \Theta \rangle$. But until now, the effect that SDS causes a blue shift in the resonance wavelength is not fully understood (see *Chapter 5.4.3*). Alternatively – although it does not resemble the idea of determining k_{on} and k_{off} within one single experiment – the rate constants can be determined by varying the concentration of SDS and under utilization of *formula 5.17* and *5.18*. In an experiment presented in *Figure 26* the concentration was

varied in equidistant steps ranging from 1 mM to 0.25 mM and the time constants τ were calculated. As a function of the concentration the inverse τ^{-1} follows a linear trend where the slope corresponds to k_{on} and the offset to k_{off}. Consequently, k_{on} can be determined to (13.36±12.30) 1/mMs and k_{off} to (4.87±8.42) 1/s. It has to be kept in mind that the Lorentzian function does not involve the surface area of the sensor (compare with *Chapter 5.4.1.3*). Thus, these values are only an approximation. At least, the surface area of the sensor was determined to $4.4 \cdot 10^3$ nm^2 and thus belongs to the regime where an independence of τ from the surface area was observed (see *Figure 24*).

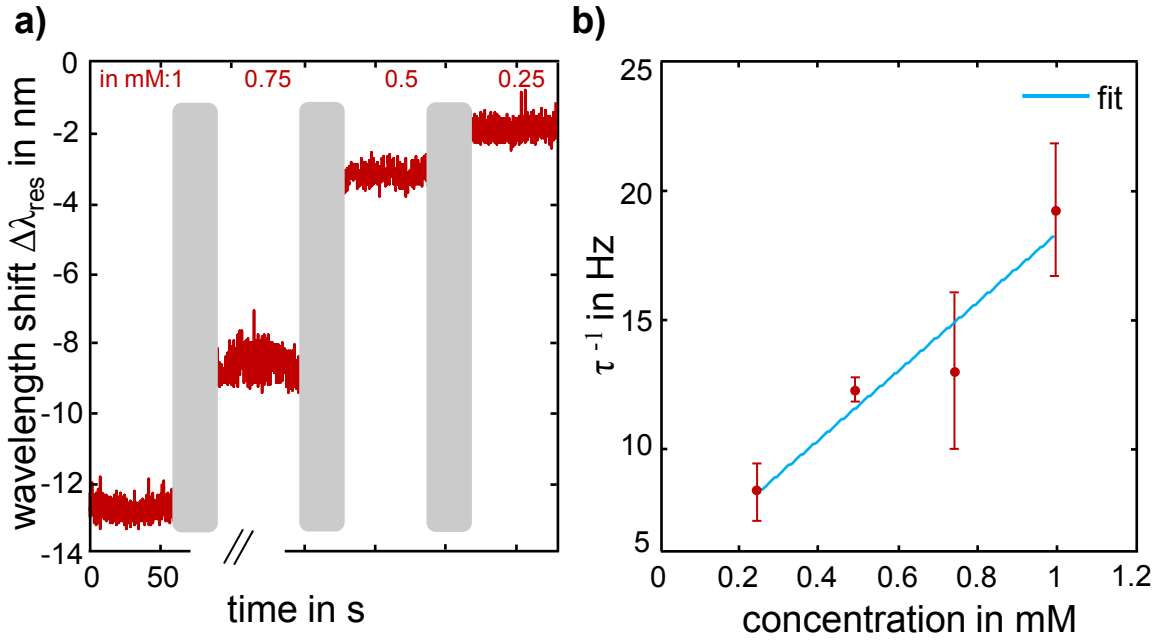

Figure 26. Determination of the rate constants k_{on} and k_{off}. **a)** Timetrace sequences of the shift in the resonance wavelength of a single gold nanorod under variation of the SDS concentration in the surrounding buffer medium (PBS). The utilized nanorod was functionalized with 1-dodecanethiol. **b)** The kinetic time constant τ varies with concentration. As a function of the concentration the inverse τ^{-1} follows a linear trend (light blue).

On the basis of the estimated k_{on}-and k_{off}-values we can calculate the number of adsorbed molecules on the surface. This is conducted as follows: Through the knowledge of k_{on} and k_{off} the surface coverage Θ can be determined via *formula 5.19* (see *Figure 27, blue*). To calculate the number of adsorbed molecules N (see *formula 5.25*) the surface area of the sensor A_{surf} was determined according to Henkel *et al.*[138] and the area per molecule $A_{molecule}$ was taken from Turner *et al.*.[106] They determined a value of 0.42 nm^2.

$$N = \frac{A_{molecule}}{\Theta \cdot A_{surf}} \tag{5.25}$$

For a mean coverage of 58% the mean number of molecules bound to the sensor surface can therefore be determined to approximately 6000 (see *Figure 27*, *red*). The shift per molecule is in average around 0.001 nm. However, due to the high error limits of the values for k_{on} and k_{off} a reasonable consideration of the error limits for the coverage and the number of bound molecules is not possible and these values represent therefore only a rough estimation.

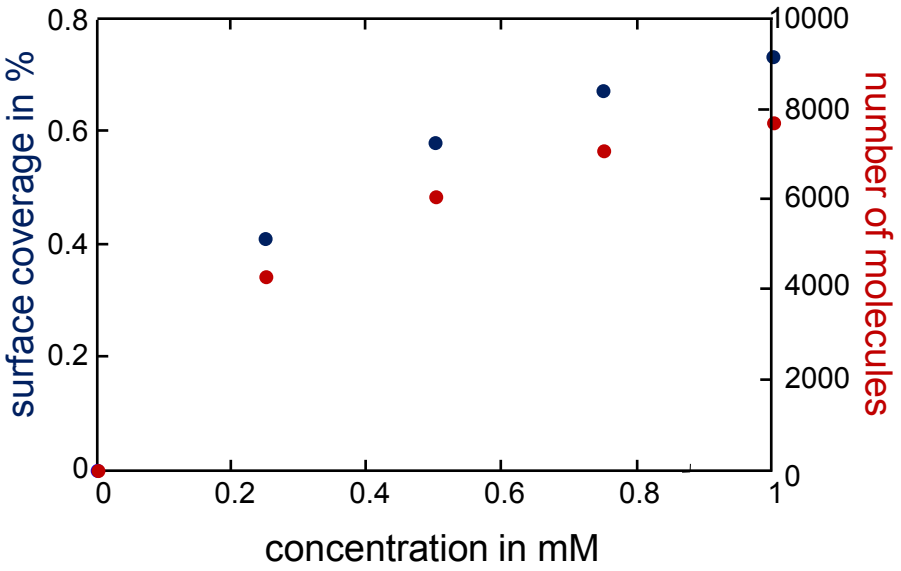

Figure 27. Surface coverage and number of bound molecules in dependency of the concentration. The surface coverage (blue) and thus also the number of bound molecules (red) increase non-linear. The data corresponds to the measurement presented in *Figure 26*.

In *Chapter 5.4.1.2* it was demonstrated that there is a lower limit in the concentration/ surface coverage for the observation of equilibrium coverage fluctuations. Janshoff *et al.*[126] stated that there is also an upper limit where the exchange rate between surface and solution reaches its maximum. *Figure 28* shows the fluctuation amplitudes in dependence of the surface coverage. The noise reaches its maximum at an estimated coverage of 67% which is introduced by a concentration of 0.75 mM. However -as mentioned before- the relationship between shift in the resonance wavelength, surface coverage, concentration and

sensor size has first to be further investigated before the upper limit can be further discussed.

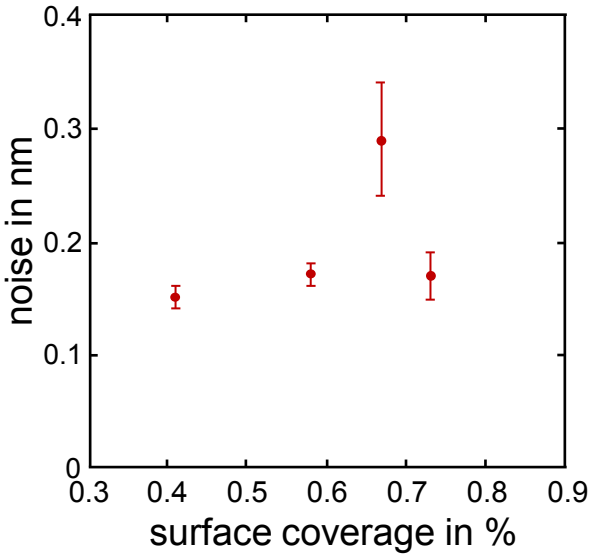

Figure 28. Dependency of noise on surface coverage. The data corresponds to the measurement shown in *Figure 26*.

5.4.2 Adsorption Behavior of Sodium Dodecyl Sulfate

The adsorption behavior of surfactants is strongly dependent on the surface characteristics of the sensor. To demonstrate this, the nanorods were functionalized with two different kinds of thiols. First, cysteamine was introduced which forms a hydrophilic, positively charged self-assembled monolayer (SAM) on the surface of the rod (see *Figure 29c*). For comparison, the sensor surface was functionalized with 1-dodecanethiol as in the already described experiments to get a hydrophobic SAM (see *Figure 30c*). This is in accordance to Levchenko *et al.*[105] who also studied adsorption behavior of SDS on hydrophilic and hydrophobic functionalized surfaces via Surface Plasmon Resonance (SPR). In both cases adsorption was observed by introducing 1.7 mM SDS in PBS and desorption was initiated by rinsing with pure buffer solution (see *Figure 29a* and *Figure 30a*). In case of the hydrophobic functionalized sensor (see *Figure 30a*) the adsorption occurs within seconds due to the high affinity of SDS for hydrophobic SAMs and the corresponding power spectrum can be fitted with a Lorentzian function (see *Figure 30b*). On the contrary, in the case of the

hydrophilic surface adsorption shows a biphasic behavior: an original faster rate is followed by a slower adsorption rate until equilibrium is finally reached after approximately 1450 s (see *Figure 29a*). Levchenko *et al.*[105] confirmed a higher affinity of SDS for hydrophobic than for hydrophilic surfaces where electrostatic interaction prevails. Within the first 100 s after rinsing with PBS buffer to introduce desorption, already approximately 60% of SDS desorbed from the sensor surface. In comparison, only 45% of SDS desorbed within the same period in case of the hydrophobic functionalized surface. For hydrophobic surfaces the desorption kinetics are slower than the adsorption kinetics as intermolecular van der Waals interaction stabilize adsorption.[105] The corresponding power spectrum of the hydrophilic surface does not follow a Lorentzian function (see *Figure 29b*). The reason therefore is probably that the fluctuations occur at a slower timescale in comparison to the case when hydrophobic surfaces are present so that the kinetic time constant τ is not represented within the measured frequency regime. Instead, a longer measurement time would be necessary. Levchenko *et al.*[105] suggest two different models for the adsorption behavior of SDS. On hydrophobic surfaces micelles do not adsorb but only provide monomer surfactants for the bulk (see *Figure 30c*). On hydrophilic surfaces on the contrary micelle adsorption prevails over single molecule adsorption (see *Figure 29c*).

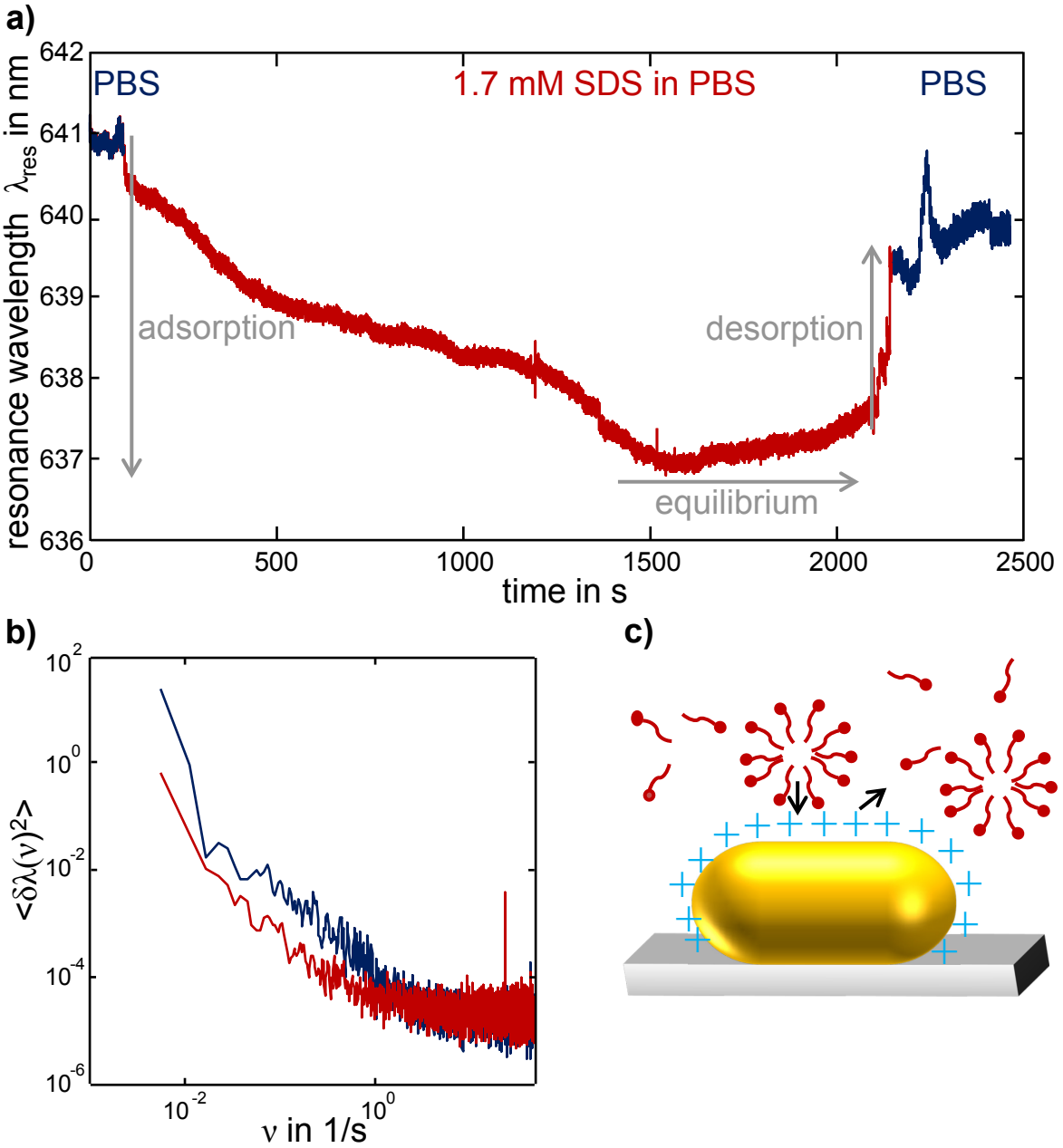

Figure 29. Adsorption of SDS on hydrophilic surfaces. **a)** Timetrace of the resonance wavelength of a single gold nanorod functionalized with cysteamine. After rinsing with PBS buffer (blue) a buffer solution containing 1.7 mM SDS was introduced (red). A blue shift in the resonance wavelength indicates the adsorption of SDS molecules on the sensor surface. Desorption was introduced by rinsing with PBS again. **b)** The power spectrum of the timetrace sequence in the equilibrium state (red) does not follow a Lorentzian function in the measured frequency regime. For comparison, the power spectrum of the baseline in PBS buffer is displayed (blue). **c)** Schematic representation of the adsorption of SDS on the positively charged surface. Above the CMC micelle adsorption prevails over single molecule adsorption.[105]

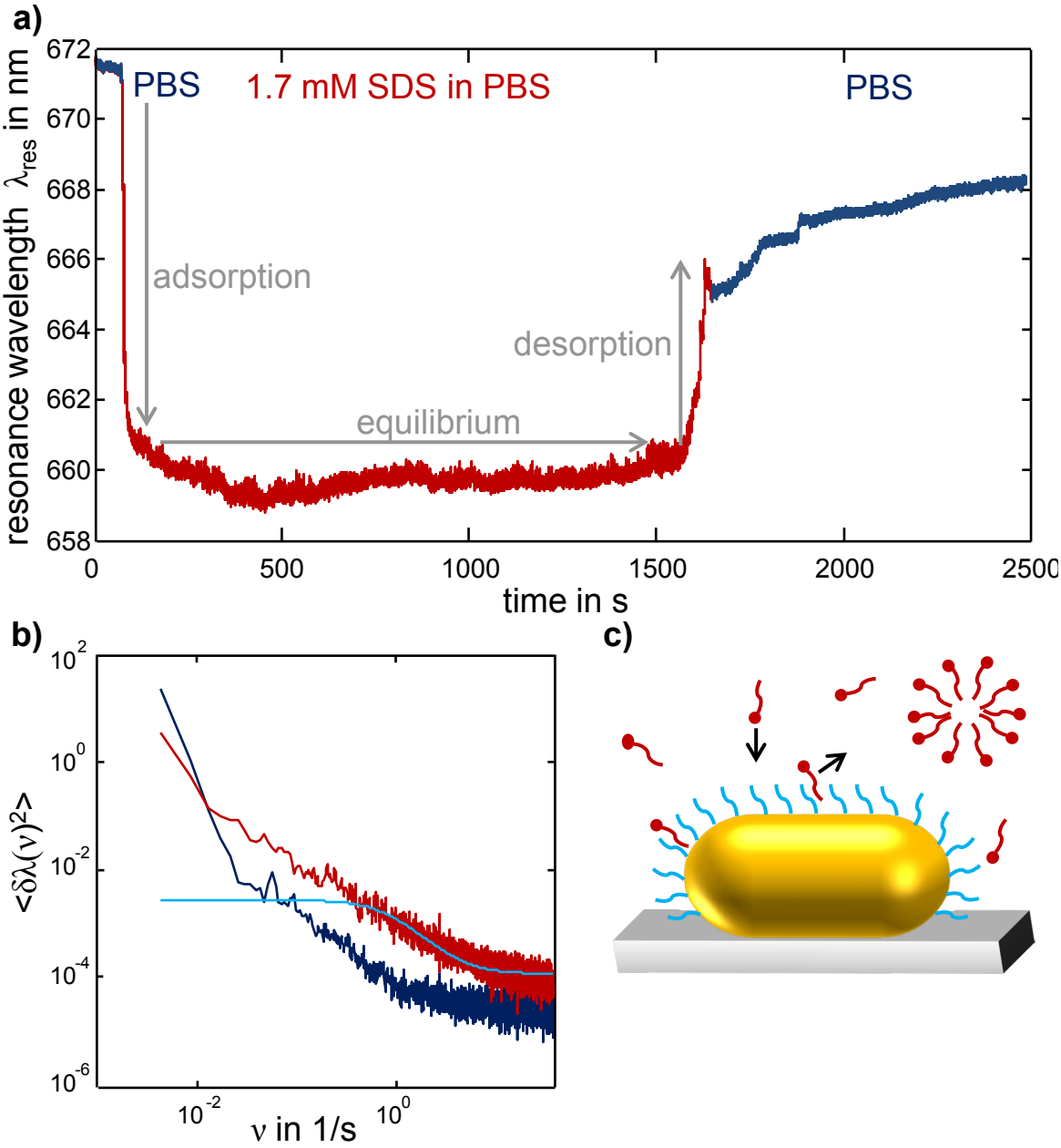

Figure 30. Adsorption of SDS on hydrophobic surfaces. **a)** Timetrace of the resonance wavelength of a single gold nanorod functionalized with 1-dodecanethiol. After rinsing with PBS buffer (dark blue) a buffer solution containing 1.7 mM SDS was introduced (red). A blue shift in the resonance wavelength indicates the adsorption of SDS molecules on the surface of the sensor. Equilibrium was reached within seconds. Desorption was introduced by rinsing with PBS again. **b)** The power spectrum of the timetrace sequence in the equilibrium state (red) is shown. It can be described by a single Lorentzian (light blue). For comparison, the power spectrum of the baseline in PBS buffer is also displayed (dark blue). **c)** Schematic representation of the adsorption of SDS on the hydrophobic surface of the sensor. Above the CMC single molecule adsorption prevails over micelle adsorption.[105]

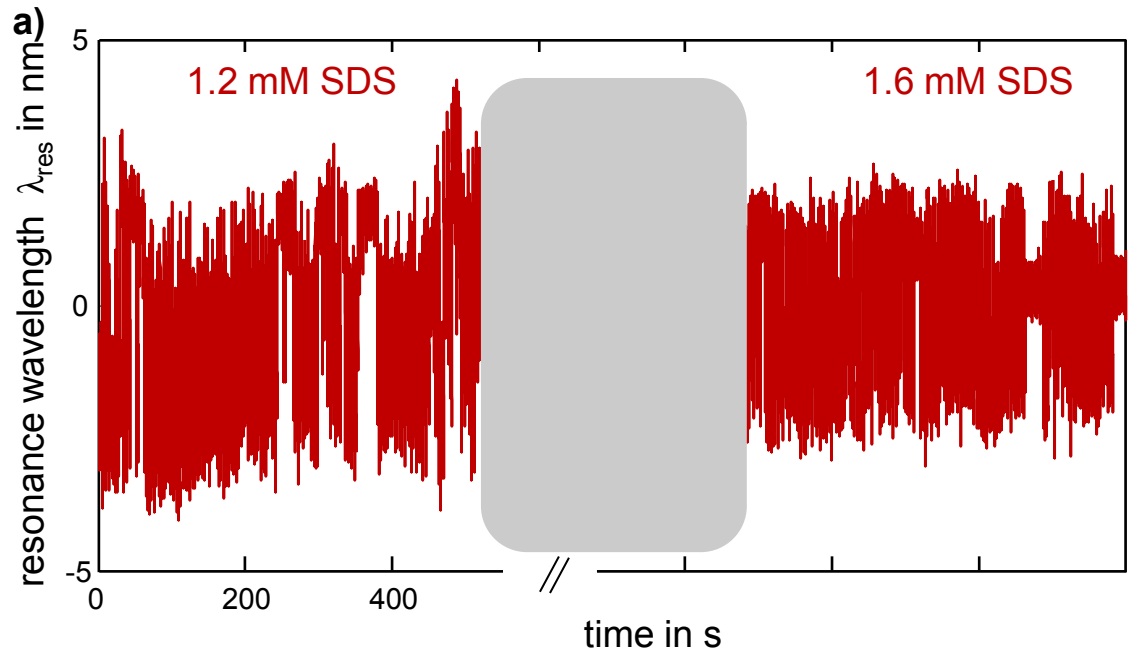

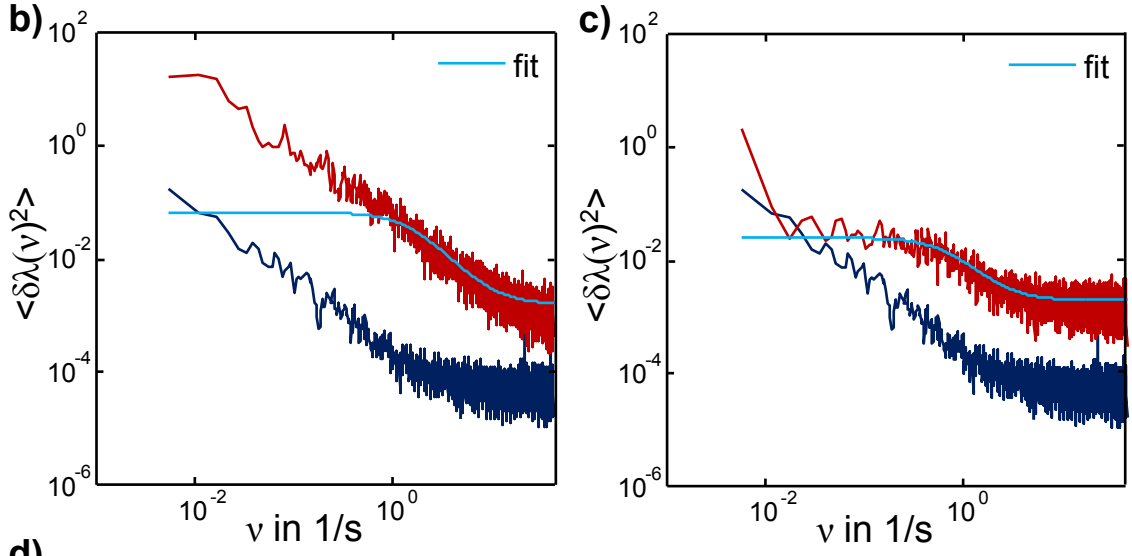

d)

c_1 in mM	c_2 in mM	σ_1 in nm	σ_2 in nm	τ_1 in s	τ_2 in s
1.2	1.6	0.63±0.15	0.32±0.05	0.08±0.02	0.19±0.02

Figure 31. Adsorption behavior of SDS above the CMC. **a)** Timetrace sequences of the resonance wavelength of a single gold nanorod functionalized with 1-dodecanethiol under variation of the SDS concentration in the surrounding buffer medium (PBS). In both cases, the critical micelle concentration is overcome (see *appendix F*, *Figure 47*). **b)-c)** The corresponding power spectra of the timetrace sequences (red) can be described by a single Lorentzian (light blue). For comparison, the power spectra of the baseline in PBS buffer are shown (dark blue). **d)** Overview of the calculated noise values σ and kinetic time constants τ of the presented measurement.

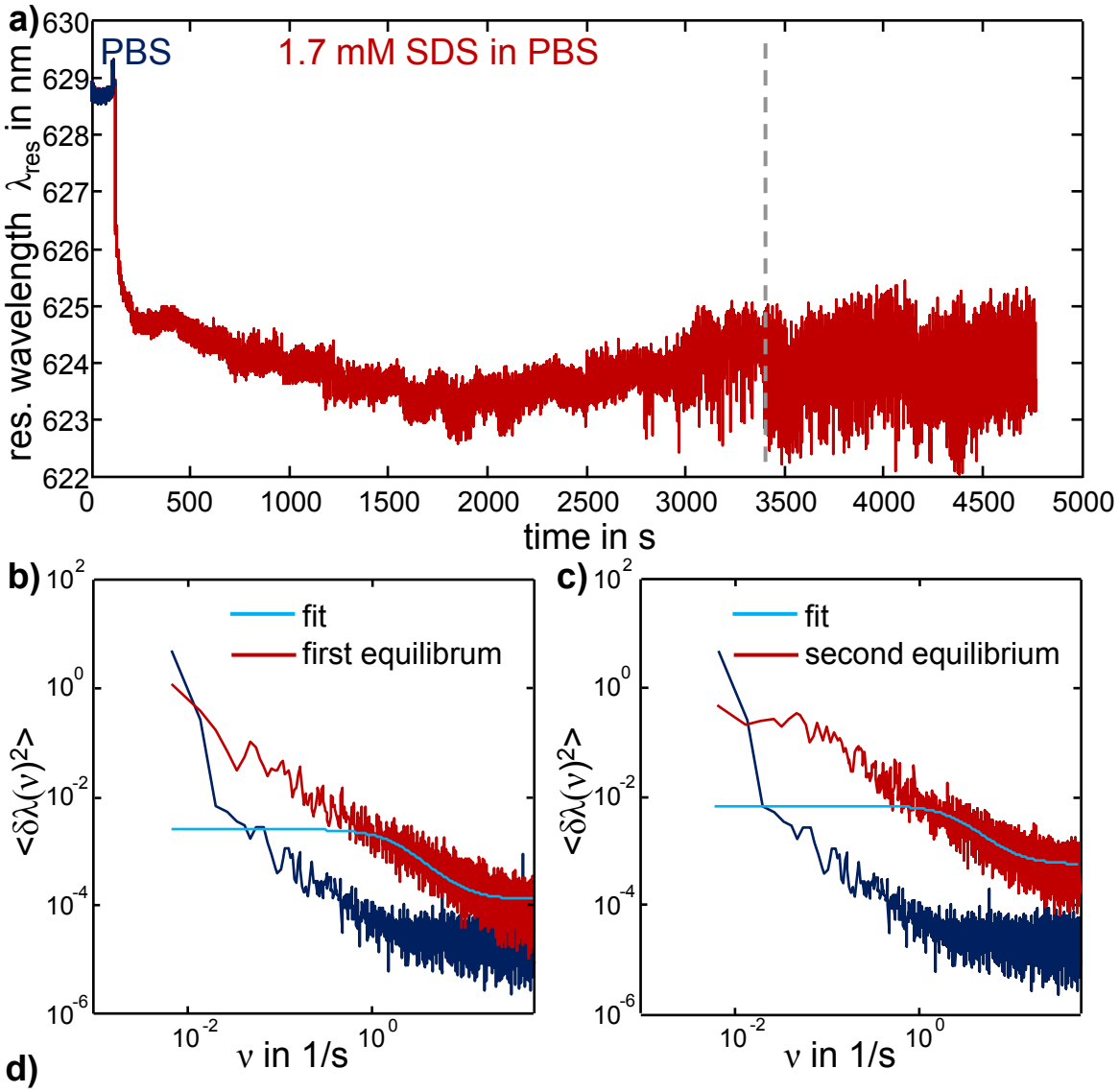

d)

measurement	A_{surf} in 10^3 nm^3	σ_1 in nm	σ_2 in nm	τ_1 in s	τ_2 in s	Δt in s
1 (shown)	6.82	0.10±0.01	0.28±0.04	0.08±0.01	0.05±0.00	3330
2	4.41	0.24±0.05	0.63±0.17	0.10±0.02	0.06±0.01	650

Figure 32. Time dependency of SDS adsorption. **a)**Timetrace of the resonance wavelength of a single gold nanorod functionalized with 1-dodecanethiol. It was first rinsed with PBS buffer (dark blue) and then with a buffer solution containing 1.7 mM SDS. Shifts in the resonance wavelength were monitored for approximately 4500 s. A blue shift in the resonance wavelength indicates the adsorption of SDS molecules on the surface. Equilibrium was reached within seconds. After approximately 3330 s a further increase in the fluctuation amplitude can be observed. **b)-c)** The corresponding power spectra of the timetrace sequences (red) can be described by a single Lorentzian (light blue). For comparison, the power spectra of the baseline in PBS buffer are shown (dark blue). **d)** Overview of the calculated noise values σ and kinetic time constants τ of the here presented measurement *(1)* and another measurement (*2, see appendix F, Figure 50*) using a sensor with a smaller surface area A_{surf}.

Furthermore, the adsorption behavior of SDS above the critical micelle concentration (CMC) on hydrophobic surfaces was investigated. Therefore, the resonance wavelength of a single gold nanorod functionalized with 1-dodecanethiol was monitored while first rinsing with a 1.2 mM solution of SDS and then changing to a 1.6 mM solution (see *Figure 31a*). Both concentrations are above the CMC (compare with *appendix F, Figure 47*). For both timetrace sequences the power spectra were calculated, fitted with a Lorentzian function and the kinetic time constants τ were calculated (see *Figure 31b* and *c*). *Figure 31d* compares the extracted time constants as well as the fluctuation amplitudes. With increasing concentration the value for τ increases and the fluctuation amplitude decreases. This effect is known in literature. Over time SDS hydrolyzes and forms dodecanol.[106] Due to solubilization of dodecanol within bulk micelles the total amount of surfactants sinks above the CMC.[106, 139, 140] Experimental results by Levchenko *et al.*[105] confirm these results. Alternatively, Montgomery *et al.*[141] named structural changes of the surface micelle formation as reason.

Finally, the equilibrium coverage fluctuations of SDS were followed for long time to investigate the time dependency of the system. *Figure 32a* shows the adsorption curve of a 1.7 mM solution of SDS on a single gold nanorod. The blue shift indicates adsorption and equilibrium was reached within seconds. The power spectrum calculated from the timetrace sequence directly after adsorption can be described with a single Lorentzian and a value of 0.08 s for τ can be determined (see *Figure 32b*). After approximately 3330 s the fluctuation amplitude increases from 0.10 nm to 0.28 nm and τ decreases to 0.05 s (also compare with *Figure 32c*). A complete overview over the calculated values is given in *Figure 32d.* The same experiment was repeated with a smaller dimensioned sensor (compare with *Figure 32d, measurement 2,* full data can be found in *appendix F, Figure 50*). Thereby, a decrease of τ in combination with an increase of the fluctuation amplitude was observed already after 650 s. The two different time constants allow a classification into an initial slow and into a second faster adsorption dynamic. The reason for this phenomenon lies probably in the reorganization of the surfactants on the sensor surface. Surfactants form micellar structures on solid surfaces. This effect was first investigated via Atomic Force Microscopy by Manne *et al.*.[111] The surface micelle formation of SDS was investigated on

graphite as model hydrophobic surface.[142, 143] Periodic, hemicylindric structures were monitored. Thereby, the critical surface aggregation concentration (*csac*) where SDS starts to form structures was determined to be at about one fourth of the CMC.[142] By increasing the concentration of SDS or by increasing the concentration of sodium chloride in solution under constant concentration of SDS the distance between neighboring aggregates decreases.[142, 143] Additionally, the presence of 1-dodecanol leads to changes in the shape in form of swollen hemicylinders and flat layers above the CMC.[144] Beyond, surface micelle structures can change over time. For example, Ducker *et al.*[145] monitored the formation from rods to uniform sheets of CTAB in water on a hydrophilic mica surface. There consequently are two thinkable scenarios for the explanation of the time dependency of equilibrium coverage fluctuations of SDS. The first possibility is that the whole surface micelle formation does not occur instantaneously. Consequently, subsequent adsorption and reorganization is a kinetically slower process than when the surface micelles have already fully formed. Second, a metastable surface micelle formation forms instantaneously which then transforms into a more stable configuration at the minute timescale. Then, this second configuration shows a higher micelle stability but less affinity to the surface which results into an higher surfactant exchange rate at the solid-liquid interface and the time constant τ increases.

5.4.3 Explanation for the Blue Shift

When SDS is adsorbed on the surface of a plasmonic nanorod the plasmonic spectrum changes as follows: The resonance wavelength shifts to the blue. Thereby, the height of the shift increases with increasing aspect ratio of the particle and can amount up to 15 nm. The intensity always decreases around 30-60% of the original value. The full width at half maximum stays approximately constant. *Table 3* exemplarily demonstrates this phenomenon for the measurement presented in *Figure 30*.

Table 3. Influence of SDS incubation on plasmonic spectra**.** Overview of the resonance wavelength λ_{res}, the full width at half maximum *FWHM* and intensity *I* before (1) and after (2) SDS in PBS buffer medium is introduced to a gold nanorod.

$\lambda_{res}(1)$ in nm	$\lambda_{res}(2)$ in nm	*FWHM(1)* in eV	*FWHM(2)* in eV	I(1) in arb.u.	I(2) in arb.u.
671.5	659.7	0.143	0.159	22800	15700

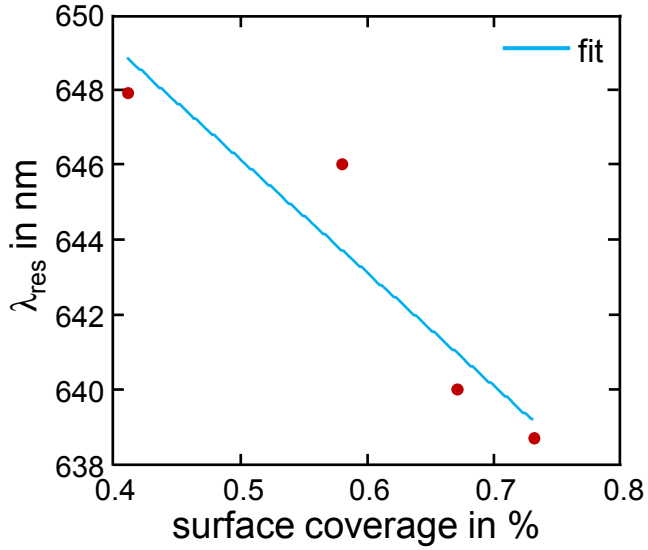

Figure 33. Shift dependency of the coverage. The absolute value of the shift in the resonance wavelength increases with increasing surface coverage. The data belongs to the measurement presented in *Figure 26*. The values for the surface coverage were calculated in *Chapter 5.4.1.3*. A linear fit is shown (light blue).

Further, the absolute value of the shift in the resonance wavelength increases with increasing surface coverage (see *Figure 33*).

There are different possibilities for the explanation of the blue shift. First, the blue shift can be initiated by refractive index changes and as second reason charge carrier effects have to be considered. A local change in the refractive index can in principle be caused as SDS shows a higher refractive index than water. The value was determined to 1.461.[146] Consequently, a red shift in the resonance wavelength of the sensor is expected. This holds true if SDS in dissolved in pure water (see *Figure 34a*). However, if SDS is dissolved in phosphate buffered saline a blue shift is monitored (see *Figure 34b*). Additionally, different kinds and combinations of salt where tested. The blue shift arose in all cases (further timetraces see *appendix F*, *Figure 49*). Thus, for the observation of a blue shift the presence of ions is necessary but it is not dependent on specific kinds. Furthermore, the reversible replacement of a negatively charged SDS layer on the sensor surface by a positively charged CTAB layer was investigated (see *Figure 34c*). It is interesting to see that the introduction of CTAB leads to a red shift although it shows a smaller refractive index than SDS (n_D =1,435[147]) and a blue shift would be expected.

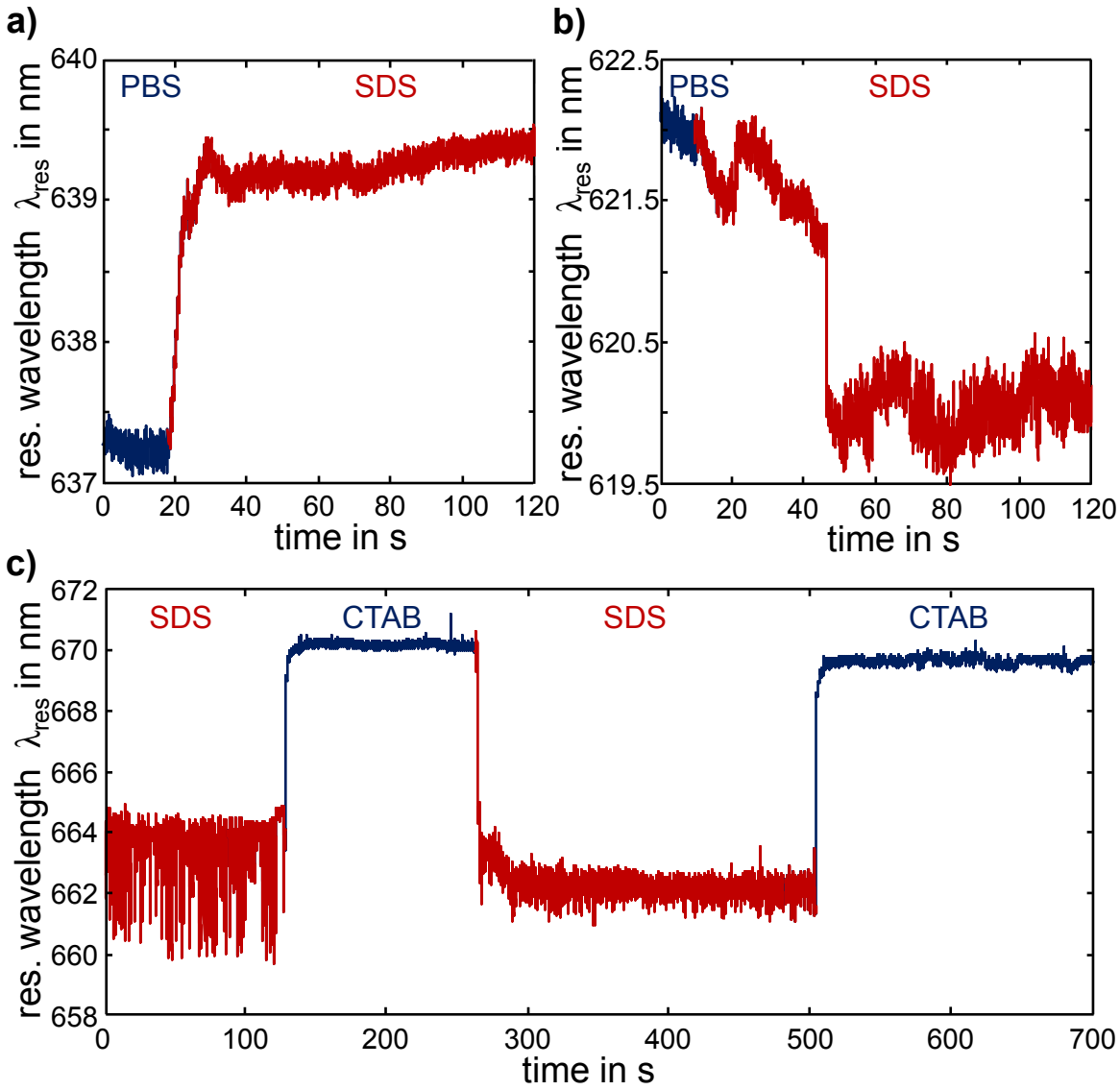

Figure 34. Shifts in the resonance wavelength when SDS is introduced. In all cases a concentration of 1.7 mM and CTAB rods without further modification were applied. **a)** Resonance wavelength of a single gold nanorod shifts to the red when SDS is dissolved in water. **b)** Resonance wavelength shifts to the blue in phosphate buffered saline medium when SDS was introduced. **c)** SDS and CTAB, respectively dissolved in PBS, were injected by turns. CTAB leads to a red shift in the resonance wavelength.

The blue shift can in principle also be caused by a desorption effect although no such thing has been reported in literature.[105] SDS would then remove the functionalization of the senor. However, the blue shift was also observed on blank rods where the prior removing of the CTAB by incubation with sodium thiosulfate was monitored (see *Chapter 5.4.1.1*). Besides, different adsorption behavior was detected by different kinds of surface modification (see *Chapter 5.4.2*). 1-dodecanethiol has almost the same refractive index as SDS (n_D

=1,459[148]) due to the quite similar chemical structure. Thus, no shift is expected by a replacement of 1-dodecanethiol with SDS. Regarding the equilibrium coverage fluctuations in itself timetraces with fluctuation amplitudes up to 0.9 nm were acquired (see *Chapter 5.4.1.1*). It is unlikely that this extremely high fluctuation amplitude caused by minor variations in the surface coverage arises from local changes in the refractive index especially as the thickness of the SDS layer is expected to be in the range of 1nm and less.[106] Considering all these arguments, changes in the refractive index are a less probable explanation for the effect that SDS causes a blue shift.

Therefore, charge carrier effects introduced by the presence of salts have to be taken into account. Either, it is charging which means that an electron transfer from a SDS molecule to the gold nanorod occurs and the electron density in the rod increases. That electron transfer can occur through a non-conjugated, self-assembled passivating hydrocarbon film was already demonstrated by K. A. Bunding Lee.[149] He functionalized gold electrodes with hydrocarbons consisting of an electro active end and a thiol group which binds covalently to gold. Electron transfer was measured via Cyclic Voltammetry with a hydrocarbon chain consisting of up to 10 CH_2-groups and even if disorganization of the layer was existent.

Another explanation related with charge carrier effects is an induction phenomenon as explanation for the blue shift due to the point charge of SDS. Then, the electron density within the sensor would increase due to the scenario that the negatively charged SDS layer around the sensor compresses the electron density (see *Figure 35*). A first calculation on this can easily be conducted: The negatively charged SDS layer has the following surface charge density σ:

$$\sigma = \frac{e}{A_{molecule}} \tag{5.26}$$

with the elementary charge e. Then, the layer thickness d of the positively charged image charge can be estimated as follows:

$$d = \frac{\sigma}{\rho_0} \tag{5.27}$$

with $\rho_0 = 59 e/nm^3$.

ρ_0 is the initial electron density of gold. This results into a value for d of 0.04 nm.

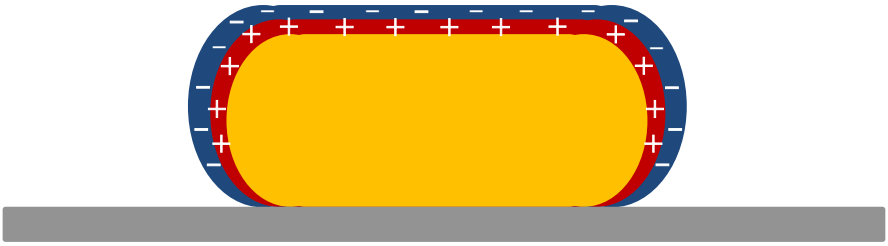

Figure 35. Schematic representation of the induction phenomenon. A negatively charged layer around a gold nanorod (blue) leads to a positive image charge (red) and electron density within the rods increases.

A less probable explanation for the blue shift would be the oxidation of the gold rod. Then, gold ions would change over to the surrounding solution and SDS molecules would become a radical. The blue shift would be caused by shape modification of the rod as a smaller particle shows a smaller resonance wavelength.

Within this thesis the question of why SDS causes a blue shift in the resonance wavelength of a gold nanorod could not be completely solved. Further experiments to clarify this issue can be conducted with plasmonic particles as well as through electrochemistry. Experiments on basis of plasmonic nanoparticles have to be conducted on the single particle level were the sensors are immobilized on a glass substrate and not in solution as the presence of salts leads to aggregation of the particles. The possibility of charging can be surveyed by the utilization of radicals. Thereby, if rods would have been negatively loaded an introduction of radicals would annihilate the blue shift. However, radicals have to be found which do not bind or interact with the sensor itself. Path breaking also appears to follow electrochemical experiments according to K. A. Bunding Lee.[149] To test the theory of induction theoretical simulations seem to be most suitable.

5.5 Conclusions and Outlook

Within this project, it was for the first time experimentally demonstrated how to describe adsorption kinetics through observation of equilibrium coverage fluctuations. Thereby, sodium dodecyl sulfate dissolved in phosphate buffered saline was introduced as system under investigation. Temporal fluctuations of the resonance wavelength of a single gold nanorod were evaluated via Fourier analysis and the kinetic time constant τ could be determined. Different strategies for the calculation of the rate constants k_{on} and k_{off} were discussed and applied. Furthermore, it was demonstrated how the signal-to-noise ratio can be improved by the right choice of the utilized concentration as well as of the size of the sensor. Finally, the adsorption behavior of SDS was investigated. Different adsorption behavior for different kinds of surface modification was shown. Above the critical micelle concentration a decrease in adsorption kinetics was observed. When following equilibrium coverage fluctuations for longer time a second, faster adsorption dynamic was monitored. At last, several possible explanations for the effect, that SDS causes a blue shift in the resonance wavelength of a nanorod were discussed.

Lüthgens *et al.*[126, 127] pointed out 5 major advantages for the determination of the rates constants through observation of equilibrium coverage fluctuations in comparison to conventional methods (see *Chapter 5.2*). In the following I will discuss each of these points separately under inclusion of my experimental data. The first argument was that equilibrium coverage fluctuations are independent of mass transfer so that such complications do not have to be considered. This was confirmed by my experiments. However, in meantime Jokic *et al.*[135, 136] demonstrated in 2012 the influence of mass transport on theoretical basis and extended the Janshoff-model. So either the system of SDS falls under the by Jokic classified category where the diffusion timescale is shorter than the convection timescale and mass transport does thus not have to be considered or the extension of the model is wrong. Consequently, when the approach to quantify adsorption kinetics through observation of equilibrium coverage fluctuations will be extended to protein systems which show due to their bigger size a much slower diffusion control experiments on mass transport have to be conducted. As second argument falsified results due to drifts in the measuring signal in common adsorption experiments were mentioned. In fact, within my experiments

long term drifts in the resonance wavelength were also present and were probably caused by thermal instabilities of the Plasmon Fluctuation Setup. However, these drifts were not represented in the corresponding power spectra so that no detrending of the timetraces was necessary. Third, in conventional experiments the standard Langmuir equation could only describe the adsorption isotherms inadequate and thus an exact determination of the rate constants failed. Consequently, in case of SDS Levchenko *et al.*[105] could only describe the adsorption behavior via half-times and initial rates but were not able to determine exact values for the rate constants. In my experiments, the power spectra were described with a standard Lorentzian without further adaption to system specific properties and kinetic time constants could be calculated. However, the power spectra also showed instrumental non-linear noise in the low frequency regime so that a more accurate fitting is developable. Ideally, an exact mathematical description for the instrumental noise can be found and included into the fitting function. Forth, some systems show a two-step kinetic where the second step above the so called jamming limit is not reached after a for experiments appropriate time. On the contrary, with the detection scheme of equilibrium coverage fluctuations the kinetic time constants can be determined within one single experiment at intermediate coverage. Fifth, with common techniques quite a number of adsorption isotherms have to be acquired to calculate the rate constants. This is time consuming and falsifies the extracted values. Now, the kinetics can be fully described within one single experiment. The extracted values of τ were < 1 s. The sample rate used for these experiments was around a factor of 10 higher than the τ values. This was found to be necessary since for the approximation of the power spectra with a single Lorentzian many data points in the high frequency regime are necessary. When the signal-to-noise ratio was at least 2 a timetrace of around 10 min was sufficient.

The validation of this new detection scheme with regard to its accuracy for the determination of the actual rate constants k_{on} and k_{off} remains challenging. First, the initial adsorption isotherms couldn't be approximated accurately with the Langmuir equation (also compare with Levchenko *et al.*[105]). Consequently, the values determined via equilibrium coverage fluctuations cannot be compared to a control experiment conducted with the conventional method. Second, as the effect why SDS causes a blue shift in the resonance wavelength is so

far not completely understood the relationship between shift and surface coverage is not given. For validation further investigations which lead to an understanding of the blue shift as well as a further development of the mathematical description of the equilibrium coverage fluctuations seems path breaking. The so far applied single Lorentzian has to be extended under inclusion of system-specific properties, probably also under consideration of coverage-dependent adsorption behavior and inclusion of an available surface function.

The big question remains for how many systems the approach to extract the rate constants through observation of equilibrium coverage fluctuations is applicable. One major limitation is that a reversibility of the system is essential. The system under investigation should show a reversible adsorption behavior to a high extent. This was the case with SDS.[105] However, especially in regards of biosensors there would be many limitations since protein interactions at the solid-liquid interface are often described as irreversible. One protein system which shows at least partly reversible adsorption on a lipid bilayer membrane is annexin A1.[150-154] Further, reversible protein-protein interactions can be studied when one partner is fixed on the surface and the other one is free in solution. One example for this is the system "polycystin-2 and polycystin-1".[155] Another limitation is the timescale at which these adsorption-desorption processes occur. Kastl. *et al.*[150] already published k_{on}- and k_{off}-values for the system "annexin A1 + membrane". On basis of these values the kinetic time constant τ yields to the range of 10^{-3} Hz- depending on the concentration. Consequently, this requires on the one hand a quite long measurement time and on the other hand, equilibrium coverage fluctuations are then not so easy to separate from long term drifts of the measuring signal due to setup instabilities.

In case of sodium dodecyl sulfate the equilibrium coverage fluctuations can be classified into an initial slow and into a second faster adsorption dynamic. It arises probably from reorganization processes on the surface. This phenomenon has so far not been experimentally accessible in this manner and gives now further insight into the adsorption process of SDS on the molecular level. Future experiments including a combined analysis of Plasmon Spectroscopy and liquid Atomic Force Microscopy would be interesting to further investigate surface micelle formation and how the shape of surface micelles influences the

adsorption kinetics. An additional topic which was not further investigated within this thesis is the roll of present salts on adsorption kinetics.

The effect why sodium dodecyl sulfate causes a blue shift in the resonance wavelength of a gold nanorod was not solved within this thesis - however the basis to enter a new regime of plasmon sensing is set.

Chapter 6

If there is magic on this planet, it is contained in water.

-- Loren Eiseley

6 Diffusion Kinetics of Gold Nanospheres

6.1 Introduction

Molecular transport within living cells as well as mass transfer through membranes is a prior condition for the existence of animate being. Consequently, many natural scientific disciplines ask for techniques to measure diffusion coefficients and concentrations of molecules in different environments.[156] One technique to study diffusing molecules is the so called Fluorescence Correlation Spectroscopy (FCS) (see *Figure 36a*) which was firstly published by Elson and Madge in 1974[157] and has become a well-established technique.[158] Fluctuations of dye labeled molecules within a quite small detection volume are measured and intensity fluctuations of the fluorescent labeled molecules are recorded over time. For analysis the autocorrelation is calculated which is defined as follows:

$$G(\tau) = \frac{1 + \langle \delta F(t) \delta F(t+1) \rangle}{\langle F(t) \rangle^2} \tag{6.1}$$

with $\delta F(t) = F(t) - \langle F(t) \rangle$

Thereby, *F(t)* is the detected fluorescence intensity. In a standard FCS setup the autocorrelation can be expressed by

$$G(\tau) = \frac{1}{\langle N \rangle} \cdot \frac{1}{1 + \frac{\tau}{\tau_D}} \cdot \frac{1}{\sqrt{1 + \frac{\omega^2}{z^2} \cdot \frac{\tau}{\tau_D}}} \tag{6.2}$$

with the average number of diffusers $\langle N \rangle$ within the detection volume V which is turn defined by the lateral and axial diameter ω and z. On this basis the concentration $\langle C \rangle$ can be determined via

$$\langle C \rangle = \frac{\langle N \rangle}{V} \tag{6.3}$$

The diffusion time τ_D states how long the diffuser stays within the sensing volume. In the autocorrelation it represents the time at which the amplitude is decreased to half of the original value. Then, the diffusion constant which is defined by the Stokes-Einstein equation (see *formula 6.4* with the Bolzman constant k_B, the temperature T, the dynamic viscosity of the surrounding solvent μ and the hydrodynamic radius R_H of the diffuser) can be calculated via *formula 6.5*.

$$D = \frac{k_B T}{6\pi\eta R_H} \tag{6.4}$$

$$\tau_D = \frac{r_0^2}{4D} \tag{6.5}$$

The utilization of confocal optical microscope techniques led to an impressive development of this method[159] which opened a window for a wide range of applications such as sequencing of single DNA strains[160] or monitoring conformational changes of single molecules.[161] A high resolution is possible due to its small detection volume, usually in the order of 1 fl or less.[162, 163] Therefore, only a small sample volume is required. However, Fluorescence Correlation Spectroscopy is also limited through 2 major disadvantages. First, the highest possible concentration of diffusers is usually below the concentrations existent in biological systems. Second, the analyte has to be labeled with a fluorescent dye. However, the addition of dyes increases the hydrodynamic radius of the diffusers, its diffusion behavior changes and consequently the measured results are falsified.[164] Beyond, experiments suffer from quenching or bleaching effects.[165]

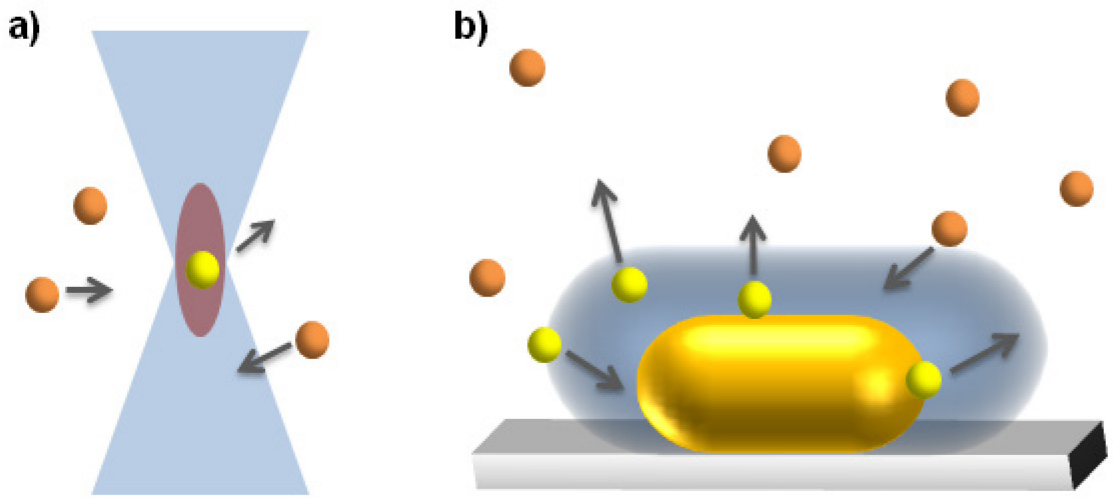

Figure 36. Illustration of different kinds of detection volumes for the determination of diffusion constants. **a)** The detection volume (red) of the well-established Fluorescence Correlation Spectroscopy technique is schematically represented. It is Gaussian shaped and usually about 0.5 µm3. This figure originates with sight variation from Dr. Liane Slaughter. **b)** Within this project the sensing volume of a single gold nanorod (blue) is used as detection volume. This approach is named Plasmon Correlation Sensing. The figure originates with sight variation from literature [57].

In this chapter, I present an alternative and novel approach to for the measurement of diffusion constants with a highly reduced detection volume named *Plasmon Correlation Sensing*. The sensing volume of a single, immobilized nanorod is used as detection volume (see *Figure 36b*). When a diffusing particle enters the detection volume a shift in the resonance wavelength of the plasmon sensor is introduced. In comparison to Fluorescence Correlation Spectroscopy, the diffusers can now be studied in their natural appearance as no labeling is necessary. Further, the sensing volume is in the range of zepto- to attoliters.[26] Consequently, Wang *et al.*[166] managed to measure diffusion constants with analyte concentration in the nanomolar regime by using an individual gold nanoparticle as optical nano-antenna in a Fluorescence Correlation Spectroscopy setup.

The residence time of the diffusing particles within the sensing volume τ_D as well as the induced shifts of the resonance wavelength of the senor $\Delta\lambda_{int}$ (see *Figure 37*) are dependent of many parameters. The residence time depends on the hydrodynamic radius of the diffuser, the viscosity of the surrounding medium, the temperature and the size of the detection volume (see *formula 6.5*). The induced shift on the other hand depends not only on sensor dimensions, but also on the size and material of the diffusers. Further, the

position of diffuser and sensor to relative each other also has an influence on the exact amount of the shift.[22] The diffuser has to fulfill many requirements. For instance, the particles must not stick to glass or to the sensor itself. Furthermore, the particles should be soluble in water as well as in glycerin, must not aggregate, have a uniform size and a small size distribution. The kinds of nanoparticles which fulfill all these requirements are gold nanospheres. Due to plasmon coupling gold spheres can induce larger shifts in comparison to dielectric particles of the same size.[51] As the gold spheres should not be attracted to the CTAB layer of the sensor or to glass, the diffusers where functionalized with methoxy polyethylene glycol. This functionalization led at the same time to an increased solubility at high concentrations.

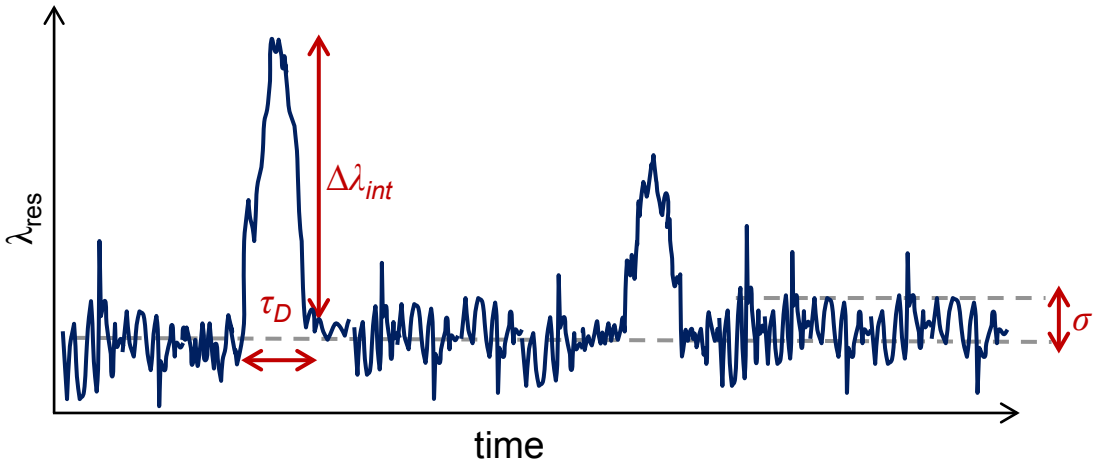

Figure 37. Schematic illustration of a measured signal in a PCS experiment. The resonance wavelength of a gold nanorod is monitored over time. When a diffusing particle is located in the sensing volume with the diffusion time τ_D, a shift $\Delta\lambda_{int}$ is introduced. The signal-to-noise ratio has to be optimized as noise σ produced by the setup is present. This figure originates with sight variations from Dr. Liane Slaughter.

After an introduction to the principles of diffusion and an overview about various methods which are related to FCS (see *Chapter 6.2*) I present the principle of Plasmon Correlation Sensing and show how the diffusion time can be determined by following fluctuations in the resonance wavelength of a single gold nanorod over time. Further, I will show how the characteristic time constants depend on viscosity of the surrounding medium as well as on the diffuser size. Finally, I will discuss how the signal-to-noise-ratio can be optimized (see *Chapter 6.4*).

The protocol for the functionalization of the gold spheres which acted as diffusers originates from . The determination of the dimensions of the utilized nanoparticles via TEM was conducted by . At this point I also want to thank for helpful discussion.

6.2 Theory

6.2.1 Diffusion

Diffusion can be defined as a temperature driven movement of particles without further energy supply. To describe diffusion processes it has to be distinguished between diffusion in gas, in fluids and in solids. The following information is based on Atkins.[167]

To describe diffusion the first Fick's law can be applied:

$$J = -D\frac{dc}{dx} \tag{6.6}$$

Thereby, J is diffusion flux, D the diffusion coefficient and dc/dx the concentration gradient against the diffusion direction. Consequently, the diffusion flux is direct proportional to the concentration gradient. The diffusion flux can also be expressed through:

$$J = s \cdot c \tag{6.7}$$

with the drift velocity s and the concentration of particles c. With the thermodynamic force F as a result of the concentration gradient (R: universal gas constant, T: temperature)

$$F = -\frac{RT}{c}\left(\frac{dc}{dx}\right)_{p,T} \tag{6.8}$$

the drift velocity can also be described as follows:

$$s = \frac{D}{RT} \cdot F \tag{6.9}$$

If an ion in solution is exposed to an external electric field E with the force $z \cdot e \cdot E$ and $s = \mu E$ we can write:

$$D = \frac{\mu RT}{zN_A e} \tag{6.10}$$

with the mobility of the particles μ. The Stokes-Einstein law gives a relationship between the mobility of an ion in solution and the diffusion coefficient. Combining *formula 6.10* with

$$\mu = \frac{e \cdot z}{6\pi\eta a} \tag{6.11}$$

with the viscosity of the medium η and the radius of the particle a we can describe the diffusion coefficient D via:

$$D = \frac{kT}{6\pi\eta a} \tag{6.12}$$

The second Fick's law describes the relationship between temporal and real concentration gradients. Due to conservation of mass

$$\frac{dc}{dt} = -\frac{dJ}{dx} \tag{6.13}$$

we can write:

$$\frac{dc}{dt} = D\frac{d^2c}{dx^2} \tag{6.14}$$

To express the concentration gradient in a more general way convection has to be included. The convection flow can be described as a particle flux through an area A during a time interval Δt due to a flow with the velocity v:

$$J = \frac{cAv\Delta t}{A\Delta t} = cv \tag{6.15}$$

then we can write

$$\frac{dc}{dt} = -v\frac{dc}{dx} \tag{6.16}$$

Combing *formula 6.16* with *formula 6.14* a general expression to describe diffusion is:

$$\frac{dc}{dt} = D\frac{d^2c}{dx^2} - v\frac{dc}{dx} \tag{6.17}$$

6.2.2 State of the Art: Improvement of Fluorescence Correlation Spectroscopy in Terms of Volume Reduction

To overcome the limitations through the large detection volume caused by the optical diffraction limit and restrictions through a low signal-to-noise ratio the technique of Fluorescence Correlation Spectroscopy has been developed by mainly two different approaches. One strategy is to shape the laser excitation beam in an unconventional manner. Alternatively, photonic structures can be applied.[163] In the following I will give a brief overview about these two approaches and focus on improvements in terms of volume reduction and fluorescence enhancement. To reduce the detection volume in longitudinal direction Total Internal Reflection Fluorescence Microscopy (TIRF) can be applied.[168] Volume reduction by a factor of 6 combined with strong fluorescence enhancement[163] can also be realized via Fluorescence Detection on a mirror. Thereby, the laser beam is reflected on a dielectric mirror and an interference pattern is produced.[169] With Stimulated Emission Depletion Microscopy (STED) the excitation of the fluorescence occurs by a regular focal, green spot whereas a second, red beam causes the stimulation of the molecules down to their ground state.[170] This leads to a volume reduction by a factor of 100 since the fluorescence only takes place at the very center of the focal spot.[163] One example to improve the detection of the fluorescence signal with the help of photonic structures is the usage of a paraboloid detector which leads to large fluorescence collection angles and has been demonstrated successfully for measurements in lipid membranes.[171] Gold Nanoparticles have also already been applied in FCS in terms of field enhancement.[166, 172] Thereby, single gold spheres were placed into the detection volume and acted as nano-antennas.

6.3 Experimental Details

Materials Glycerin and sodium chloride were bought from *Sigma.* As sensors gold nanorods were applied. The synthesis is described in *appendix A1*, further details on sensor dimensions can be found in *appendix C1*. Gold nanospheres served as diffusers. The 9 nm and 44 nm gold spheres were purchased from *BBInternational*. The 17 nm gold spheres synthesized according to *appendix A2*. To avoid aggregation of the particles as well as sticking to the glass surface or to the sensor, the spheres were functionalized with poly (ethylene glycol) (PEG) purchased from *Iris Biotech GmbH* and were after that centrifuged to reduce the size distribution. The functionalization and centrifugation protocol can be found in *appendix B* and further characterization of the samples in *appendix C2*. In order to increase the diffusion time of the diffusers within the detection volume, the samples were mixed with different portions of glycerin.

Sample Preparation As flow cell a glass capillary (dimensions 100 mm x 2 mm x 0.1 mm) connected with flexible tubing was utilized. Between flow cell and half cylinder immersion oil was deposited. The immobilization of the gold rods on the glass surface was achieved by rinsing with a 1M solution of sodium chloride. After the solutions containing the diffusers were introduced the tubing was lifted so that no flow took place and affected the measurements.

Setup *Chapter* 3 describes the applied microscope. The measurements were conducted with the so called *crop mode* which enables a temporal resolution in the microsecond regime. The exposure times ranged from 31 µs to 200 µs with a readout time of 75 µs. Gain was adjusted ranging between gain factor 20 and gain factor 60.

Data Evaluation Each timetrace was cut into 20 equidistant pieces and each of them was detrended separately. The fluctuation amplitudes of each sequence were averaged and the mean values and standard deviations are given in the following. The autocorrelations of each sequence were averaged as well. To determine the kinetic time constant τ_D the autocorrelations were described with an exponential fitting function. The error bars in der following figures represent the accuracy of the fit.

6.4 Results and Discussion

6.4.1 Principle

For the investigation of diffusion processes gold nanorods with a mean size of 35 x 78 nm where utilized as sensors. After immobilizing the rods on the surface of the glass capillary spectra of one single particle were acquired and the changes of the resonance wavelength over time were monitored (timetrace). *Figure 38a* shows the timetrace of a gold nanorod surrounded by a solution containing 50% glycerin (blue line) and the timetrace of the same nanorod surrounded by a solution containing 50% glycerin and gold nanospheres with a mean diameter of 17 nm (concentration: $1.3 \cdot 10^{11}$ particles/ml) as well (red line). First of all, an increase in the fluctuation amplitude from 0.65 nm to 0.66 nm can be observed. This corresponds to a signal-to-noise ratio (S/N) of 1.02. Consequently, a S/N ≈ 1 is sufficient to be able to extract the diffusion time τ_D from the autocorrelation of the timetrace (see *Figure 38b*). The autocorrelation was calculated by cutting the timetrace into 20 equidistant pieces and detrending each of them separately. Thereafter, the autocorrelations of each sequence were averaged. The autocorrelation can be described by:

$$ACF = a \cdot \exp\left(-\frac{t}{\tau_D}\right) + b \tag{6.18}$$

Applying this fitting function to the presented autocorrelation the value for the diffusion time τ_D can be amounted to 2.1 ms. Knowing the resonance position and the full width at half maximum (*FWHM*) of the sensor, it is possible to determine its dimensions[58, 138] and thus to calculate its sensing distance r_0 (formula according to simulations by):

$$r_0 = \frac{1}{b \cdot 5.2336 \cdot AR^{-0.6551}} \tag{6.19}$$

Thereby, b and AR are defined as width and aspect ratio of the rod. In this experiment a sensor with the dimensions of 41 x 79 nm was used. With a sensing distance of 12 nm the sensing volume is amounted to $9 \cdot 10^4$ nm^3 under the assumption that the glass substrate limits the sensing volume to half of the volume around the rod.

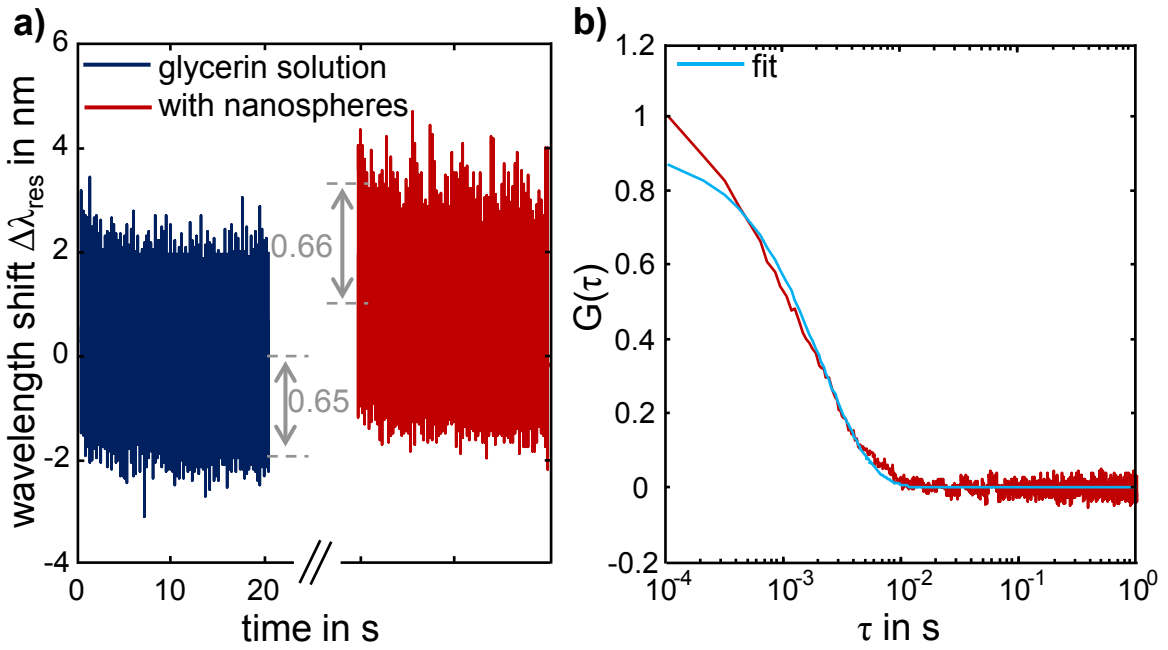

Figure 38. Determination of the diffusion time. **a)** Timetrace of the resonance wavelength of a single gold nanorod in a 50% glycerin solution without (blue) and with gold nanospheres (red, size: 17 nm). An increase in the fluctuation amplitude can be observed. **b)** The corresponding autocorrelation shows an exponential trend which yields the diffusion time τ_D.

6.4.2 Variation of Viscosity

A parameter which influences the diffusion time τ_D is the viscosity of the surrounding medium (see *Figure 39a*). The higher the viscosity η the smaller is the diffusion constant D and thus the longer the diffusers stay within the sensing volume and τ_D increases. To confirm that the exponential trend of the autocorrelation really arises from diffusing particles timetraces were measured under variation of the percentage of glycerin in the surrounding solution in equidistant steps. The autocorrelation of each timetrace was calculated (see *Figure 39b*) and the corresponding diffusion time τ_D was extracted (see *Figure 39c*).

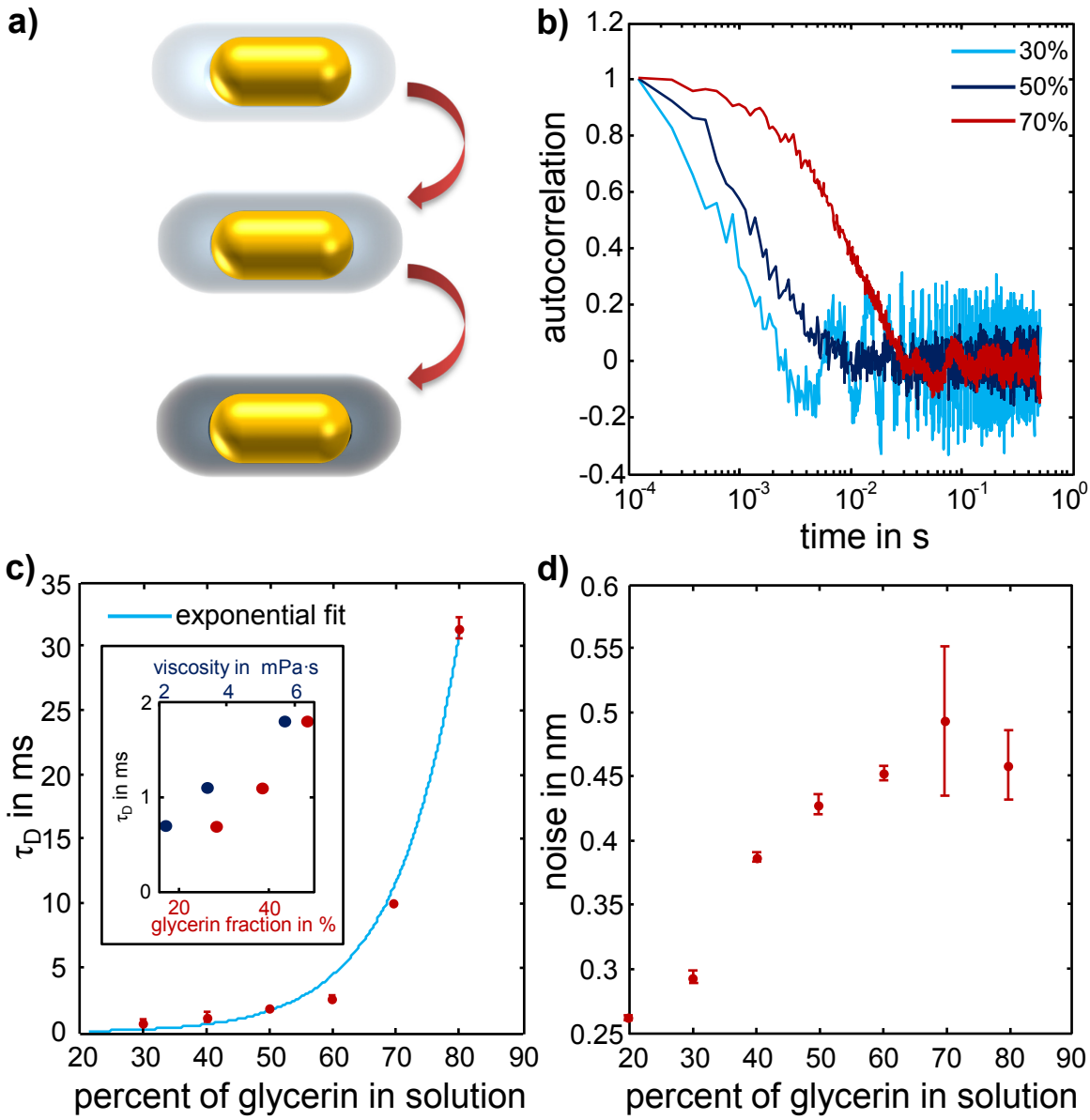

Figure 39. PCS experiments under variation of the glycerin concentration. 17 nm spheres served as diffusers. **a)** The percentage of glycerin in solution is varied. **b)** Autocorrelations of the timetraces measured in 30%, 50% and 70% glycerin solution are exemplarily shown. **c)** The diffusion time of the diffusing gold spheres depends on the viscosity of the medium. The error bars refer to the accuracy of the fit. The trend was approximated with an exponential fit. The inset shows the diffusion time plotted additionally plotted against the viscosity (blue). **d)** The fluctuation amplitude increases as well. The error bars represent the standard deviation.

τ_D shows an exponential growth with higher percentage of glycerin in solution. This is in accordance with theory since the viscosity of the medium increases exponentially with increasing glycerin fraction, too (see inset *Figure 39c* and *appendix D, Figure 44*). Only the diffusion times of diffusing particles in media containing at least 30% of glycerin or higher

could be gained through approximating the corresponding autocorrelation with an exponential fit. From samples with a glycerin fraction from 0-20% no exponential decrease in the autocorrelation could be observed. The reason for this lies in the fact that the signal-to-noise ratio increases with higher values of τ_D according to:

$$\frac{signal}{noise} = \frac{\Delta\lambda_{\text{int}} \cdot \tau_D}{t_{exp} \cdot \sigma} \tag{6.20}$$

Thereby, $\Delta\lambda_{int}$ is the shift of the resonance wavelength of the sensor caused by a single diffusion event, t_{exp} corresponds to the exposure time for the measurement and σ to the fluctuation amplitude of the timetrace (also compare with *Figure 37*). This is reflected in *Figure 39d*. A continuous increase of the noise ratios of the measured timetraces with a higher glycerin fraction is shown. Further timetraces under variation of the glycerin ratio including the corresponding autocorrelations can be found in *appendix G, Figure 51*.

6.4.3 Signal-to-Noise Optimization

To be able to characterize the diffusion kinetics of samples which show only small diffusion times (particularly samples with small diffuser sizes and low viscosity of the surrounding medium) it is necessary to maximize the signal-to-noise ratio. One possibility to improve the signal-to-noise ratio is to measure with the highest possible exposure time as the spectral noise decreases with increasing temporal resolution (see *Figure 40a*, blue). However, as diffusion is a very fast process a certain time resolution is necessary. The question, which is the highest possible exposure time to measure a dynamic process, is not easy to answer even if the characteristic time constant is roughly known. In theory, it is sufficient to measure twice as fast as the dynamic process takes place. In experiments however, a higher temporal resolution is necessary due to the presence of instrumental noise. As a rule of thumb, the exposure time should be a factor of 10 lower than the system under investigation. Within this project, diffusion processes with diffusion times within the detection volume up to 500 µs were monitored. *Figure 40a* shows the fluctuation amplitudes of timetraces taken under various exposure times in a 50% glycerin solution with and without diffusing particles present. The sensor had dimensions of 41 nm x 79 nm which corre-

sponds to a detection volume of $9 \cdot 10^4$ nm^3. The highest signal-to-noise ratio is reached with exposure times of 50-100 µs. 200 µs is already a too low sampling frequency to be able to monitor the diffusion process. The signal-to-noise ratio was below 1 and the corresponding autocorrelations didn't show an exponential trend. More data points were not acquired due to the long time for data transfer from the EMCCD camera and the high need for storage capacity.

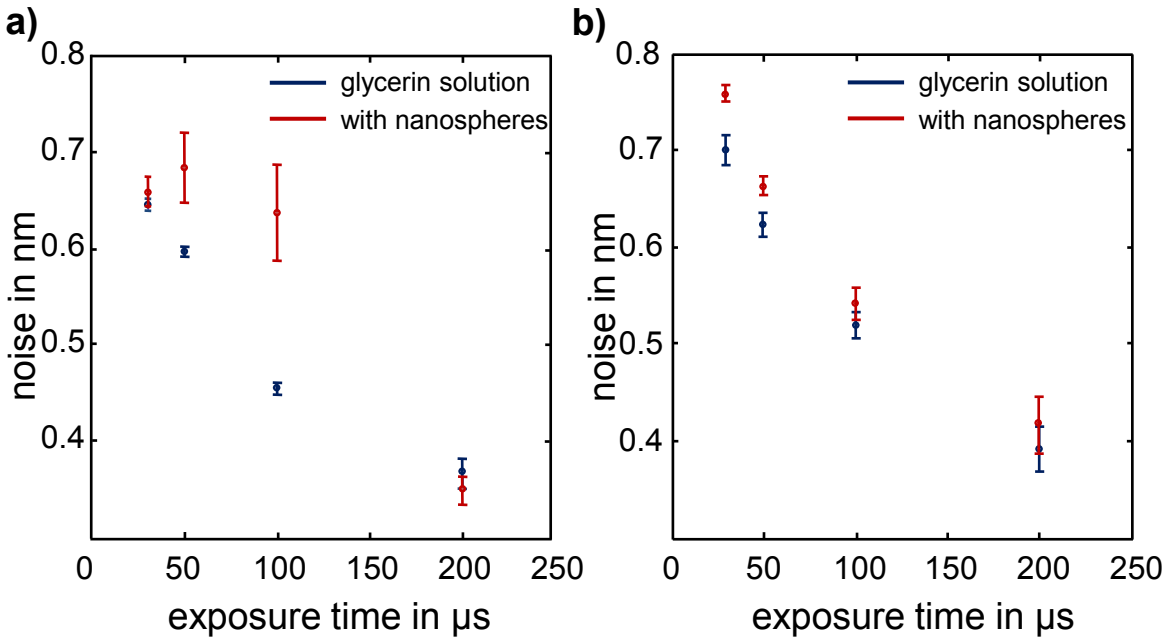

Figure 40. Dependency of the fluctuation amplitude on the utilized exposure time. Spectral noise of single gold nanorods in a 50% glycerin solution under variation of the exposure time without (blue) and with (red) diffusing particles (17 nm sized gold spheres) are presented. The error bars represent the standard deviation. **a)** A medium sized rod was applied as sensor. **b)** A big sized rod was utilized.

Another possible strategy is the right choice of the sensor size. In general, bigger nanorods provide a larger detection volume which consequently increases the diffusion time. Another advantage of the utilization of bigger sensors lies in the high scattering intensity of the plasmonic spectra. Consequently, the fluctuation amplitude of the base signal is reduced. However, the shift per diffusing particle is diminished (see *formula 6.20*). The question remains which of these two oppositional trends prevails. To experimentally demonstrate the dependency of the diffusion time from the detection volume of the sensor a diffusion measurement was repeated in three independent measurements while all other

parameters were kept constant (50% glycerin, 17 nm spheres, 30 µs exposure time). *Figure 41* shows that the diffusion time increases exponentially with increasing detection volume.

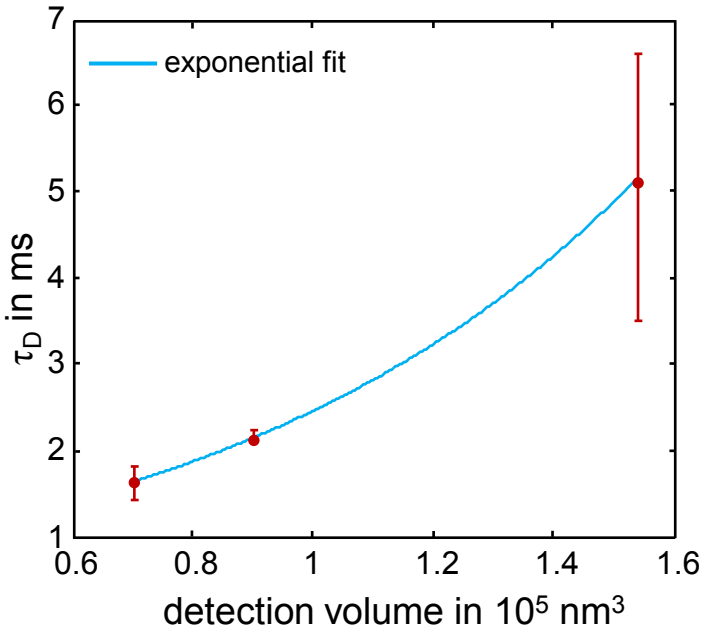

Figure 41. Dependency of the diffusion time on the sensor size. The diffusion time τ_D (red) increases with increasing detection volume. The trend was approximated with an exponential fit (blue). The error bars refer to the accuracy of the fit. The detection volumes were calculated under the assumption that only half of the sensing volume of the rods is accessible. The size of the diffusers was 17 nm, the solution contained 50% of glycerin.

To evaluate the optimal temporal time resolution for diffusion experiments with bigger sized sensors the same experiment as described above was repeated again. Timetraces were monitored under variation of the time resolution while other parameters were kept constant (50% glycerin, 17 nm spheres as diffusers). In this case a sensor with dimensions of 47 nm x 96 nm was utilized which leads to a detection volume of $15 \cdot 10^4$ nm^3. This is displayed in *Figure 40b*. The maximal achieved signal-to-noise ratio was 1.1. A reduction of the sensing volume roughly by a factor of two consequently leads to an increase in the signal-to-noise ratio from 1.0 to 1.4 in case of a temporal resolution of 100 µs. As a consequence, for further experiments it was carried on with medium-sized sensors.

6.4.4 Variation of the Diffuser Size

Finally, it was investigated which diffuser sizes can be detected (see *Figure 42*) as all prior experiments were conducted with spheres of a mean diameter of 17 nm.

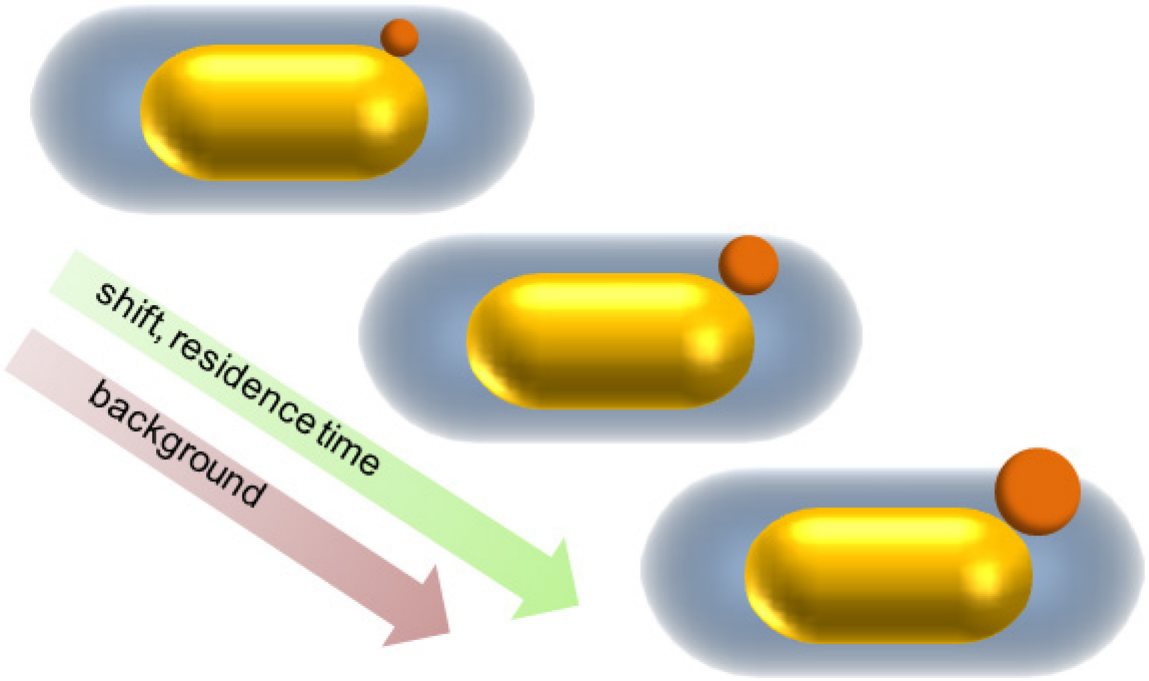

Figure 42. Influence of the diffuser size. Increasing the size of the diffusing particles leads to higher shifts in the resonance wavelength of the sensor and to longer diffusion times within the sensing volume. However, bigger diffusers also show a high scattering intensity by themselves. The figure originates wit slight variations from Dr. Liane Slaughter.

On the one hand, bigger sized diffusers are easier to measure. The signal-to-noise ratio is higher due to higher shifts per particle and higher residence times within the detection volume. On the other hand, bigger diffusers can contribute to background and consequently affect the spectrum of the sensor even if they are not localized within the detection volume. The smaller the particles the more challenging it is to determine the kinetic constants due to low signal-to-noise ratios. Besides of gold nanospheres with a diameter of 17 nm, samples containing spheres with mean diameters of 44 nm and 9 nm were applied. Timetraces were measured under variation of the percentage of glycerin in the surrounding medium and the diffusion times τ_D were determined from the autocorrelations (see *Figure 43a*). In all three cases, the diffusion times increase with the glycerin fraction in solution (also compare with *Chapter 6.4.2*). As the 44 nm-spheres provide a high signal-to-noise

ratio (see *Figure 43b*, *purple*), the diffusion times in the various glycerin containing media could be extracted easily by fitting the autocorrelations exponentially. It was even possible to determine τ_D in completely aqueous solution (0% glycerin). Nevertheless, they showed a high scattering intensity by themselves which also from time to time affected the plasmonic spectrum of the sensor (see *Figure 43b purple*, comparatively high error bars). It was also possible to determine the diffusion times of the 9 nm-spheres (see *Figure 43a*). The lowest glycerin fraction at which τ_D could be determined was 20%.

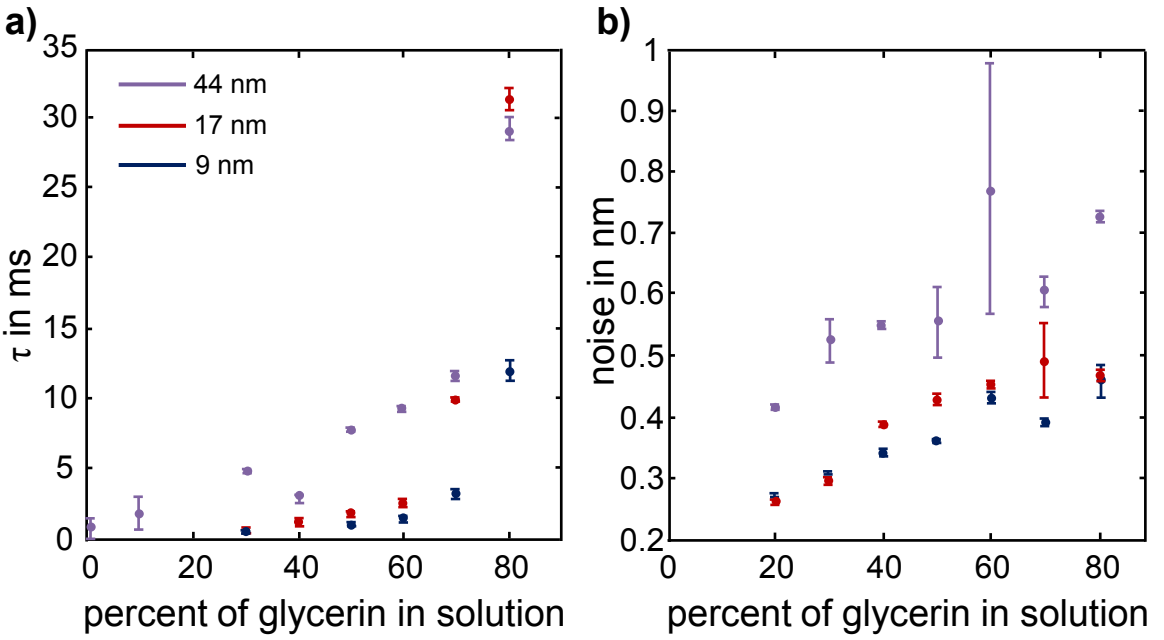

Figure 43. Measurements with different sized diffusers. The date of the 17 nm spheres corresponds to the measurement presented in *Figure 39*. **a)** The diffusion times of diffusing gold spheres depend not only on the viscosity of the medium but also on its size. The error bars refer to the accuracy of the fit. **b)** The corresponding fluctuation amplitudes are represented. The error bars represent the standard deviation.

When taking about the actual sizes of the diffusing spheres it has to be considered that they were functionalized with polyethylene glycol (MeO-PEG-SH, 840 Da, further details see *Chapter 6.3*). For discussion about the performance of the sensor and about the limit which is so far the smallest diffuser size which can be detected the values for the respective diameters determined via TEM are sufficient. The size of the shift per diffusing particle is dominated by plasmon coupling of diffuser and sensor and not by the local change of the refractive index introduced by the PEG shell. However, the PEG layer also contributes to

the hydrodynamic radius. Consequently, for further applications of the Plasmon Correlation Sensing method as the determination of diffusion coefficients it is of importance to include the surrounding layer. The total particle radius R_{total} has to be extended to:

$$R_{total} = a + R_{PEG} \tag{6.21}$$

with the radius of the diffuser a and the thickness of the PEG layer R_{PEG}.[173] A theoretical approximation of R_{PEG} is given by the Flory radius R_F which emanates from maximum entropy configuration:

$$R_F = N^{0.64} \cdot b \tag{6.22}$$

N stands for the number of monomers within one chain and b for the size of one unit. Thereby, one monomer is 3.5 Å.[174] Of course, maximal extended chain length R_{max} is given by the product of the number of monomers and the size:

$$R_{max} = N \cdot b \tag{6.23}$$

Table 4. Overview of the respective diameters of the utilized gold spheres which acted as diffusers in the plasmon correlation experiments. It has to be distinguished between the diameter of the gold spheres itself determined via TEM and the hydrodynamic radius taking the surrounding shell of polyethylene glycol into account. The radius can then be calculated under the assumption that a maximal extended chain length is present or the Flory Radius can be considered which emanates from maximum entropy configuration.

diffuser	diameter from TEM, in nm	inclusion of extended chain length, in nm	inclusion of Flory Radius, in nm
small	8.8	22.1	13.4
medium	16.6	29.9	21.2
big	43.6	56.9	48.2

Table 4 gives an overview about the respective diameters of the utilized diffusers. Besides of the values determined via TEM the diameters under inclusion of the Flory radius and the maximal radius of the PEG layer when the chain is extended to its maximum are presented. Hanauer *et al.*[173] found out that the real diameter is somewhere in between. Further, it has to be taken into account that the exact hydrodynamic radius also varies with the percentage of glycerin in solution. The exact values have to be determined experimentally, for example

via Dynamic Light Scattering. However, this technique is without further ado not applicable due to the high viscosity of the glycerin solutions. Consequently, the calculated values are so far a good approximation.

6.5 Conclusion and Outlook

In the previous chapter, the application to use the sensing volume of a single gold nanorod to determine diffusion constants was successfully demonstrated. Through following fluctuations in the resonance wavelength over time the residence time of a diffusing particle within the detection volume was extracted by approximating the corresponding autocorrelation with an exponential fit. To confirm that the calculated time constants really arise from diffusing processes an exponential growth of the diffusion time with increasing viscosity of the surrounding medium was observed. Furthermore, possibilities to improve the signal-to-noise ratio through the right choice of the sensor dimensions and the exposure time were discussed. The hereby developed measurement method worked out for the detection of diffusing gold spheres with sizes ranging from 9 nm to 44 nm.

The theory for Fluorescence Correlation Spectroscopy which was presented in *Chapter 6.1* is only applicable if the detection volume shows on the one hand a Gaussian profile and is on the other hand also far away from any surfaces. For the validation of the Plasmon Correlation Sensing a model function has to be found analytically or by numerical simulation to fit the calculated autocorrelations. This function depends on the shape and size of the detection volume

$$\Delta\lambda = F(x, y, z) \tag{6.24}$$

with the coordinates of the nanoparticles x, y, z. The mean shift of the plasmon resonance provides information about the concentration and can consequently be applied for normalization of the autocorrelation. Besides, the presence of a solid wall and eventually directed flow should be considered. The measured diffusion times are drastically higher than theoretical values calculated for the same conditions but under the assumption that the detection volume is Gaussian shaped and freestanding. For the example demonstrated in

Chapter 5.4.1.1 a theoretical value of 0.02 ms can be calculated. This differs from the experimental value by a factor of 100. This observation stands in agreement with Wang *et al.*[166] who also observed higher diffusion times within the detection volume of diffusing particles when introducing a gold nanoparticle for field enhancement in a FCS experiment. Apparently, the surface acts as an obstacle for diffusing particles. When a model is available, it will be possible to determine the final diffusion constant which is independent of the size of the detection volume. Additionally, also the calculation of concentrations and viscosities will be realized.

Table 5. Overview of selected techniques for the determination of diffusion constants (for more details see *Chapter 6.2.2*). The first publications as well as the volume reduction in comparison to the standard Fluorescence Correlation Spectroscopy technique are shown.

technique	publication	volume reduction
Fluorescence Correlation Spectroscopy	Elson *et al.*[157] 1974	x 1
Total Internal Reflection Fluorescence	Thompson *et al.*[168] 1981	x 10
Stimulated Emission Depletion Microscopy	Kastrup *et al.*[170] 2005	x 10
Near-Field Enhancement via gold nanoparticles	Estrada *et al.*[172] 2008	x 10000
Plasmon Correlation Sensing	2013	x 5000-10000

The sensing volume is typically in the range of $7.25 \cdot 10^4$ nm^3 for the sensors applied in these experiments (mean diameter: 35 nm, mean aspect ratio: 2.2) whereas the detection volume in a standard FCS experiment is usually about 0.5 µm^3.[163] *Table 5* compares selected techniques for detection of single molecules (an overview about these methods is already given in *Chapter 6.2.2*) in terms of reduction of the detection volume. The Plasmon Correlation Sensing method shows a volume reduction comparable to FCS techniques combined with near-field enhancement. This opens a window to utilize concentrations in the micro- and millimolar regime and consequently to study biological systems. In this project, gold nanospheres were used as diffusers. They could only be applied in a nanomolar concentration because they either couldn't be centrifuged down to higher concentrations

or further centrifugation let to aggregation and contribution to background so that a measurement of the samples was not possible. Further, it has to be considered that the average number of diffusers within the detection volume is inversely proportional to the y-intercept *G(0)* of the autocorrelation. A low concentration increases therefore the magnitude of the intercept and the quality of the autocorrelation is improved.

Plasmon Correlation Sensing is limited through 2 major disadvantages. First of all, the signal-to-noise ratio is restricted to the size of the diffusing particles. The smaller the particles the smaller is the shift per particle. This limitation does not occur in FCS as the measured parameter is the intensity of the fluorescent dye. Second, through dye labeling specific recognition can easily be realized. Fries *et al.*[175] even managed to identify different dye molecules via their characteristic fluorescence lifetime. Plasmon Correlation Sensing on the other hand will be demanding to apply in real biological environments where besides of the particles under investigation many other components which can shift the resonance position of the sensor as well are present. Beyond, *in vivo* studies have to be carefully analyzed since the inhomogeneous cellular environment acts as obstacles for the diffusers under investigation which leads to an alteration of the kinetic constants.[162]

Further developments of the method of Plasmon Correlation Sensing should focus on improvement of the signal-to-noise ratio. In my opinion, there are mainly two strategies. First, an even stronger light source can be applied to improve the quality of the plasmonic spectrum of the sensor and thus to reduce the fluctuation amplitude of the base signal. Second, the utilization of rods with higher aspect ratios would lead to higher shifts per diffusing particles. With these improvements it might be possible to study diffusion processes of dielectric particles, particularly of proteins in aqueous conditions. As proteins shift the resonance wavelength of the sensor due to changes in the refractive index and not due to plasmon coupling like the here utilized gold spheres lower shifts per diffusing particles are expected. The gold nanospheres could only be applied in nanomolar concentrations. Consequently, it would then be a desirable aim to test the limit of concentration that can be utilized for the determination of diffusion constants. Beyond, the diffusion constant of particles is strongly dependent on temperature. Installing a temperature

controlled device on the microscope would also give access to study diffusion in a temperature dependent manner.

All in all, single plasmonic sensors can be applied as new method to study diffusion kinetics and a volume reduction by a factor of 5000-10000 in comparison to the standard FCS technique is given. Additionally, the technique provides surface sensitivity and can thus be applied for the investigation of diffusion processes at the solid-liquid interface. As no labeling with fluorescent dyes is necessary the proposed detection scheme does not suffer from bleaching effects or alteration of the hydrodynamic radius. Finally, the Plasmon Correlation Sensing holds potential for exact determination of diffusion constants in vitro.

Chapter 7

Some physicists would prefer to come back to the idea of an objective real world whose smallest parts exist objectivly in the same sense as stones or trees exist independently of whether we observe them.

This, however, is impossible.

-- Werner Heisenberg

7 Summary and Outlook

Within this thesis plasmonic nanoparticles were for the first time applied as sensors to resolve and quantify adsorption and diffusion kinetics.

Plasmonic nanoparticles (further details see *Chapter 2*) are ideal candidates to investigate processes on the single molecule level due to their small sensing area. Consequently, only few molecules can adsorb at a time and fluctuations in the measured signal can be monitored whereas in conventional optical sensors many molecules can adsorb and fluctuations cancel each other out. To achieve the required temporal resolution and high signal-to-noise-ratio necessary to investigate these dynamic processes on the single-molecule level the Plasmon Fluctuation Setup was introduced in *Chapter* 3. In comparison to conventional dark-field microscopes a white light laser is coupled onto the sample via total internal reflection and an EMCCD camera is implemented as sensitive detector.

First, I investigated adsorption at the non-equilibrium as well as at the equilibrium state. In *Chapter* 4 the adsorption of single molecules of the blood plasma protein fibrinogen was monitored by following the resonance wavelength of one single nanorod over time. A systematic evaluation of the time between discrete steps within a timetrace suggests that one single adsorption event is resolved as a two-step process with a mean time of 7 s between the steps. A comparison of this result with actual publications about the adsorption behavior of fibrinogen assigns the first step to the adsorption of the fibrinogen molecule itself and the second step to the bending of the middle E domain towards the surface of the sensor. This holds potential for further investigation of conformational changes of different kind of proteins under different conditions.

Chapter 5 gives an experimental demonstration of how adsorption kinetics can be described through observation of equilibrium coverage fluctuations. In comparison to conventional methods like Surface Plasmon Resonance this approach enables to extract the rate constants within one single experiment, is not affected by mass transport as well as by long term drifts in the measuring signal. Studies on the optimization of the signal-to-noise ratio demonstrated the importance of the right choice of the sensor size as well as the utilized concentration. As system under investigation the surfactant sodium dodecyl sulfate was applied in an aqueous salt solution. The observation of its equilibrium coverage fluctuations for longer time above the critical micelle concentration allowed the classification into an initial slow and a second faster adsorption dynamic which arises probably from reorganization processes of micellar structures on the sensor surface. This phenomenon has so far not experimentally been accessible in this manner and gives now further insight into the adsorption process of SDS on the molecular level. The effect, why sodium dodecyl sulfate causes a blue shift in the resonance wavelength of a gold nanorod remains not fully understood. However, the basis for a new regime of plasmon sensing which enables the detection of small molecules is set.

In *Chapter* 6 the sensing volume of a gold nanorod was applied as detection volume to observe diffusion of gold nanospheres. Thereby, a diffusing particle entering the sensing volume introduces a shift in the resonance wavelength. An exponential growth of the

diffusion time with higher viscosity of the surrounding medium was found which served as control experiment and as confirmation that the extracted time constants are real. As diffusing particles gold spheres with sizes ranging from 9 nm to 43 nm can be detected. Investigations on the optimization of the signal-to-noise ratio suggest an exposure time of 50-100 µs and the usage of a nanorod with mean size of 35 x 78 nm as most practical sensor. In comparison to the conventional Fluorescence Correlation Spectroscopy technique a volume reduction by a factor of 5000-10000 is reached. This holds many advantages like the utilization of concentrations in the micro- and millimolar regime and circumstance that no labeling with fluorescent dyes is necessary. For validation of the Plasmon Correlation Sensing method a mathematical model is needed to describe the autocorrelation which takes the more complex geometry of the detection volume as well as presence of a surface into account.

In summary, this thesis provides a basis for novel applications of plasmonic nanoparticles in the field of sensing. Nanoparticles can be utilized to study dynamic processes on the molecular level. Therefore, the two most fundamental kinetic processes- adsorption and diffusion- were investigated with model systems. This experience will open a window to get deeper understanding about more complex biological systems.

8 Bibliography

[1] I. Ament, *personal communication* **2013**.

[2] V. Srinivasan, V. K. Pamula, R. B. Fair, *Lab Chip* **2004**, *4*, 310.

[3] G. F. Blackburn, H. P. Shah, J. H. Kenten, J. Leland, R. A. Kamin, J. Linl, J. Peterman, M. J. Powell, A. Shaj, D. B. Talley, *Clinical Chemistry* **1991**, *37*, 1534.

[4] J. S. Alford, *Computers & Chemical Engineering* **2006**, *30*, 1264.

[5] M. Beyer, C. Menzel, R. Quack, T. Scheper, K. Schügerl, *Biosensors and Bioelectronics* **1994**, *9*, 17.

[6] C. Krantz-Rülcker, M. Stenberg, F. Winquist, I. Lundström, *Analytica Chimica Acta* **2001**, *426*.

[7] K. G. Ong, C. A. Grimes, C. L. Robbins, R. S. Singh, *Sensors and Actuators A: Physical* **2001**, *93*, 33.

[8] M. Altamirano, L. Garcia-Villada, M. Agrelo, L. Sanchez-Martin, L. Martin-Otero, A. Flores-Moya, M. Rico, V. Lopez-Rodas, E. Costas, *Biosensors and Bioelectronics* **2004**, *19*, 1319.

[9] A. J. Haes, R. P. V. Duyne, *J. Am. Chem. Soc.* **2002**, *124*, 10596.

[10] V. Vamvakaki, N. A. Chaniotakis, *Biosensors and Bioelectronics* **2007**, *22*, 2650.

[11] S. Zhang, N. Wang, H. Yu, Y. Niu, C. Sun, *Bioelectrochemistry* **2005**, *67*, 15.

[12] L. M. d. C. Silva, A. C. S. A. Pinto, A. M. Sagado, M. A. Z. Coelho, of *Biosensors-Emerging Materials and Applications* (Ed.: P. A. Serra), InTech, **2011**.

[13] Helmholtz Centre for Environmental Research-UFZ, *http://www.ufz.de/index.php?en=13023* **2014**.

[14] A. Janshoff, C. Steinem, *Sensors Update* **2001**, *9*, 313.

[15] J. Wang, *Analyst* **2005**, *130*, 421.

[16] X. Fan, I. M. White, S. I. Shopova, H. Zhu, J. D. Suter, Y. Sun, *Analytica Chimica Acta* **2008**, *620*, 8.

[17] K. Matsubara, S. Kawata, S. Minami, *Applied Optics* **1988**, *27*, 1160.

[18] P. Pattnaik, *Applied Biochemsitry and Biotechnology* **2005**, *126*, 79.

[19] I. Ament, *PhD defence presentation* **2012**.

[20] C. Sönnichsen, T. Franzl, T. Wilk, G. v. Plessen, J. Feldmann, O. Wilson, P. Mulvaney, *Phys. Rev. Letters* **2002**, *88*, 077402.

[21] C. L. Baciu, J. Becker, A. Janshoff, C. Sönnichsen, *Nano Letters* **2008**, *8*, 1724.

[22] I. Ament, J. Prasad, A. Henkel, S. Schmachtel, C. Sönnichsen, *Nano Letters* **2012**, *12*, 1092.

[23] K. Kopitzki, P. Herzog, *Einführung in die Festkörperphysik*, Vieweg+Teubner Verlag, **2007**.

[24] P. B. Johnson, R. W. Christy, *Physical Review B* **1972**, *6*, 4370.

[25] C. F. Bohren, D. R. Huffman, *Wiley-Interscience* **1983**.

[26] S. A. Maier, *Plasmonics Fundamentals and Applications*, Springer ed., **2007**.

[27] R. Wilson, *Chem. Soc. Rev.* **2008**, *37*, 2028.

[28] J. Perez-Juste, I. Pastoriza-Santos, L. M. Liz-Marzan, P. Mulvaney, *Coordination Chemistry Reviews* **2005**, *249*, 1870.

[29] S. W. Prescott, P. Mulvaney, *Journal of Applied Physics* **2006**, *99*, 123504.

[30] K. S. Lee, M. A. El-Sayed, *J. Phys. Chem. B* **2005**, *109*, 20331.

[31] J. Becker, I. Zins, A. Jakab, Y. Khalavka, O. Schubert, C. Sönnichsen, *Nano Letters* **2008**, *8*, 1719.

[32] M. Z. Liu, P. Guyot-Sionnest, *Journal of Physical Chemistry B* **2004**, *108*, 5882.

[33] A. Jakab, C. Rosman, Y. Khalavka, J. Becker, A. Trügler, U. Hohenester, C. Sönnichsen, *ACS Nano* **2011**, *5*, 6880.

[34] Y. Khalavka, J. Becker, C. Sönnichsen, *J. Am. Chem. Soc.* **2009**, *131*, 1871.

[35] L. Mann, A. Henkel, **unpublished results**.

[36] J. Becker, A. Trügler, A. Jakab, U. Hohenester, C. Sönnichsen, *Plasmonics* **2010**, *5*, 161.

[37] M. Tarantola, A. Pietuch, D. Schneider, J. Rother, E. Sunnick, C. Rosman, S. Pierrat, C. Sönnichsen, J. Wegener, A. Janshoff, *Nanotoxicology* **2011**, *5*, 254.

[38] K. A. Willets, R. P. V. Duyne, *Annual Review of Physical Chemistry* **2007**, *58*, 267.

[39] P. K. Jain, X. Huang, I. H. El-Sayed, M. A. El-Sayed, *Plasmonics* **2007**, *2*, 107.

[40] C. Rosman, J. Prasad, A. Neiser, A. Henkel, J. Edgar, **2013**.

[41] N. J. Halas, S. Lal, W.-S. Chang, S. Link, P. Nordlander, *Chem. Rev.* **2011**, *111*, 3913.

[42] E. Prodan, C. Radloff, N. J. Halas, P. Nordlander, *Science* **2003**, *302*, 419.

[43] J. A. Fan, C. Wu, K. Bao, J. M. Bao, R. Bardhan, J. J. Halas, V. N. Manoharan, P. Nordlander, G. Shevets, F. Capasso, *Science* **2010**, *328*.

[44] E. Hao, G. C. Schatz, *Journal of Chemical Physics* **2004**, *120*, 357.

[45] K. H. Su, Q. H. Wei, X. Zhang, J. J. Mock, D. R. Smith, S. Schultz, *Nano Letters* **2003**, *3*, 1087.

[46] L. Gunnarsson, T. Rindzevicius, J. Prikulis, B. Kasemo, M. Kall, S. L. Zou, G. C. Schatz, *Journal of Physical Chemistry B* **2005**, *109*, 1079.

[47] P. K. Jain, W. Y. Huang, M. A. El-Sayed, *Nano Letters* **2007**, *7*, 2080.

[48] S. Sheikholeslami, Y.-W. Jun, P. K. Jain, A. P. Alivisatos, *Nano Letters* **2010**, *10*, 2655.

[49] T. Pakizeh, M. Käll, *Nano Letters* **2009**, *9*, 2343.
[50] L. S. Slaughter, Y. P. Wu, B. A. Willingham, P. Nordlander, S. Link, *ACS Nano* **2010**, *4*, 4657.
[51] L. S. Shao, C. Fang, H. Chen, Y. C. Man, J. Wang, H.-Q. Lin, *Nano Letters* **2012**.
[52] P. Mulvaney, *Langmuir* **1996**, *12*, 788.
[53] T. Ung, M. Giersig, D. Dunstan, P. Mulvaney, *Langmur* **1997**, *14*, 7392.
[54] A. Toyota, N. Nakashima, T. Sagara, *Chem. Phys. Lett.* **2004**, *349*, 1773.
[55] P. Mulvaney, J. Perez-Juste, M. Giersing, L. M. Liz-Marzan, C. Pecharroman, *Plasmonics* **2006**, *1*, 61.
[56] A. B. Dahlin, *Sensors* **2012**, *12*, 3018.
[57] I. Ament, *PhD thesis*, University of Mainz (Mainz), **2012**.
[58] A. Henkel, *PhD thesis*, University of Mainz (Mainz), **2013**.
[59] Z. Wu, N. E. Huang, *Proceedings of the Royal Society A* **2004**, *460*, 1597.
[60] F. N. Hooge, *Physics Letters A* **1969**, *29*, 139.
[61] A. Sapper, J. Wegener, A. Janshoff, *Anal. Chem.* **2006**, *78*, 5184.
[62] J. Becker, *PhD thesis*, University of Mainz (Mainz), **2010**.
[63] A. Curry, G. Nusz, A. Chilkoti, A. Wax, *Appled Optics* **2007**, *46*.
[64] C. J. Wilson, R. E. Clegg, D. I. Leavesley, M. J. Pearcy, *Tissue Eng.* **2005**, *11*, 1.
[65] P. Cacciafesta, A. D. L. Humphris, K. D. Jandt, M. J. Miles, *Langmuir* **2000**, *16*, 8167.
[66] M. W. Mosesson, *J. Lab. Clin. Med.* **1990**, *116*, 8.
[67] M. Jirousková, J. E. Dyr, J. Suttnar, K. Holada, B. Trnková, **1997**, *78*, 1125.
[68] P. Roach, D. Farrar, C. C. Perry, *J. Am. Chem. Soc.* **2005**, *127*, 8168.
[69] C. E. Hall, H. S. Slayter, *Biophys. Biochem. Cytol.* **1959**, *5*, 11.
[70] A. Agnihotri, C. A. Siedlecki, *Langmuir* **2004**, *20*, 8846.
[71] I. S. Yermolenko, V. K. Lishko, T. P. Ugarova, S. N. Magonov, *Biomacromolecules* **2011**, *12*, 370.
[72] Kollman, *Biochemistry* **2009**, *48*, 3877.
[73] S. Köhler, *personal communication* **2013**.
[74] L. E. Averett, M. H. Schoenfisch, *Analyst* **2010**, *1235*, 1201.
[75] B. M. Reinhard, S. Sheikholeslami, A. Mastroianni, A. P. Alvisatos, J. Liphardt, *Proc. Nat. Acad. Sci.* **2007**, *104*, 2667.
[76] A. Gunnarsson, P. Jonsson, V. P. Zhdanov, F. Hook, *Nucl. Acids Res.* **2009**, *37*, e99.
[77] A. Dolatshahi-Pirouz, T. Jensen, M. Fos, J. Chevallier, F. Besenbacher, *Langmuir* **2009**, *25*, 2971.

[78] G. Anand, S. Sharma, A. K. Dutta, S. K. Kumar, G. Belfort, *Langmuir* **2010**, *26*, 10803.

[79] M. Karlsson, J. Ekeroth, H. Elwing, U. Carlsson, *Journal of Biological Chemistry* **2005**, *280*, 25558.

[80] C. Chothia, *Annual Review of Biochemistry* **1984**, *53*, 537.

[81] W. Norde, *Pure & Appl. Chem.* **1994**, *66*, 491.

[82] S. M. Slack, T. A. Horbett, *ACS Symposium Series* **1995**, *602*, 112.

[83] N. L. Burns, K. Homberg, C. Brink, *Journal of Colloid and Interface Science* **1996**, *178*, 116.

[84] J. J. Jacobs, J. L. Gilbert, R. M. Urban, *The Journal of Bone & Joint Surgery* **1998**, *80*, 268.

[85] D. D. Deligianni, N. Katsala, S. Ladas, D. Sotiropoulou, J. Amedee, Y. F. Missirlis, *Biomaterials* **2001**, *22*, 1241.

[86] M. Tanaka, T. Motomura, M. Kawada, T. Anzal, Y. Kasori, T. Shiroya, K. Shimura, M. Onishi, A. Mochizuki, *Biomaterials* **2000**, *21*, 1471.

[87] M. Taborelli, L. Eng, P. Descouts, J. P. Ranieri, R. Bellamkonda, P. J. Aebischer, *J. Biomed. Mater. Res.* **1995**, *29*, 707.

[88] T. J. Lenk, T. A. Horbett, B. D. Ratner, K. K. Chittur, *Langmuir* **1991**, *7*, 1755.

[89] T. C. Ta, M. T. M. Dermott, *Anal. Chem.* **2000**, *72*, 2627.

[90] K. L. Marchin, C. L. Berrie, *Langmuir* **2003**, *19*, 9883.

[91] M. L. Clarke, J. Wang, Z. Chen, *J. Phys. Chem. B* **2005**, *109*, 22027.

[92] T. Smith, *Journal of Colliod and Inferface Science* **1980**, *75*, 51.

[93] H. B. Weiser, *A Textbook of Colloid Chemistry*, Wiley&Sons, New York, **1949**.

[94] J. Turkevitch, P. C. Stevenson, J. Millier, *Discuss. Faraday Soc.* **1951**, *11*, 55.

[95] J. Hemmerle, S. M. Altmann, M. Maaloum, J. K. H. Horber, L. Heinrich, J.-C.-. Voegel, P. Schaaf, *Proc. Nat. Acad. Sci. USA* **1999**, *96*, 6705.

[96] J. U. Keller, *Non-Equilib. Thermodyn.* **2009**, *34*, 1.

[97] D. Siegismund, T. F. Keller, K. D. Jandt, M. Rettenmayr, *Macromol. Biosci.* **2010**, *10*, 1216.

[98] B. Nikoobakht, M. A. El-Sayed, *Chem. Mater* **2003**, *15*, 1957.

[99] J. Vörös, *Biophys J.* **2004**, *87*, 553.

[100] P. Zijlstra, P. M. R. Paulo, M. Orrit, *Nature Nanotechnology* **2012**, *7*, 379.

[101] J. W. J. Kerssemakers, E. L. Munteanu, L. Laan, T. L. Noetzel, M. E. Janson, M. Dogterom, *Nature* **2006**, *442*, 709.

[102] J. Liu, U. Messow, *Colloid and Polymer Science* **2000**, *278*, 124.

[103] U. Larsson, B. Blombäck, R. Rigler, *Biochim Biophys Acta* **1987**, *915*, 172.

[104] K. J. Vahala, *Nature* **2003**, *424*, 839.

[105] A. A. Levchenko, B. P. Argo, R. Vidu, R. V. Talroze, P. Stoeve, *Langmuir* **2002**, *18*, 8464.

[106] S. F. Turner, S. M. Clarke, A. R. Rennie, P. N. Thirtle, D. J. Cooke, Z. X. Li, R. K. Thomas, *Langmuir* **1999**, *15*, 1017.

[107] S. C. Clark, W. A. Ducker, *J. Phys. Chem. B* **2003**, *107*, 9011.

[108] H. Gharibi, N. Takisawa, P. Brown, M. A. Thomason, D. M. Painter, D. M. Bloor, D. G. Hall, E. Wyn-Jonas, *J. Chem. Soc. , Faraday Trans* **1991**, *87*, 707.

[109] E. A. G. Aniansson, S. N. Wall, M. Almgren, H. Hoffmann, I. Kielmann, W. Ulbricht, R. Zana, J. Lang, C. Tondre, *J. Phys. Chem.* **1976**, *80*, 905.

[110] A. F. H. Ward, L. Tordai, *J. Chem.Phys.* **1946**, *14*.

[111] S. Manne, J. P. Cleveland, H. E. Gaub, G. D. Stucky, P. K. Hansma, *Langmuir* **1994**, *10*, 4409.

[112] S. Manne, H. E. Gaub, *Science* **1995**, *270*, 1480.

[113] W. A. Ducker, L. M. Grant, *J. Phys. Chem.* **1996**, *100*, 11507.

[114] V. Subramanian, W. A. Ducker, *Langmuir* **2000**, *16*, 4447.

[115] H. C. Schniepp, D. A. Saville, I. A. Aksay, *J. Am. Chem. Soc.* **2006**, *128*, 12378.

[116] M. Tanaka, A. Mochizuki, T. Motomura, K. Shimura, M. Onishi, Y. Okahata, *Colloids and Surfaces A: Physiochemical and Engineering Aspects* **2001**, *193*, 145.

[117] F. Höök, J. Vörös, M. Rodahl, R. Kurrat, P. Böni, J. J. Ramsden, M. Textor, N. D. Spencer, P. Tengvall, J. Gold, B. Kasema, *Colloids and Surfaces B: Biointerfaces* **2002**, *24*, 155.

[118] G. B. Sigal, M. Mkrsich, G. M. Whitesides, *Langmuir* **1997**, *13*, 2749.

[119] G. B. Sigal, M. Mkrsich, G. M. Whitesides, *J. Am. Chem. Soc.* **1998**, *120*, 3464.

[120] B. Liedberg, C. Nylander, I. Lunström, *Sensors and Actuators* **1983**, *4*, 299.

[121] A. Janshoff, H.-J. Galla, C. Steinem, *Angew. Chem.* **2000**, *112*, 4164.

[122] E. R. Nowak, J. B. Knight, E. Ben-Naim, H. M. Jaeger, S. R. Nagel, *Phys. Rev. E* **1998**, *57*, 1971.

[123] S. C. Biswas, D. K. Chattoraj, *Journal of Colliod and Inferface Science* **1998**, *205*, 12.

[124] E. S. Pagac, D. C. Prieve, R. D. Tilton, *Langmuir* **1998**, *14*, 2333.

[125] R. Atkin, V. S. J. Craig, S. Briggs, *Langmuir* **2001**, *17*, 6155.

[126] E. Lüthgens, A. Janshoff, *ChemPhysChem* **2005**, *6*, 444.

[127] E. Lüthgens, *Phd thesis*, Univerität Mainz (Mainz), **2005**.

[128] I. Langmuir, *J. Am. Chem. Soc.* **1918**, *40*, 1361.

[129] P. Schaaf, J. Talbot, *J. Chem. Phys.* **1989**, *91*, 4401.
[130] P. Schaaf, J. Talbot, *Phys. Rev. Lett.* **1989**, *62*, 175.
[131] E. Ruckenstein, *J. Coll. Int. Sci.* **1978**, *66*, 531.
[132] Z. Adamczyk, B. Senger, J.-C. Voegel, P. Schaaf, *J. Chem. Phys.* **1999**, *110*, 3118.
[133] Z. Adamczyk, P. Weronski, *Adv. Coll. Int. Sci.* **1999**, *83*, 137.
[134] Z. Adamczyk, B. Siwek, P. Warszynski, E. Musial, *J. Coll. Int. Sci.* **2001**, *242*, 14.
[135] I. Jokic, Z. Djuric, M. Frantlovic, K. Radulovic, P. Krstajic, Z. Jokic, *Sensors and Actuators B: Chemical* **2012**, *166-167*, 535.
[136] M. Frantlovic, I. Jokic, Z. Djuric, K. Radulovic, *Sensors and Actuators B: Chemical* **2013**, in press.
[137] S. Paria, C. Manobar, K. C. Khilar, *Ind. Eng. Chem. Res.* **2005**, *44*, 3091.
[138] A. Henkel, Y. Khalavka, A. Neiser, S. Schmachtel, *unpublished results*.
[139] J. K. Lu, I. P. Purcell, E. M. Lee, E. A. Simister, R. Thomas, A. R. Rennie, J. Penfold, *J. Coll. Int. Sci.* **1995**, *174*, 441.
[140] C. D. Bain, P. B. Davies, R. N. Ward, *Langmuir* **1994**, *10*, 2060.
[141] M. E. Montgomery, M. J. Wirth, *Langmuir* **1994**, *10*, 861.
[142] E. J. Wanless, W. A. Ducker, *J. Phys. Chem.* **1996**, *100*, 3207.
[143] V. K. Paruchuri, J. Nalaskowski, D. O. Shah, J. D. Miller, *Colliods and Surfaces A: Physiochem. Eng. Aspects* **2006**, *272*, 157.
[144] E. J. Wanless, T. W. Davey, W. A. Ducker, *Langmuir* **1997**, *13*, 4223.
[145] W. A. Ducker, E. J. Wanless, *Langmuir* **1999**, *15*, 160.
[146] T. Kyprianidou-Leodidou, W. Caseri, U. W. Suter, *J. Phys. Chem.* **1994**, *98*, 8992.
[147] C. Xu, J. irudayaraj, *Biophysical Journal* **2007**, *93*, 3684.
[148] SigmaAldrich, **2013**.
[149] K. A. Bunding-Lee, *Langmuir* **1990**, *6*, 709.
[150] K. Kastl, M. Menke, E. Lüthgens, S. Faiß, V. Gerke, A. Janshoff, C. Steinem, *Chem-BioChem* **2006**, *7*, 106.
[151] K. Kastl, M. Ross, V. Gerke, C. Steinem, *Biochemisitry* **2002**, *41*, 10087.
[152] R. D. Shesham, L. J. Bartolotti, Y. Li, *Protein Engineering, Design&Selection* **2008**, *21*, 115.
[153] S. Faiß, K. Kastl, A. Janshoff, C. Steinem, *Biochim Biophys Acta* **2008**, *1778*, 1601.
[154] K. Kastl, A. Herrig, E. Lüthgens, A. Janshoff, C. Steinem, *Langmuir* **2004**, *20*, 7246.
[155] D. Behn, S. Bosk, H. Hoffmeister, A. Janshoff, R. Witzgall, C. Steinem, *Biophys. Chem.* **2010**, *150*, 47.
[156] S. T. Hess, S. Huang, A. A. Heikal, W. W. Webb, *Biochemisitry* **2002**, *41*, 697.

[157] E. L. Elson, D. Magde, *Biopolymers* **1974**, *13*, 1.
[158] W. W. Webb, *Proc. Nat. Acad. Sci. USA* **1997**, *94*, 11753.
[159] R. Rigler, Ü. Mets, J. Widengren, P. Kask, *European Biophysics Journal* **1993**, *22*, 159.
[160] W. P. Ambrose, P. M. Goodwin, J. H. Jett, M. E. Johnson, J. C. Martin, B. L. Marrone, J. A. Schecker, C. W. Wilkerson, R. A. Keller, A. Haces, P.-J.Shih, J. D. Harding, *Ber. Bunsen-Ges. Phys. Chem.* **1993**, *97*, 1535.
[161] C. Eggeling, J. R. Fries, L. Brand, R. Günter, C. A. M. Seidel, *Proc. Natl. Acad. Sci. U.S.A.* **1998**, *95*, 1556.
[162] I. von d. Hocht, J. Enderlein, *Experimental and Molecular Pathology* **2007**, *82*, 142.
[163] J. Wenger, H. Rigneault, *Int. J. Mol. Sci.* **2010**, *11*, 206.
[164] C. Rosman, A. Henkel, A.Neiser, P.Schwille, C. Sönnichsen, *unpublished results* **2013**.
[165] S. Weiss, *Science* **1999**, *283*, 1676.
[166] Q. Wang, G. Lu, L. Hou, T. Zhang, C. Luo, H. Yang, G. Barbillon, F. H. Lei, C.A.Marquette, P. Perriat, O. Tillement, S. Roux, Q. Ouyang, Q. Gong, *Chemical Physics Letters* **2011**, *503*, 256.
[167] P. W. Atkins, J. d. Paula, *Physikalische Chemie*, Weinheim, **2006**.
[168] N. L. Thompson, T. P. Burghardt, D. Axelrod, *Biophys. J.* **1981**, *33*, 435.
[169] H. Rigneault, P. F. Lenne, *J. Opt. Soc. Am. B* **2003**, *20*, 2203.
[170] L. Kastrup, H. Blom, C. Eggeling, S. W. Hell, *Phys. Rev. Lett.* **2005**, *94*, 178104:1.
[171] J. Ries, T. Ruckstuhl, D. Verdes, P. Schwille, *Biophys. J.* **2008**, *94*, 221.
[172] L. C. Estrada, P. F. Aramendia, O. E. Martinez, *Optics Express* **2008**, *16*, 20597.
[173] M. Hanauer, S. Pierrat, I. Zings, A. Lotz, C. Sönnichsen, *Nano Letters* **2007**, *7*, 2881.
[174] C. Jeppesen, J. Y. Wong, T. L. Kuhl, J. N. Israelachvili, N. Mullah, S. Zalipsky, C. M. Marques, *Science* **2001**, *293*, 465.
[175] J. R. Fries, L. Brand, C. Eggeling, M. Köllner, C. A. M. Seidel, *J. Phys. Chem. A* **1998**, *102*, 6601.
[176] The Dow Chemical Company, *http://www.dow.com/optim/optim-advantage/physical-properties/viscosity.htm* **2013**.
[177] J. H. Clint, *J. Chem. Soc. , Faraday Trans 1* **1975**, *71*, 1327.

9 Appendix

A Nanoparticle Synthesis

A1 Rods

The synthesis of gold nanorods was conducted according to Nikoobakht *et. al.*.[98] The synthesis consisted of two steps. First, seeds were produced. Therefore, a solution containing 5 ml of de-ionized water, 5 ml of 0.2 M cetyl trimethylammonium bromide (*Sigma*) and 50 µl of 0.1 M tetracholoauric acid (*Sigma*) was prepared. Then, 600 µl of 0.02 M sodium borohydride (*Sigma*) was added while being cooled down with ice water. A brown coloration indicated a successful synthesis. In the growing step, a solution containing 3.848 ml of de-ionized water, 5 ml of 0.2 M cetyl trimethylammonium bromide (*Sigma*), 50 µl of 0.1 M tetracholoauric acid (*Sigma*) and 1 ml of 0.25 M sodium chloride was prepared. Then 20 µl of 0.04 M silver nitrate (*Sigma*) and 70 µl of 0.078 M ascorbic acid (*Sigma*) were added. To start the growth process, 12 µl of the previous prepared seed solution was added. To synthesize big rods, the protocol was altered as follows: For the growth solution, 200 µl of 1 M hydrochloric acid (*Merck*), 20 µl of 0.04 M silver nitrate (*Sigma*) and 80 µl of 0.1 M ascorbic acid (*Sigma*) were utilized and the seeds were diluted by a ratio of 1:10. The samples were stored at room temperature and heated up to 35 °C to resolve the crystallized CTAB before usage. To inject the rods into the flow cell for an experiment, a 1:50 dilution was usually prepared. The syntheses were kindly conducted by around 5 years ago. Consequently, aging processes in meantime cannot be excluded.

A2 Spheres

400 ml of 0.5 mM tetracholoauric acid (*Sigma*) were heated up to 95 °C while stirring. After that, 100 ml of 2 mM trisodium citrate (*Sigma*) were added. The solution first turned colorless, then black, purple and dark red. To avoid aggregation and aging processes, the sample was stored in the fridge. This synthesis was gently conducted by .

B Particle Functionalization

For functionalization, MeO-PEG-SH (840 Da, *Iris Biotech GmbH*) was used. The following protocol was kindly developed by .

In the beginning the concentration of spheres in solution was determined via UV-Vis and the average size was determined by TEM (see *appendix C*). The calculation of the number of PEG chains to cover the nanoparticles was conducted as follows: first the surface area of the NPs was calculated. The number of chains per NP was considered to be two times the surface area. To guarantee full coverage, a factor of 2 was taken into account. The accordant amount of PEG was added. The incubation took place at room temperature overnight under continuous stirring.

Three different samples were functionalized. The first sample contained 17 nm-spheres (see *appendix C*) and were synthesized by (see *appendix A2*). The other samples consisted of 9 nm- and 44 nm-spheres respectively and were purchased from *BBInternational*. To reduce the size distribution, the samples were centrifuged as follows: The sample containing the 44 nm spheres was centrifuged for 10 min at 1000 rpm and the supernatant was centrifuged for further 10 min at 1500 rpm. The 17 nm spheres sample was centrifuged for 5 min at 5000 rpm, then for 5 min at 7000 rpm and a third time for another 5 min at 11000 rpm. Between each step, the supernatant was removed. The sample with the 9 nm spheres was applied without further centrifugation.

C Nanoparticle Characterization

C1 Rods

Table 6. Dimensions of the applied nanorods. Overview of the resonance wavelengths λ_{res}, the lengths, widths and the surface areas of the applied rods.

rods	λ_{res} in nm	length in nm	width in nm	surface in nm^2
medium	646	77.81±8.06	35.39±6.09	10660.55±2869.10
big	663	106.92±12.67	49.99±6.57	20867.65±4115.37

Table 7 gives an overview of the gold nanorods which were applied as sensors within this thesis. The dimensions were determined via TEM (*Philips EM-420*). The data were generously provided by .

C2 Spheres

This table provides the average dimensions and the concentrations of the gold nanospheres used as diffusers in *Chapter 6*. The dimensions were determined via TEM (*Philips EM-420*). The data were kindly measured by .

Table 7. Dimensions of the applied spheres. Overview of the resonance wavelengths λ_{res}, the diameters, aspect ratios *AR* and concentrations of the utilized spheres.

spheres	λ_{res} in nm	diameter in nm	AR in nm	concentration in particles/ml
small	530	8.76±0.74	1.13±0.09	$4.23 \cdot 10^{12}$
medium	529	16.62±2.70	1.10±0.06	$2.54 \cdot 10^{11}$
big	534	43.59±1.99	1.05±0.04	$4.31 \cdot 10^{10}$

D Viscosity of Glycerin-Water Mixtures

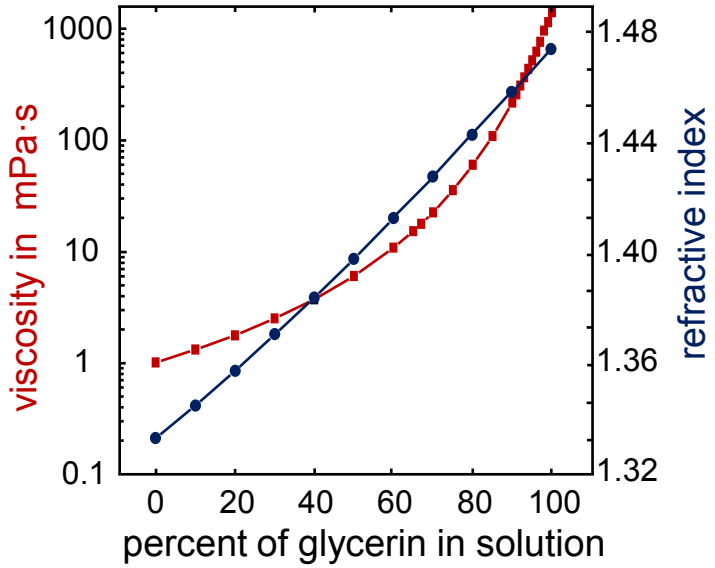

Figure 44. Dependency of viscosity and refractive index of glycerin-water-mixtures. Viscosity (red) and refractive index (blue) increase with the glycerin fraction in solution. Data is valid for room temperature (20 °C). Figure is taken from the dissertation of Dr. Irene Ament.[57]

Figure 44 shows the exponential increase of the viscosity with increasing percent of glycerin in solution. Data is taken from the Dow Chemical Company Website.[176]

E Additional Data for *Chapter* 4

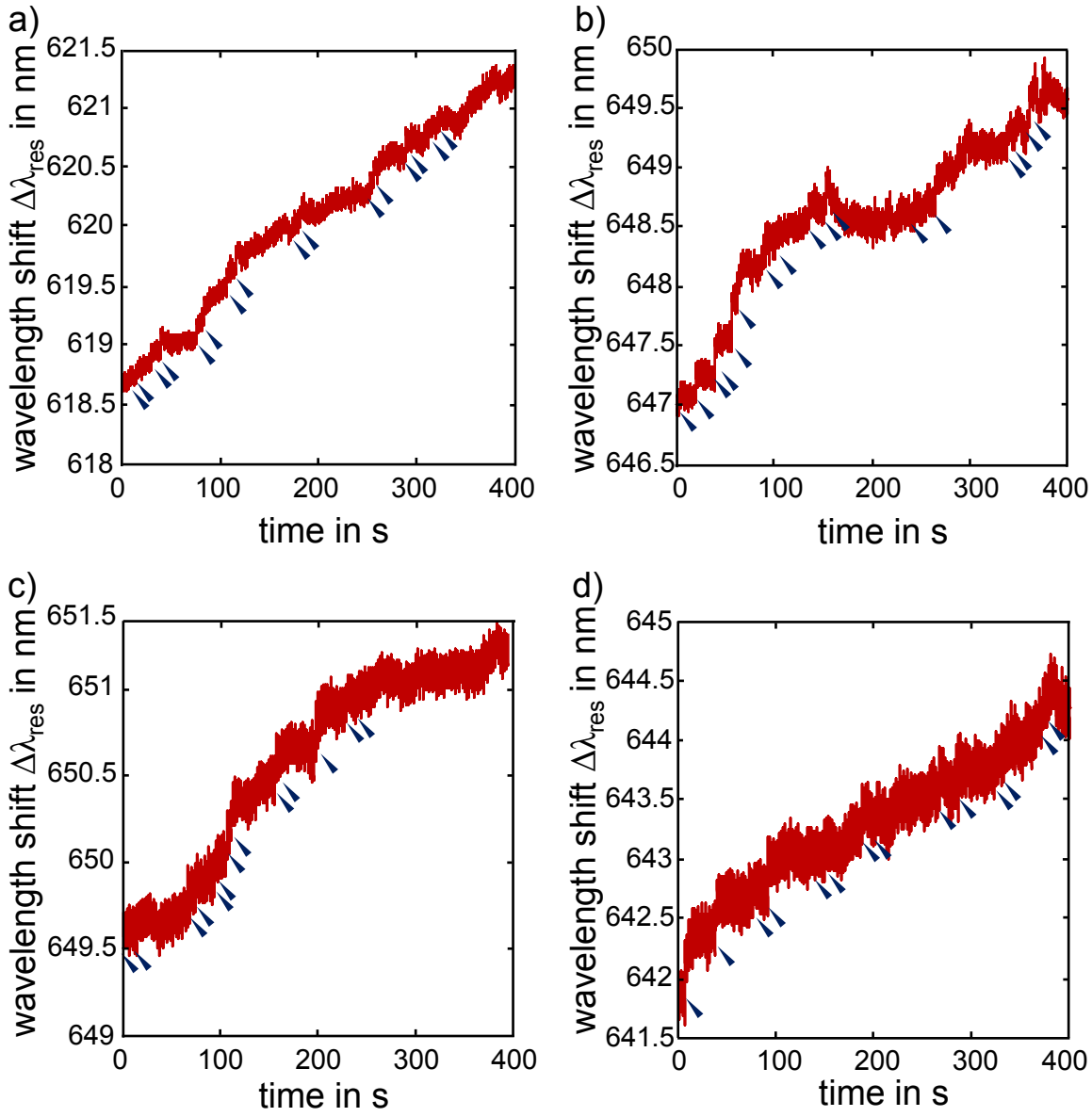

Figure 45. Additional adsorption isotherms of fibrinogen. The sketches correspond to adsorption steps.

In *Figure 45*, additional adsorption isotherms of fibrinogen are shown.

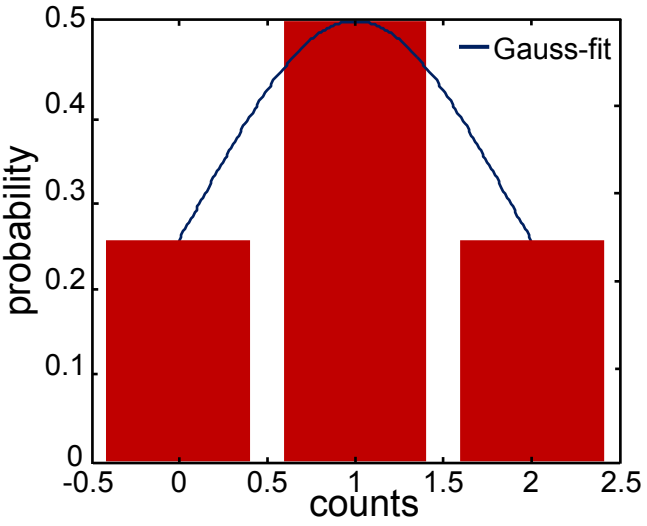

Figure 46. Data evaluation of the time between steps. The probability in the number of units within one section that is defined by the mean time between 2 neighboring units follows a Gaussian distribution. The corresponding timetrace is presented in *Chapter 4.4*, *Figure 14*.

Figure 46 shows that the probability in the number of units within one section that is defined by the mean time between two neighboring units follows a Gaussian distribution. A unit is defined by the number of steps within one section with the size of a mean time between 2 steps.

F Additional Data for *Chapter 5*

The critical micelle concentration (CMC) in phosphate buffered saline medium was determined with a Ring Tensiometer (*dataphysics*, type *DCAT 11EC*). According to J. H. Clint[177] the CMC is represented by the minimum of the surface tension and was thus determined to 0.84 mM. The measurement was kindly conducted in the workgroup of

.

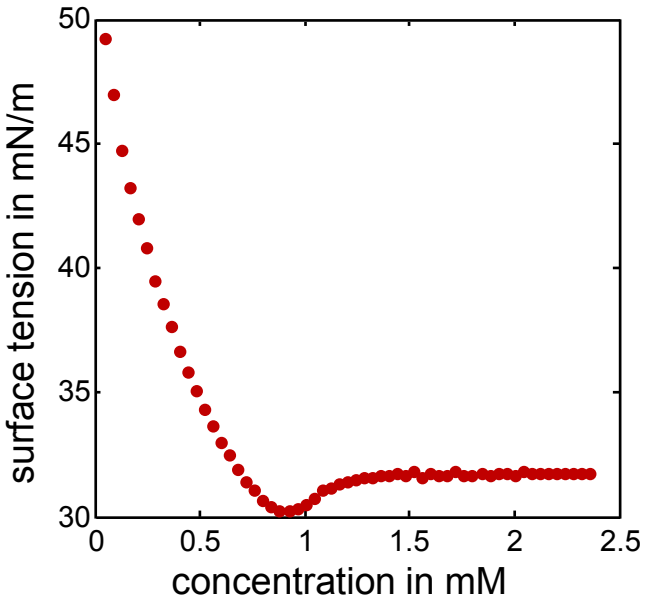

Figure 47. Determination of the critical micelle concentration of sodium dodecyl sulfate in phosphate buffered saline. The surface tension of PBS buffer is displayed as a function of the concentration of SDS.

Sodium thiosulfate can be introduced to remove the CTAB layer and silver bromide on the surface of the gold nanorods. *Figure 48* shows the change in the resonance wavelength when a 50 µM solution of sodium thiosulfate is rinsed into the flow cell. A blue shift of approximately 1.6 nm can be observed. The timetrace belongs to the measurement presented in *Chapter 5.4.1.1*, *Figure 21*.

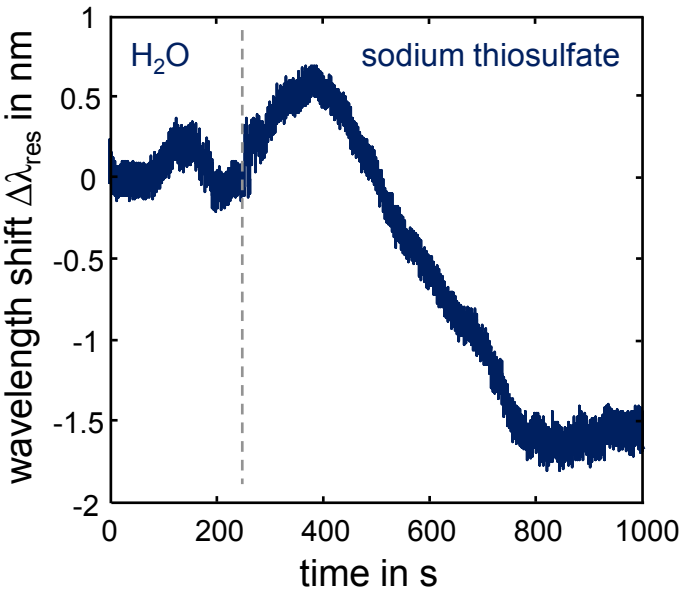

Figure 48. Incubation of sodium thiosulfate. Timetrace of the resonance wavelength of a gold nanorod. When 50 µM solution of sodium thiosulfate is introduced a blue shift of 1.6 nm can be observed. The timetrace belongs to the measurement demonstrated in *Chapter 5.4.1.1*, *Figure 21*.

Figure 49 shows additional timetraces which show that SDS introduces a blue shift in the presence of salts. The experiment could not be conducted with SDS dissolved in a medium containing only KCl due to precipitation of SDS.

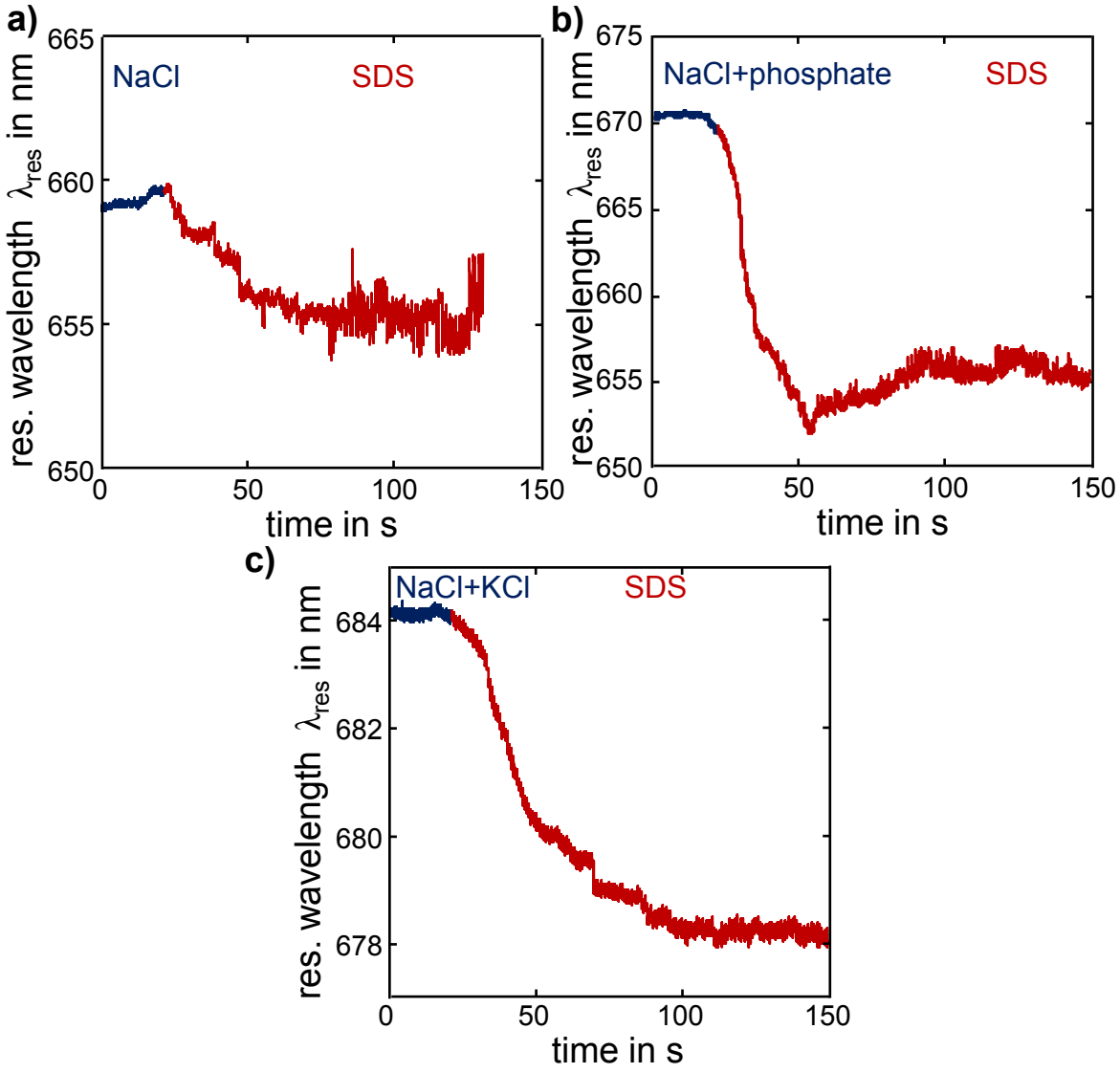

Figure 49. Influence of salt on the adsorption behavior of SDS. Timetraces of the resonance wavelength of single gold nanorods in different aqueous mediums. Blue shifts were observed when introducing sodium dodecyl sulfate with a concentration of 1.7 mM. **a)** The medium was sodium chloride. **b)** A mixture of sodium chloride and sodium phosphate was applied. **c)** A mixture of potassium chloride and sodium chloride acted as medium. In all cases the same concentrations which are present in phosphate buffered saline were utilized.

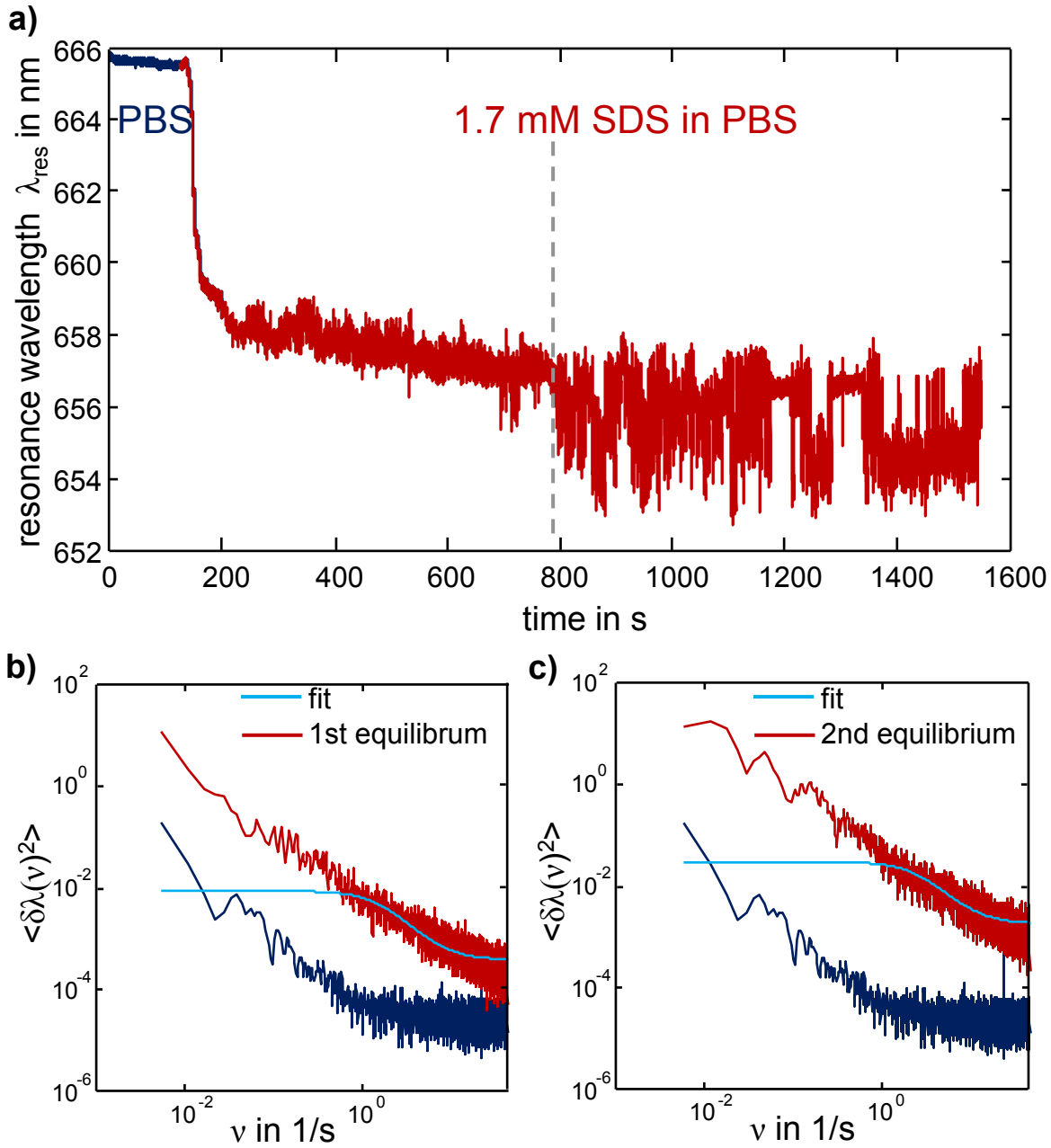

Figure 50. Time dependency of SDS adsorption. This measurement corresponds to the values presented in *Figure 32c*. **a)** Timetrace of the resonance wavelength of a single gold nanorod functionalized with 1-dodecanethiol. It was first rinsed with PBS buffer (dark blue) and then with a buffer solution containing 1.7 mM SDS (red). Shifts in the resonance wavelength were monitored for approximately 1600 s. A blue shift in the resonance wavelength indicates the adsorption of SDS molecules on the surface. Equilibrium was reached within seconds. After approximately 650 s a further increase in the fluctuation amplitude can be observed. **b)-c)** The corresponding power spectra of the timetrace sequences (red) can be described by a single Lorentzian (light blue). For comparison, the power spectra of the baseline in PBS buffer are shown (dark blue).

G Additional Data for *Chapter 6*

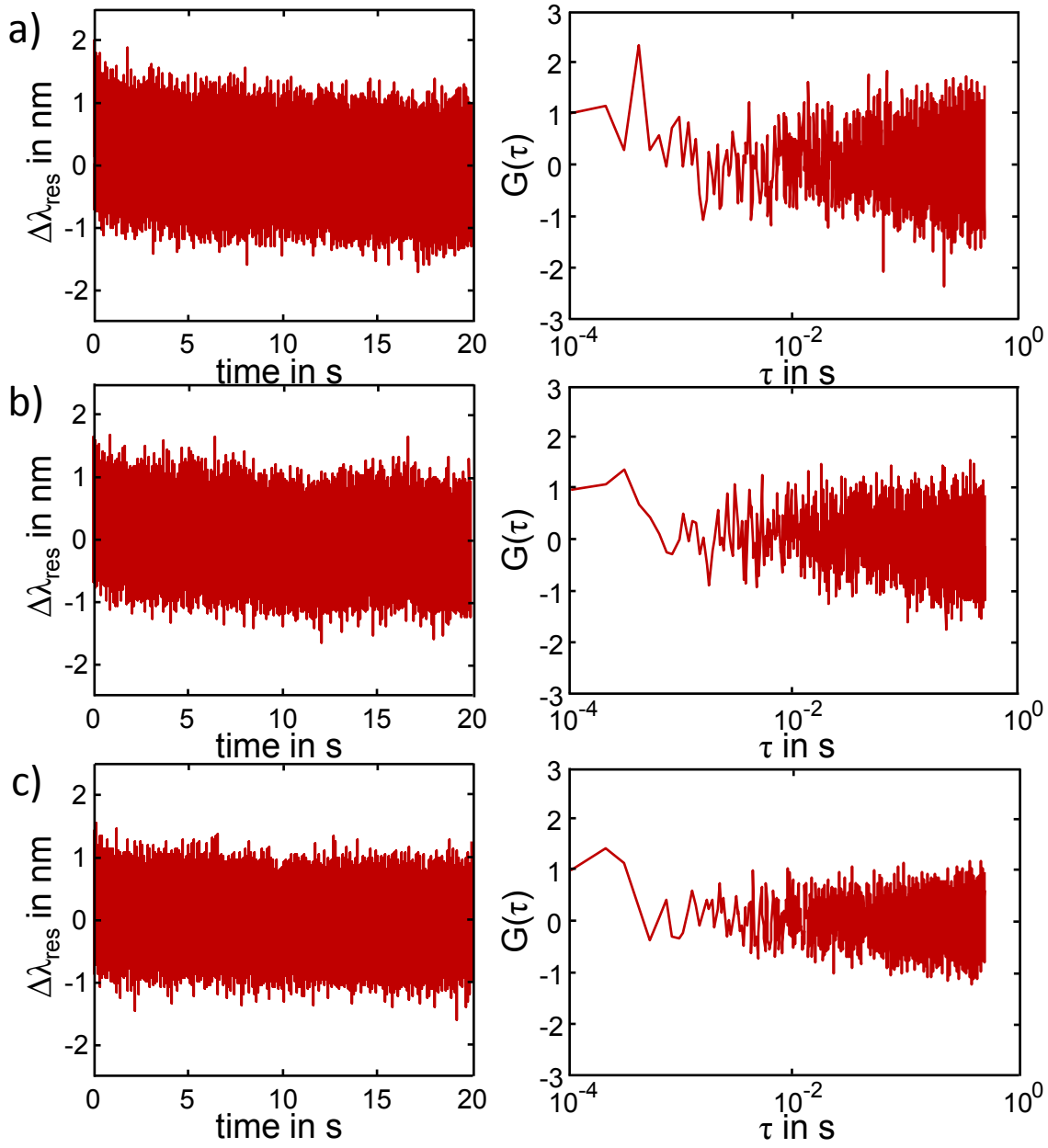

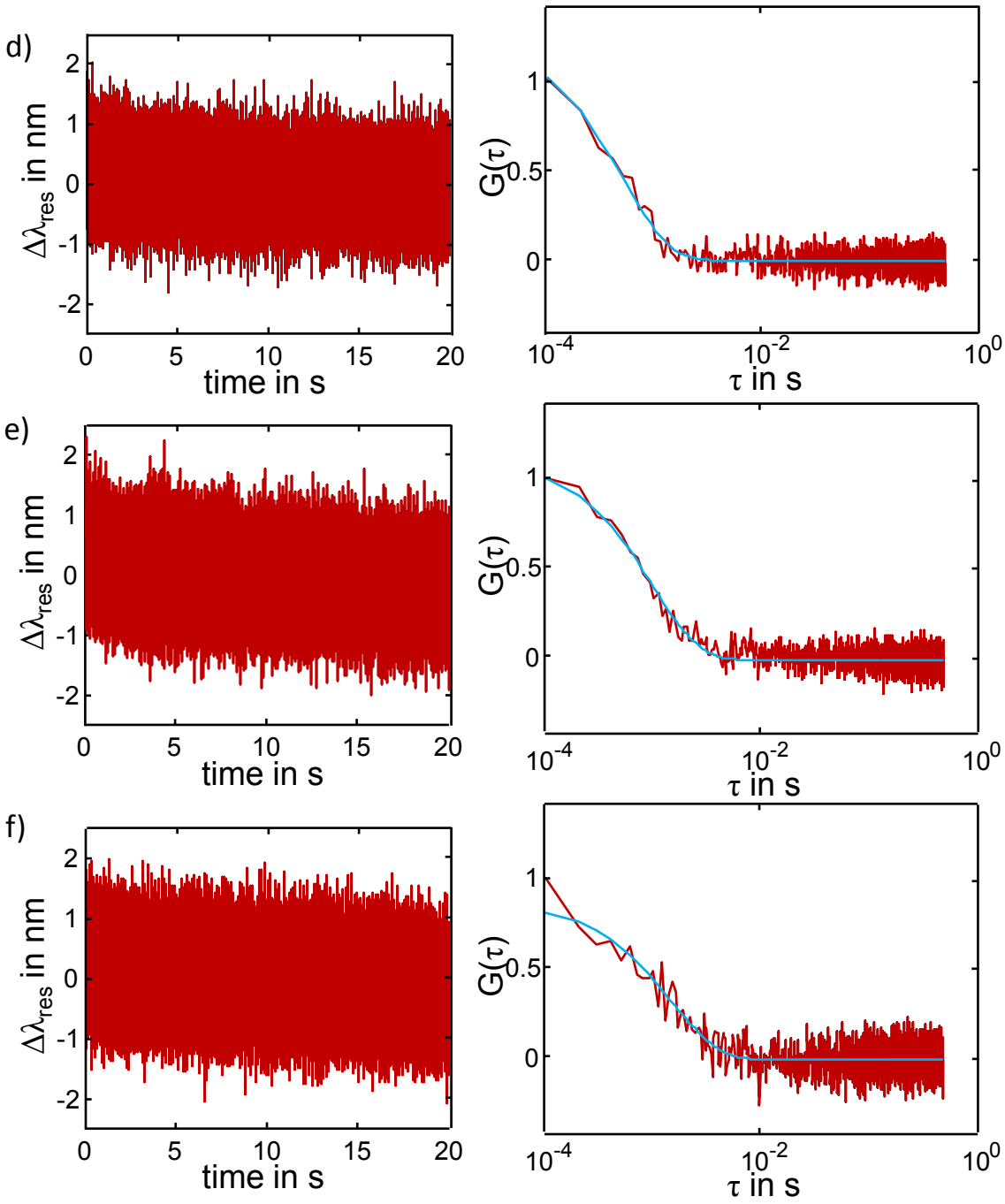
d)
e)
f)
Δλres in nm
time in s
G(τ)
τ in s

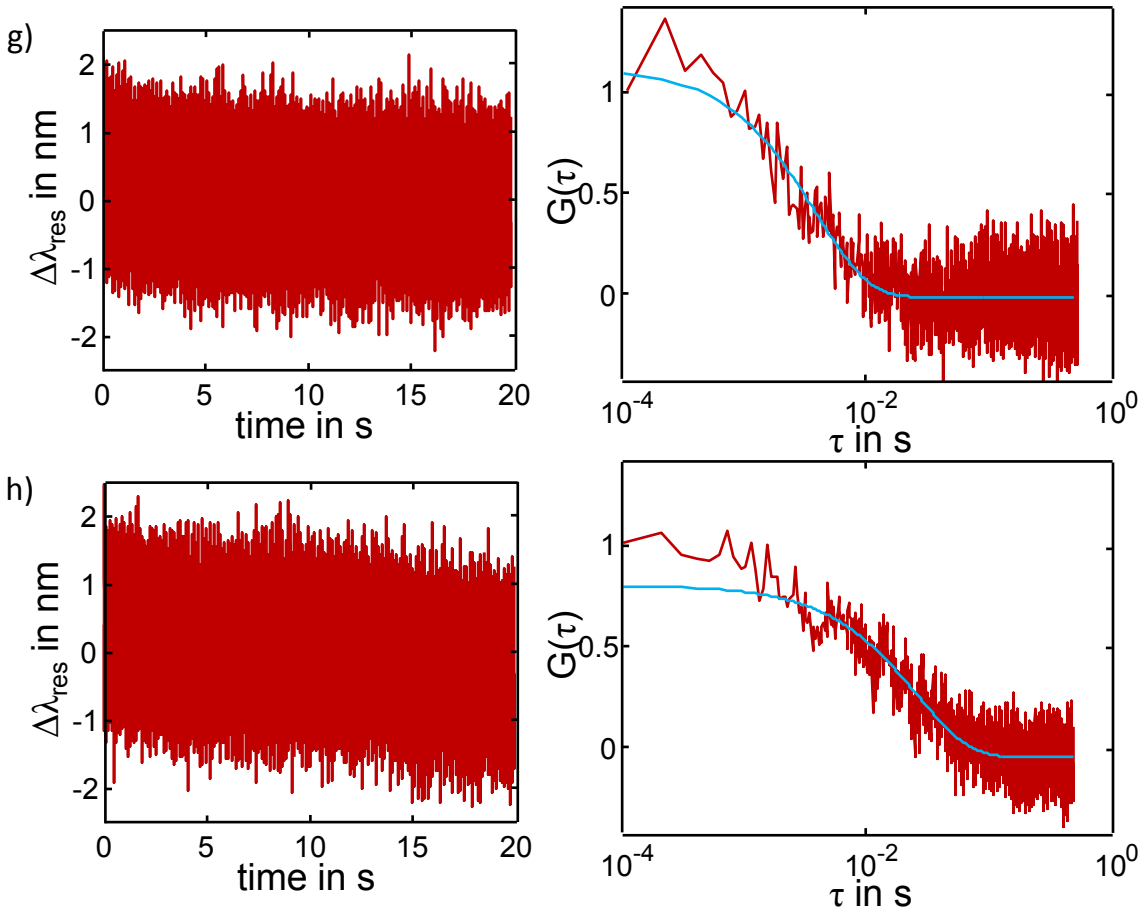

Figure 51. Additional data for the Plasmon Correlation Sensing Project. In each case the timetrace (left) and the corresponding autocorrelation (right) including the exponential fit are shown (blue). A medium sized sensor and 17 nm gold spheres were applied. The timetraces differ in the glycerin ratio. a) 0% glycerin. b) 10% glycerin. c) 20% glycerin. d) 30% glycerin. e) 40% glycerin. f) 50% glycerin. g) 60% glycerin. h) 80% glycerin.

10 Acknowledgements

[personal data removed]

11 List of Publications

Journal Articles

[1] V. Kleiner, L. Slaughter, I. Ament, C. Sönnichsen, *Plasmonic Sensors as New Approach for Diffusion Measurements*, in prep.

Posters and Conferences

[1] *Strategies in Tissue Engineering*, Würzburg, Mai **2012**.

[2] *Diffusion Fundamentals V*, Leipzig, August **2013**.

[3] *Stiftungskolloquium Carl Zeiss Stiftung*, Oberkochen, November **2013**.

12 Curriculum Vitae

[personal data removed]